

AD A 052428

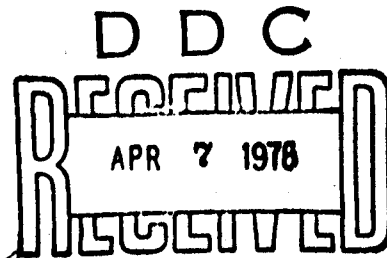
STUDIES ON TRANSONIC TURBINE
WITH FILM-COOLED BLADES

A FOURTH ANNUAL REPORT
July 1, 1976 - June 30, 1977

N. Adams, F. Hajjar, R. F. Topping, J. F. Louis
Massachusetts Institute of Technology
Cambridge, Massachusetts 02139

Technical Report
September 1977

Submitted : Power Programs
Materials Science Division
Office of Naval Research
Department of the Navy
Arlington, Virginia 22217



Best Available Copy

DISTRIBUTION STATEMENT A
Approved for public release;
Distribution Unlimited

⑥ STUDIES ON TRANSONIC TURBINE
WITH FILM-COOLED BLADES.

⑨ A FOURTH ANNUAL REPORT no. 4, 1 Jul 76 -
July 1, 1976 - June 30, 1977

30 Jun 77

⑩ N. Adams, F. Hajjar, R. F. Topping, J. F. Louis
Massachusetts Institute of Technology
Cambridge, Massachusetts 02139

⑯ NPPA14-76-C-0253

⑭ 77-1

Technical Report

Sept 1977

⑫ 116 p.

D D C

APR 7 1978

B

Submitted : Power Programs
Materials Science Division
Office of Naval Research
Department of the Navy
Arlington, Virginia 22217

DISTRIBUTION STATEMENT A

Approved for public release;
Distribution Unlimited

145 850

mtk

REPORT DOCUMENTATION PAGE		READ INSTRUCTIONS BEFORE COMPLETING FORM
1. REPORT NUMBER 77-1	2. GOVT ACCESSION NO.	3. RECIPIENT'S CATALOG NUMBER
4. TITLE (and Subtitle) Studies on Transonic Turbines with Film-Cooled Blades - A Fourth Annual Report		5. TYPE OF REPORT & PERIOD COVERED Technical Report - Annual Report 7/1/76-6/30/77
		6. PERFORMING ORG. REPORT NUMBER
7. AUTHOR(s) N. Adams, F. Hajjar, R. Topping, J.F. Louis		8. CONTRACT OR GRANT NUMBER(s) N00014-76-C-0253
9. PERFORMING ORGANIZATION NAME AND ADDRESS Massachusetts Institute of Technology Gas Turbine Laboratory Cambridge, MA 02139		10. PROGRAM ELEMENT, PROJECT, TASK AREA & WORK UNIT NUMBERS
11. CONTROLLING OFFICE NAME AND ADDRESS Director, Power Programs, Materials Sciences Division, Office of Naval Research, Dept. of the Navy, Arlington, VA 22217		12. REPORT DATE September 1977
14. MONITORING AGENCY NAME & ADDRESS (if different from Controlling Office)		13. NUMBER OF PAGES 108
		15. SECURITY CLASS. (of this report) Unclassified
		15a. DECLASSIFICATION/DOWNGRADING SCHEDULE
16. DISTRIBUTION STATEMENT (of this Report) Approved for Public Release, Distribution Unlimited		
17. DISTRIBUTION STATEMENT (of the abstract entered in Block 20, if different from Report)		
18. SUPPLEMENTARY NOTES		
19. KEY WORDS (Continue on reverse side if necessary and identify by block number) Transonic Turbines Cascade Testing Heat Transfer Unsteady Effects Film Cooling Aerodynamics		
20. ABSTRACT (Continue on reverse side if necessary and identify by block number) During the fourth year of the contract, further advances were made towards the goal of gathering the heat transfer and aerodynamics flow data necessary for a good understanding of the performance of film-cooled, highly-loaded, transonic turbine blading. Surface Mach number and heat transfer rate distributions were determined for a reference transonic airfoil over a range of exit Mach numbers, for inlet incidence angle variation of <u>+15°</u> . An evaluation and comparison		

20. Abstract continued

of all cascade data collected so far was then conducted. Progress was also made in the investigation of the effects of unsteadiness on transonic airfoil aerodynamics and heat transfer.

FOREWORD

This report was prepared by the M.I.T. Gas Turbine Laboratory under Contract No. N00014-76-C-0253 and covers the fourth year of activities under this contract.

The principal investigator is Professor Jean F. Louis. The contract monitor is Mr. James R. Patton, Jr., Power Program, Office of Naval Research, Department of the Navy.

Reproduction in whole or in part is permitted for any purpose of the United States Government.

ACCESSION for	
NTIS	White Section <input checked="" type="checkbox"/>
DDC	Buff Section <input type="checkbox"/>
UNANNOUNCED	<input type="checkbox"/>
JUSTIFICATION _____	
BY _____	
DISSEMINATION/SIMILARITY CODES	
SERIAL AVAIL. and/or SPECIAL	
A	

TABLE OF CONTENTS

	Page No.
ABSTRACT	
INTRODUCTION	
I. AERODYNAMIC AND HEAT TRANSFER AT OFF-DESIGN INCIDENCE	
1.1 The Effect of Incidence on the Pressure Distribution Around the Reference Blade	4
1.1.1 Zero Incidence	5
1.1.2 Positive Incidences	7
1.1.3 Negative Incidences	8
1.2 The Effect of Incidence on Heat Transfer	9
1.2.1 Heat Transfer Distributions Around the Blade	10
1.2.2 Mean Heat Transfer	14
1.3 Summary and Conclusions on the Angle of Incidence Studies	14
1.3.1 Conclusions of Angle of Incidence Studies	15
II. COMPARISON OF TEST DATA FOR THE REFERENCE CONVERGENT BLADE WITH STRAIGHT BACK AND THICK TRAILING EDGE	
2.1 Summary of Demuren's Work at VKI	16
2.1.1 The VKI Facility	16
2.1.2 Measuring Procedure	17
2.1.3 Blade Geometry and Instrumentation	18
2.1.4 The Measured Flow Field	18
2.1.5 The Blade Performance	19
2.1.6 Effect of Blade Solidity on Performance	20
2.1.7 Effect of Reynold's Number Variation	20
2.1.8 Down Stream Wake	20
2.2 Summary of M.I.T. Work	21
2.2.1 Demuren's M.I.T. Work	21
2.2.1.1 Blade Surface Mach Number Distribution	22
2.2.1.2 Comparison Between MIT and VKI Data	22
2.2.1.3 Demuren's Blade Heat Transfer Distribution	23
2.2.2 Hajjar's M.I.T. Work	24
2.3 Comparison of Data	24

III. EFFECTS OF UNSTEADINESS ON TRANSONIC AIRFOILS

3.1 The Flow Field Generated by a Rotating Ellipse	27
 3.1.1 Assumptions	27
 3.1.2 The Complex Potential	28
 3.1.3 Elliptical Coordinates	28
 3.1.4 Flow Field Velocity Components	29
 3.1.5 Flow Field Pressure Analysis	30
 3.1.6 Numerical Calculations and Experimental Comparison	30

ABSTRACT

During the fourth year of the contract, further advances were made towards the goal of gathering the heat transfer and aerodynamics flow data necessary for a good understanding of the performance of film-cooled, highly-loaded, transonic turbine blading.

Surface Mach number and heat transfer rate distributions were determined for a reference transonic airfoil over a range of exit Mach numbers, for inlet incidence angle variation of $\pm 15^\circ$. An evaluation and comparison of all cascade data collected so far was then conducted. Progress was also made in the investigation of the effects of unsteadiness on transonic airfoil aerodynamics and heat transfer.

STUDIES ON TRANSONIC TURBINES WITH

FILM-COOLED BLADES

A FOURTH ANNUAL REPORT

N. Adams, F. Hajjar, R. F. Topping, J. F. Louis

Introduction

The increasing interest in transonic turbines shown over the last few years is a reflection of the need to increase turbine work output per unit area of cooled-blade surface. Much of the increase in turbine cycle efficiency obtained over the last two decades has been due to increased turbine inlet temperature through the use of more efficient cooling techniques. As more and more coolant mass flow is extracted from the compressor, however, a point is reached where the losses and reduction in working fluid caused by the use of increased coolant mass flow more than offset the increase in efficiency and specific thrust attainable by higher turbine inlet temperatures. At this point, the need arises to increase and optimize the work output per unit of cooled-blade surface. This can be accomplished by the use of transonic blading.

The goal of these studies is to gather necessary heat transfer and aerodynamic data for the designer of high performance, film-cooled, highly-loaded transonic turbine blading. In the first three years of the contract, the following key tasks were performed:

- (a) The gathering of film cooling effectiveness data in the transonic range $1.15 < M < 1.4$ for both slot and hole injection using a shock tunnel.
- (b) The gathering of heat transfer and aerodynamics data at the trailing edge of a transonic blade, and the use of this data to formulate a model for the heat transfer and aerodynamic flow at the trailing edge of transonic blades.
- (c) The design, manufacture and check-out of the MIT cascade blowdown facility.
- (d) The design and aerodynamic testing of four transonic blade profiles in a conventional wind tunnel at VKI.
- (e) Aerodynamic and heat transfer testing of the four transonic blade profiles at zero angle of incidence in the blowdown facility.
- (f) The design and manufacture of equipment and instrumentation to measure the effects of periodic unsteadiness on the aerodynamic and heat transfer performance of turbine blades.
- (g) An estimation of the coolant flow requirements of a transonic turbine and a comparison between the coolant flow requirements of the transonic turbine with that of a subsonic turbine of equal work output.

In the fourth year, the following tasks were accomplished:

- (1) Aerodynamic and heat transfer tests were performed on the reference blade profile at off-design angles of incidence in the blowdown facility.
- (2) Heat transfer and aerodynamic properties of the reference blade were compared with earlier experimental work.
- (3) The experimental and analytical program on the effects of unsteadiness on transonic airfoils began.

I. Aerodynamic and Heat Transfer Testing at Off-Design Incidence

1.1 The Effect of Incidence on the Pressure Distribution Around The Reference Blade

Figure 1 shows the reference blade used in conducting the incidence tests and shows the pertinent parameters of the blade. Table 1 shows the location of the pressure taps on the blade, the distance x being measured along the surface of the blade. The isentropic surface Mach numbers were plotted as a function of the non-dimensional length ratio, S/L , for the design incidence of 0° and off-design incidences of ± 7.5 and $\pm 15^\circ$. The range of the isentropic exit Mach number varied from the subsonic region through the low supersonic region. The reference blade was the same as that used in previous work with the exception that surface roughness was removed by smoothing the 4X fabrication master blade.

1.1.1 Zero Incidence

Figures 2a through 2e are plots of the Mach number distribution around the blade surface for increasing mass flows. The stagnation point was found using a potential flow analysis. A line perpendicular to the flow angle was used to find the tangent point on the leading edge of the profile. The stagnation point for zero incidence is located a small distance along the suction side from the tap defined as the leading edge gauge ($S_s/L_s = 0.007$). This is why the Mach number at $S/L = 0$ does not indicate a stagnation condition.

On the pressure side the velocity distribution for all exit Mach numbers is similar. There is a rapid expansion in the leading edge region. The large amount of turning in this location leads to an over-expansion of the flow around $S_p/L_p \approx 0.1$. After a deceleration in this region there is a favorable pressure gradient to the trailing edge of the blade. It should be noted that the Mach number never exceeds unity on the pressure side of the blade. This is expected because the blade design is such that the throat occurs at the trailing edge of the blade, on the pressure side of the profile.

For the suction side, the Mach number distributions are divided into two families of trends, one for subsonic exit Mach numbers and one for the low supersonic exit Mach numbers. The blade was designed such that all the flow turning would be accomplished upstream of the throat. Demuren[1] picked this scheme in designing the four profiles used. The designs were such that the effects of the acceleration due to flow turning would be separated from the acceleration due to different flow areas. In the region before the throat, all the flow turning takes place and after the throat

different area configurations were investigated. It is the flow in the region after the throat that determined the two families of trends for the reference blade.

For the subsonic exit Mach numbers the flow rapidly accelerates from the stagnation point to a peak around $S_s/L_s = 0.45$. This over-expansion is a direct result of the large amount of turning taking place in this region. Following this peak the flow decelerates. If the local velocity is supersonic, this velocity reduction occurs through a series of Lambda shocks located near the blade surface. For exit Mach numbers less than 0.7 the velocities are subsonic and no Lambda shock can exist. After this region the flow undergoes a gradual acceleration to the trailing edge for the case of subsonic exit Mach numbers.

In the transonic regime, the flow accelerates from the stagnation point to a peak at $S_s/L_s = 0.45$. Similar to the high subsonic regime, the isentropic flow velocity is reduced by a series of Lambda shocks located on the blade surface near $S_s/L_s = 0.5$. At $S_s/L_s = 0.55$ the flow decelerates to unity, to meet the boundary condition of choking at the throat. The flow then reaccelerates rapidly and reaches a second peak. At this point the flow passes through a shock wave and the isentropic Mach number decreases. Inspection of the Schlieren photographs shows that this shock is attached to the trailing edge of neighboring blades. The intersection of the shock and the suction side of the blade occurs further downstream as exit Mach number increases. This is the reason the second peak in Mach number for $M_{ex} = 1.53$ is a little further along the suction side than the peak for $M_{ex} = 1.09$.

1.1.2 Positive Incidences

The off-design Mach number distribution for incidences of $+7.5^\circ$ and $+15^\circ$ are reported in Figures 3 and 4, respectively. The overall trend for the positive incidences is similar to that for zero incidence, but some differences do exist. On the pressure side the flow in the region of the leading edge still has a very rapid acceleration, but a smaller deceleration occurs in the region of $S_p/L_p = 0.15$ for the low exit Mach numbers. As the exit Mach number increases an overexpansion does take place in this region. This overexpansion gets more severe as exit Mach number increases, but disappears at the highest exit Mach number ($M_{ex} \approx 1.3$). For both positive incidences, at $M_{ex} \approx 1.3$, the rapid acceleration disappears near the leading edge and the flow undergoes a gentle acceleration from the stagnation point to the trailing edge. One way to explain this is that due to the high curvature, a separation bubble is attached to the blade surface between the first and second pressure taps ($S_s/L_s = 0.07$ and $S_s/L_s = 0.17$). The bubble alters the streamlines in this region. As the Reynolds number increases (mass flow increases) the boundary layer thickness is reduced leading to a smaller radius of curvature in this region. This increase in curvature would cause the leading edge of the bubble to move forward until at the highest mass flow it is over the first pressure tap. The forward movement of the bubble is what causes the sudden change in the shape of the pressure distribution near the leading edge as mass flow increases.

For the suction side no noticeable differences exist between the zero and positive incidence data.

1.1.3 Negative Incidence

For the negative angles of incidence, significant changes occur in the Mach number distribution (Figures 5 and 6). The stagnation point moves up the suction surface as expected. Due to the large amount of turning required to accelerate the flow from the stagnation point, around the leading edge radius to the pressure side, a rapid increase in Mach number is recorded near the leading edge on the pressure side of the blade. Again we see an overexpansion in the region $S_p/L_p \approx 0.1$. At low exit Mach numbers this overexpansion is moderate, followed by a smoothing of the velocity distribution in the mid-range of exit Mach numbers. As the mass flow is increased to the highest mass flow, the overexpansion becomes severe. Without the aid of flow visualization at off-design incidences the following explanation cannot be verified, but heat transfer data tends to confirm that for the lower mass flows, a long separation bubble is attached to the blade surface beginning before the pressure tap at $S_p/L_p = 0.17$ and extending over the next three pressure taps. This is indicated by these three pressure taps reading approximately the same. At the higher mass flows the separation bubble moves forward and gets smaller. This causes a larger overexpansion followed by a more rapid reacceleration after the overexpansion. The bubble collapses due to the acceleration after this point.

On the suction side, there is a drastic change in the transonic regime Mach number distribution downstream of the throat for the negative incidences when compared to the same mass flow at other incidences. For all mass flows the region from the stagnation point up to the throat is similar to the positive and zero incidences, and for the subsonic cases the

Mach number distribution is similar from the throat to the trailing edge. For supersonic exit conditions, however, the flow accelerates further downstream before intersecting with the trailing edge shock. The trailing edge shock intersection with the suction side of the blade can be seen progressing downstream as the exit Mach number increases. For example, the location of the second peak in isentropic Mach number for $\alpha = -15^\circ$ occurs at $S_s/L_s \approx 0.70$ for $M_{ex} = 1.38$, but for $M_{ex} = 1.70$ this peak shifts to $S_s/L_s \approx 0.8$. The same is true for the -7.5° incidence except that at the highest mass flow, the limit loading condition was reached; i.e., the trailing edge shock did not intersect the suction side of the blade. Differences were also caused by the larger inlet area of the negative incidence cascade geometry which changed cascade pressure ratio.

1.2 The Effect of Incidence on Heat Transfer

The calorimetric heat transfer gauges used in this study and described in previous reports were designed to measure heat flux as the hot main flow passes over the blade surface. Heat flux cannot be measured directly but can be calculated as a function of the change in temperature of the gauge. The short run time of the experiment allows a gauge design such that the heat flux is proportional to the temperature rise of the gauge slug. The change in temperature of the slug is measured with a thermocouple. The output of the thermocouple is a constant until initiation of the test, then the output trace starts to rise monotonically until the test is terminated.

The gauge is modeled as a perfectly insulated cylindrical disk with one-dimensional heat transfer into the slug from the hot main flow. The heat transfer property being sought is the convection coefficient, h , averaged over the gauge surface. Since the heat flux into the gauge can be

measured, the convection coefficient is calculated using the difference in temperature of the hot main flow and the gauge as the convective driving force.

1.2.1 Heat Transfer Distributions Around the Blade

The heat transfer characteristics of the reference blade were plotted as the local Nusselt number versus the blade surface location. The heat transfer characteristics were measured for design and off-design engine conditions. The results are generally what is expected; the zero and positive incidence data follow the same trends and magnitudes, while the negative incidence data has slightly different trends in the area of the leading edge and on the suction surface between the throat and the trailing edge (Figures 7 - 11). These two regions are the same regions where the pressure distribution for the negative incidence varied from the zero and positive incidences. The leading edge gauge indicates a lower value of heat transfer than expected in the region of the stagnation point. The stagnation point is not centered on the leading edge gauge but its location is within the gauge area. The boundary layer grows very rapidly in the leading edge region and an averaging effect is expected over this region. A dotted line is shown for the leading edge to indicate that the actual value of the stagnation point is expected to be much higher than the average over the gauge area. The trailing edge gauge measures heat transfer from all sides of the trailing edge radius. The trailing edge heat transfer rate is one of the lowest around the blade surface. The suction side laminar boundary layer transition zone is shown at $S_s/L_s = 0.2$ by a dotted line. The nearest gauges were centered at

$S_s/L_s = 0.13$ and 0.24 . It is felt the transition zone must occur between these two because other likely locations had a higher density of gauges.

For zero incidence, the heat transfer to the pressure side is exactly what is expected. The heat transfer decreases rapidly from the leading edge as the boundary layer grows. In the region $S_p/L_p \approx 0.2$, a slow transition to the turbulent boundary layer takes place. In the region after the transition, the heat transfer slowly decreases or levels off to a minimum at $S_p/L_p \approx 0.5$ and increases from this point to the trailing edge. Two opposing boundary layer properties are interacting along this region. The increased length would indicate that the boundary layer is growing in thickness, while acceleration of the main flow would cause thinning of the boundary layer. An inspection of the velocity distributions indicate increased acceleration after $S_p/L_p \approx 0.5$, which is why the thinning effect becomes dominant in determining the heat transfer and the Nusselt number rises in this region.

The flow on the suction side leads to a wide variation in heat transfer as a function of distance along the suction surface. This variation is also a strong function of exit Mach number. The heat transfer rate decreases from the stagnation point as the laminar boundary layer grows. The laminar transition zone occurs in the vicinity of $S_s/L_s = 0.2$. For the exit Mach numbers of 0.62 and 0.79 there is an increase in the local heat transfer rate followed by a sharp decrease at $S_s/L_s = 0.38$. Inspection of the pressure distributions indicate that this is where the peak in Mach number occurs. In the following region of rapid flow deceleration, a separation bubble forms and causes the reduction in heat transfer to the blade. After this the heat transfer rate tends to level off for the remainder of the blade. For the exit Mach number of 0.93 , this sharp reduction in heat transfer occurs at $S_s/L_s \approx 0.4$ and the pressure peak

occurs at $S_s/L_s \approx 0.45$. There appears to be a "space shift" between the heat transfer gauges and the pressure taps. A possible explanation is that the heat transfer gauges are rough enough to cause the transonic flow to undergo deceleration earlier than a smooth surface. This is suspected because small perturbations of surface roughness are very critical in the transonic flow regime. At $S_s/L_s \approx 0.4$ the heat transfer rate increases until $S_s/L_s \approx 0.6$. This corresponds to the separation bubble reattaching and the boundary layer thinning after reattachment. After this point, the heat transfer levels off, as did the velocity distribution.

For the high mass flows (low supersonic exit velocities) the suction side heat transfer shows a much different trend downstream of the throat. Again minimum heat transfer occurs at $S_s/L_s \approx 0.40$ and the decrease in the heat transfer rate comes before the velocity peak. This systematic "space shift" between the velocity maximum and the heat transfer minimum in the transonic regime seems to indicate that gauge roughness is a likely explanation. After this minimum, the heat transfer increases due to reattachment of the separation bubble. After the throat ($S_s/L_s = 0.55$), the heat transfer continues to increase with acceleration of the main flow, which thins the boundary layer. After the point where the trailing edge shock system intersects the blade surface, the boundary layer separates. The heat transfer decreases and levels off at the trailing edge.

For the positive incidence data no noticeable difference in the trend or the magnitude of the heat transfer data occurs. The effect of the instrumentation "space shift" did occur and indicates the heat transfer gauges do alter the boundary layer in the transonic flow regime.

For the negative incidences a few differences can be found in the heat transfer trends. On the pressure side, the slow transition of the laminar

boundary layer in the region of $S_p/L_p = 0.25$ is not indicated by the heat transfer data for the low exit Mach numbers. Instead heat transfer is fairly level until $S_p/L_p = 0.5$, where rapid acceleration causes thinning of the boundary layer. This would verify the long separation bubble mentioned previously. For higher mass flows the heat transfer decreases from the leading edge gauge and then increases. At the highest mass flows this decrease, followed by an increase in heat transfer, becomes more severe. As discussed previously, as the mass flow increases, the separation bubble becomes smaller in length, which is verified by the decrease and downstream increase in the heat transfer rate. When comparing the negative incidence with the zero and positive incidences the suction side heat transfer is very similar for all cases except the low supersonic exit velocities. For these high mass flow runs the trailing edge shock system intersects the suction surface further down the blade than at design incidence. After the shock hits the blade, the boundary layer separates and the heat transfer levels off. An example of the trailing edge shock interaction with the boundary layer can be seen by comparing the exit Mach numbers of 1.35 and 1.71 for the negative 7.5° incidence. For the low exit Mach number the heat transfer levels off after the shock system intersects the suction surface, but for the high exit Mach number, where limit loading was reached, the heat transfer continues the downward trend indicating thickening of the boundary layer.

1.2.2 Mean Heat Transfer

The Nusselt number averaged over the blade surface was calculated for each test condition. The results are plotted as a function of exit Mach number for different incidences (Figure 12). The results shows for equal mass flow rates the heat transfer for off-design conditions is within 10% of that for design incidence. This indicates that incidence has a very small effect on average values of heat transfer for the conditions tested.

1.3 Summary and Conclusions on the Angle of Incidence Studies

The angle of incidence study examined the effect of incidence angle on the heat transfer performance of transonic turbine blades. This is important to the designer who must be assured there will not be a catastrophic loss in performance at off-design angles of incidence. It is also of importance to the turbine designer since it will help determine the optimum location of cooling ports in order to avoid overheating of the blade at both design and off-design points.

This study has been part of a larger program on transonic turbines which has been going on at the M.I.T. Gas Turbine Laboratory for the past five years. The aim of the overall program is to gather necessary data for cooled transonic turbine blade design and to carry out the testing of film-cooled transonic blades.

1.3.1 Conclusions of Angle of Incidence Studies

1. The off-design incidence angles show local differences in the pressure and heat transfer distributions. The major areas of departure from the design case are on the pressure side near the leading edge and on the suction side near the trailing edge - shock interaction area.
2. The mean Nusselt number was found to be independent of the incidence angle for both subsonic and low supersonic exit velocities. For equal mass flow rates, mean heat transfer rates for off-design incidences were within 10% of the design case.
3. The suction side laminar transition zone was found to be located closer to the leading edge than reported by Demuren[1].
4. The pressure distributions reported here were similar to the measurements taken by Demuren at Von Karman Institute but different from the measurements taken at M.I.T. The heat transfer results were also different, but average values of heat transfer were in good agreement. Improvements in surface instrumentation and of small profile changes are thought to be the cause of the difference between the two sets of data taken at the M.I.T. facility.

II. Comparison of Test Data for the Reference Convergent Blade with Straight Back and Thick Trailing Edge

This section will summarize the experimental test results of the MIT wholly convergent turbine blade with a straight back and thick trailing edge conducted in transonic cascade tests. Three test programs of interest will be summarized: Harold Demuren's work at VKI and MIT[1] and Fred Hajjar's work at MIT[2]. In the MIT studies, both blade surface static pressure and heat transfer distributions were measured, whereas the VKI data is for pressure distribution only.

2.1 Summary of Demuren's Work at VKI[1]

2.1.1 The VKI Facility

The test facility used for the turbine cascade investigation was the Von Karman Institute high speed cascade tunnel. This tunnel is of the blowdown type and is supplied with high pressure air. The turbulence level at the cascade inlet is taken to be 0.7%. The settling chamber pressure was measured with a mercury U-tube manometer. The static pressure on the cascade blades and on the wind tunnel end walls were measured with a mercury multimanometer. Mid-span traverses were performed at the inlet and outlet planes of the cascade utilizing three different probes:

at the inlet, a pitot-directional probe;

at the outlet, a pitot-directional probe combined with a single

needle static probe for $M_e \leq 1.3$;

at the outlet, an AVA-tube probe for $M_e > 1.2$.

2.1.2 Measuring Procedure

Schlieren and shadowgraph photos were taken at various exit Mach numbers to verify the periodicity of the outlet flow angle. The blade performance was determined from inlet and exit traverses and blade pressure distribution measurements. The downstream traverses were made behind several blades including the instrumented blades. The blade pressure distributions were taken without probes in the cascade to avoid probe-induced disturbances.

During the downstream traverses the following values were recorded continuously

ΔP_o = difference between the settling chamber pressure and the total pressure at the probe.

ΔP_s = difference between the static pressure at the probe and atmospheric pressure.

ΔP_{LR} = pressure difference measured by the directional probe.

The inlet Mach number was based on the total pressure and area averaged static wall pressure measurements 0.1 chord upstream of the cascade inlet. The downstream traverse data, taking into account probe calibration, was used to calculate an efficiency and the local Mach number M_2 . A calculated Reynolds number was based on the inlet flow parameters and referenced to 1 cm length.

2.1.3 Blade Geometry and Instrumentation

The following data characterize the blade and cascade geometry for the experiments conducted at the VKI facility (See Figure 1):

Blade chord $c = 2.60$ in.

Blade spacing $g = 1.95$ in.

Stagger angle = 51.0°

Inlet flow angle = 60.0°

Trailing edge thickness = .11 in.

Number of blades = 6

$g/c = 0.75$

The blade pressure distribution was measured by static pressure taps on the pressure side and suction side of two neighboring blades (blades 3 and 4) such that the instrumented blade surfaces formed a blade flow passage.

2.1.4 The Measured Flow Field

The Mach number distribution at the cascade inlet was found from wall static pressure taps in a plane .1 chord ahead of the leading edge. The inlet Mach number variation as a function of exit Mach number is shown in Figure 13. The inlet angle variation in the transverse direction was also measured with no influence of the exit Mach number observed.

The blade velocity distribution is expressed by a local Mach number calculated from the local static pressure on the blade surface and the total pressure upstream of the cascade. The Mach number distribution for a geometry $g/c = 0.75$ is shown in Figure 14.

2.1.5 The Blade Performance

The blade performance was evaluated from a downstream wake traverse at an axial distance of .3 blade chord behind the trailing edge of the blade. The variation in blade losses as a function of exit Mach number is plotted in Figure 15. For exit Mach numbers up to $M_e = 0.7$ the blade losses run up to 8% which is apparently caused by the trailing edge thickness. A sudden rise in the level of losses from $M_e = 0.7$ to $M_e = 0.85$ can be attributed to local lambda shock losses and a shock-boundary layer separation along the upper suction side of the blade. The decrease in losses from 11% at $M_e = 0.85$ to around 5% at $M_e = 1.3$ (the design point) can be attributed to the shocks becoming oblique and flow reattachment occurring. It is suggested that the increase in losses for $M_e > M_{\text{design}}$ is due to the increasing strength of the adjacent blade left running trailing edge shock which intersects the suction side and causes the boundary layer to separate. The losses recorded for $M_e > M_{\text{limit load}}$ depend on the total pressure losses due to the boundary layer, the trailing edge shocks, and the mixing processes between the exit and the traversing planes.

The outlet flow angle β_2 as a function of exit Mach number is also shown in Figure 15. The flow angle decreases slightly from 25.5° to 24° between $M_e = 0.6$ and 1.3. For $M_e > M_{\text{design}}$ ($M_{\text{design}} = 1.3$), the flow exit angle increases slowly up to $M_e = 1.4$, but then increases sharply for $M_e > 1.4$. This sharp increase can be associated with an over-expansion at the blade trailing edge. At $M_e = M_{\text{limit load}}$ ($M_{\text{limit load}} = 1.59$) the outlet flow angle deviation was about 10° .

2.1.6 Effect of Blade Solidity on Performance

Tests were also conducted to determine the effects of stage solidity (chord length/blade spacing) on the blade performance. The blade was tested at g/c = 0.81 and 0.695. Examination of the resultant blade velocity distributions and the Schlieren photos showed a change in the locations and inclinations of the left-running shocks for comparable exit Mach numbers. Also, as the blade spacing increased, the shock strength became weaker and so flow separations resulting in the shock-boundary layer interactions were avoided. No other significant effect on the blade velocity distribution was seen.

2.1.7 Effect of Reynold's Number Variation

The results of a series of tests to examine the effects of Reynold's number variation between 10^5 and 10^6 showed no noticeable change in either the blade pressure distribution nor in the shock structure. Hence it was concluded that Reynold's number effects in the range of 10^5 and 10^6 showed no noticeable change in either the blade pressure distribution nor in the shock structure. Hence it was concluded that Reynold's number effects in the range of 10^5 to 10^6 were negligible.

2.1.8 Down Stream Wake

Analysis of the downstream wake using the downstream traverse .3 chord behind the blades shows an interesting effect of Mach number on the structure of the wake. The downstream wake profile is shown in Figure 16. As the exit Mach number increases, the flow asymmetry increases. A characteristic effect is the increase in the wake depth during transition

from subsonic Mach number to supersonic Mach number. The width of the wake also changes. Careful examination of the Schlieren photographs of the wake flow shows that it consists, under certain conditions, of von Karman vortex sheets.

2.2 Summary of M.I.T. Work

Demuren's and Hajjar's work was conducted at the M.I.T. Gas Turbine Laboratory utilizing the hot blowdown turbine facility. This facility delivers air at selected pressures and temperatures for a maximum duration of ten seconds at maximum flow rate. Tests have shown that steady-state flow conditions are reached 0.2 seconds into the test.

2.2.1 Demuren's M.I.T. Work[1]

Demuren's experiment at M.I.T. tried to duplicate most of the test parameters utilized in the VKI tests. The primary differences between the two were:

1. $g/c = 0.695$ whereas VKI $g/c = 0.75$
2. 9 blade cascade whereas VKI utilized 6 blades
3. short duration whereas VKI ran continuously steady state
4. 10% turbulence level vs. 0.7% at VKI
5. flow temperature of $400^{\circ} F$ vs. room temperature at VKI.

The same blade profile was utilized in both tests. Also, the blade was instrumented in the same manner.

2.2.1.1 Blade Surface Mach Number Distribution

The plot of the measured blade velocity distribution is shown in Figure 17. A very fast expansion is seen to take place on the suction side with the Mach number reaching a peak at a location where some surface bumps are located on the blade. The flow decelerates a bit and then quickly starts to accelerate again until the surface is intercepted by the left-running trailing-edge shock from the adjacent blade, downstream of which the flow decelerates and later accelerates towards the trailing-edge. As the pressure ratio increases across the cascade, the intercepting shock moves down towards the blade trailing edge. The limit loading condition is such that this shock passes downstream of the trailing edge and no longer affects the channel flow. The flow on the pressure side rapidly accelerates immediately downstream of the stagnation point, quickly decelerates, and then gradually accelerates to its maximum value at the trailing edge. Once the flow is choked, there is very little change in the pressure side velocity distribution.

2.2.1.2 Comparison Between MIT and VKI Data

A detailed comparison was made[1] of the Mach number distribution around the blade obtained at the MIT hot blowdown facility with that obtained at the VKI facility. Overall, the pattern of the Mach number distribution was similar. Fast acceleration from the stagnation point on the suction side led to the first Mach number peak. But the location and absolute magnitude of the peak were different. The peak was shifted forward in the MIT data. Several possible reasons were suggested for this shift. The VKI tests were conducted with cold flow and a low turbulence

level (.7%) whereas the MIT work was with hot flow air (400° F) with a turbulence level of 10%. Schlieren photos taken at VKI show a distinct separation region on the suction side of the blade. The combined effects of large blade curvature and surface roughness could have triggered the separation. The high free-stream turbulence in the MIT facility could allow a more rapid flow reattachment and thus change the velocity profile in this area. Also minor changes in static pressure tap locations on the blade surfaces could account for shifts in the peak locations and magnitudes. The overall pattern of the velocity distribution is the same in both sets of data. Good agreement is seen on the pressure side distribution with a gradual Mach number increase up to the trailing-edge.

2.2.1.3. Demuren's Blade Heat Transfer Distributions

The measured blade surface heat transfer distributions are presented in Figure 18. Overall, the blade surface velocity and cascade turbulence level greatly influence the boundary layer properties which, in turn, influence the heat transfer rate to the cascade blade surface. A similar effect on both the velocity and heat transfer distributions can be seen in the area of the shock-boundary layer interaction. The rapid acceleration from the leading edge on the suction side creates a condition very favorable for the formation of a laminar boundary layer and a resultant decrease in Nusselt number. The transition to turbulent boundary layer flow causes a sudden increase in the Nusselt number. Thereafter the Nusselt number fluctuates in a manner similar to the velocity distribution until it intercepts the left-running shock from the adjacent blade. Downstream of the shock, the Nusselt number decreases significantly and then increases as the flow accelerates toward the trailing edge.

On the pressure side of the blade, the rapid acceleration from the stagnation point is again conducive to the formation of a laminar boundary layer with the resultant decrease in Nusselt number. Transition appears to occur at $x/c = 0.3$ with the Nusselt number increasing to the trailing edge due to the continuous acceleration of the flow. This increase in the Nusselt number is attributed to the thinning of the boundary layer as the flow accelerates. A high level of heat transfer was recorded close to the trailing edge (about 75% of the mean heat transfer measured at the leading-edge area). Because of the finite size of the heat transfer gauge (3/32 in. diameter), the heat transfer rate is averaged over this area, whereas the Nusselt number could have locally varied widely in this area. Thus the local heat transfer rates are, in fact, average heat transfer rates over a given small area.

2.2.2 Hajjar's MIT Work[2]

Hajjar's work was intended to first correlate the work of Demuren and then investigate the angle of incidence effects on the cascade blade performance. The same blade profile was utilized except Hajjar removed the surface bumps referred to by Demuren in his thesis. The same principles of instrumentation were used by both Hajjar and Demuren. Hajjar's results are presented in Section I of this report.

2.3 Comparison of Data

The Mach number distribution measured by Hajjar around the reference blade at zero angle of incidence (Figure 19) was compared to the data published by Demuren[1]. Demuren presents two different sets of Mach number distributions, one for data recorded at M.I.T. utilizing a hot flow (Figure 17) and one for data recorded at V.K.I. utilizing a room

temperature flow (Figure 14), for basically the same reference blade.

Hajjar's and Demuren's M.I.T. data shows good agreement on the pressure side of the profile and poor agreement on the suction side. On the suction side, Demuren's first Mach number peak occurs for a smaller x/c and is lower in magnitude. Demuren's second peak for the low supersonic exit Mach number is also shifted. Comparing Demuren's V.K.I. data with Hajjar's M.I.T. tests shows much better agreement. Demuren discussed reasons such as the suction side surface profile "bump", turbulence level (M.I.T. 10% vs. V.K.I. 0.7%) and the difference in the mainstream flow temperature to account for the difference in his two sets of data. With instrumentation improvements discussed by Hajjar[2], the V.K.I. data was reproduced at the M.I.T. facility. It is possible that the roughness caused by instrumentation on Demuren's M.I.T. blade led to deceleration of the transonic flow prematurely. This would account for the velocity peaks occurring sooner in Demuren's data.

A sample comparison of heat transfer was made with Demuren's work (Figure 20). The test conditions compared were an exit Mach number of 1.09 for Hajjar's tests to an exit Mach number of 1.08 for Demuren's data. There are differences in the local Nusselt number in all sections of the blade except the fully turbulent region after the throat on the suction side. Since the pressure distributions were much different in this region, one should not expect a good correlation of heat transfer results. For the pressure side much better agreement was expected, but the results were somewhat different. An explanation is that Demuren's gauges were in one axial line, which may cause boundary layer perturbations as discussed by Hajjar.

III. Effects of Unsteadiness on Transonic Airfoils

Flows in gas turbines are, in general, unsteady. The unsteady effects arise from factors such as blade passage, propagation of azimuthal nonuniformities, and the propagation of periodic disturbances which originate upstream of the turbine. These unsteady disturbances are likely to have a marked effect on the blade passage flow field, the base flow, the trailing edge shock system, and the blade heat transfer. The aerodynamic flow around the trailing edge is of great interest because it strongly influences blade losses.

When a transonic cascade is operating at conditions other than limit loading, the left running trailing edge shock of one blade usually interacts with the boundary layer of the suction side of the adjacent blade, and this interaction can result in local or full flow separation, which will have an influence on the turbine flow losses. Since the rotor typically operates at a high angular velocity with many individual blades, a stator can see in the neighborhood of 10^5 fluctuations per minute. The purpose of this investigation is to examine the effects of high frequency periodic unsteadiness on the performance of a given turbine blade by simulating the blade passage disturbance in a 2-D transonic turbine cascade.

The investigation will examine the following phenomena:

1. The aerodynamic and heat transfer properties in the neighborhood of the oscillating shock-boundary layer interaction on the suction side of an adjacent blade;
2. The effect of periodic unsteady disturbances on the potential flow in the blade passage;
3. The effect of oscillating disturbances on the base pressure behind the stationary blade;
4. The accumulated losses in the wake

The investigation will help provide a basic understanding of the loss mechanisms which are inherent in all gas turbine generators which utilize transonic rotating machinery.

The experiment will be performed in the M.I.T. linear cascade tunnel attached to the hot blowdown facility. A high frequency disturbance generated by rotating a small elliptical body downstream of the turbine cascade row will be used to simulate the periodic unsteady effects. Blade surface and cascade wall instrumentation will be utilized in measuring the aerodynamic and heat transfer properties for different operating conditions. A traversing probe will be used downstream to measure the cascade wake flow properties. It is anticipated that a model will be developed as a result of the experimental investigation which will include the effects of the shock-boundary layer interaction, the base pressure fluctuations, and the resultant losses in the wake.

To date, the air turbine used to rotate the elliptical rotor has been extensively tested, the cascade has been modified to accept the unsteady experiment and the pressure field around the rotor has been mapped.

3.1 The Flowfield Generated by a Rotating Ellipse

3.1.1 Assumptions

For this study a two-dimensional, inviscid, incompressible, irrotational fluid was assumed. The rotating elliptical body is an ellipse described by the equation:

$$\frac{x^2}{a^2} + \frac{y^2}{b^2} = 1 \quad (1)$$

where a and b are the semi-major and semi-minor axes respectively.

3.1.2 The Complex Potential[3]

The complex potential which describes the fluid motion generated by a rotating elliptical cylinder about its axis in an infinite fluid is given in terms of elliptical coordinates as

$$W = i C e^{-2J} \quad (2)$$

with the velocity potential given as

$$\phi = C e^{-2\epsilon} \sin 2n \quad (3)$$

and the stream function given as

$$\psi = C e^{-2\epsilon} \cos 2n \quad (4)$$

with C given as

$$C = 1/4 \omega(a + b)^2 \quad (5)$$

where ω is the angular velocity of the rotating ellipse and ϵ and n are elliptical coordinates.

3.1.3 Elliptical Coordinates (ϵ, n, z)

The elliptical coordinates (ϵ, n, z) form an orthogonal curvilinear coordinate system which is related to a cartesian coordinate system (x, y, z) by

$$x = c \cosh \epsilon \cos n \quad (6)$$

$$y = c \sinh \epsilon \sin n \quad (7)$$

$$z = z \quad (8)$$

where $0 \leq \epsilon < 00$ and $0 \leq n < 2\pi$. curves of constant ϵ give

$$\frac{x^2}{c^2 \cosh^2 \epsilon} + \frac{y^2}{c^2 \sinh^2 \epsilon} = 1 \quad (9)$$

which are confocal ellipses with foci at $(\pm c, 0)$. Curves of constant n give

$$\frac{x^2}{c^2 \cos^2 n} - \frac{y^2}{c^2 \sin^2 n} = 1 \quad (10)$$

which are confocal hyperbolas with foci at $(\pm c, 0)$.

3.1.4 Flow Field Velocity Components

The velocity vector \mathbf{V} can be resolved into elliptical coordinate components

$$\mathbf{V} = v_\epsilon u_\epsilon + v_\eta u_\eta \quad (11)$$

where u_ϵ and u_η are unit vectors. The velocity components are given by

$$v_\epsilon = \frac{1}{h_\epsilon} \frac{\partial \phi}{\partial \epsilon} \quad (12)$$

and

$$v_\eta = \frac{1}{h_\eta} \frac{\partial \phi}{\partial \eta} \quad (13)$$

with the scale factors

$$h_\epsilon = h_\eta = c \sqrt{\cosh^2 \epsilon - \cos^2 n} \quad (14)$$

substituting equation (3) and (14) into (12) gives

$$v_\epsilon = \frac{-2 \phi}{\sqrt{c \cosh^2 \epsilon - \cos^2 n}} \quad (15)$$

and equations (3), (4), and (14) into (13) gives

$$v_\eta = \frac{2 \phi}{\sqrt{c \cosh^2 \epsilon - \cos^2 n}} \quad (15)$$

3.1.5 Flowfield Pressure Analysis [5]

Following the analysis by Milne-Thomson, an expression for the pressure and velocity in the slipstream of an advancing propeller can be written as:

$$\frac{P}{\rho} + \frac{1}{2} V^2 - r^2 \omega \Omega = \frac{1}{9} \quad (17)$$

where P is the local pressure, ρ the density, V the absolute air speed, ω the angular velocity of the rotating body, Ω the angular speed of a plane containing the point of interest, r the distance containing the point of interest, and ∞ the pressure at infinity. Using equation 17, the pressure field can be determined using the results of the potential velocity field.

3.1.6 Numerical Calculations and Experimental Comparison

In order to better understand the aerodynamics of the elliptical rotor, a test has been conducted to measure the flowfield generated by the rotating body. Three small (.24 in. diameter diaphragm) miniature quartz Kistler Series 600 pressure transducers were placed with the pressure sensitive diaphragms parallel and flush to a coverplate to record the short term static pressure responses generated. Figure 21 shows the location of the transducers in relation to the rotating body. Transducer location 1 corresponds to the mean radius of the elliptical body. Location 2 corresponds to one mean radius past the maximum radius of the rotor, whereas location 3 is approximately 2 1/4 mean radii past the maximum radius.

Figure 21 details the specifications of the elliptical body where the semi major axis a is 0.632 inches, the semi minor axis b is 0.211 inches,

and the focii are at $c = \pm 0.596$ inches. In the analysis it is assumed that this body is described by equation (1), an ideal ellipse. Utilizing the model just described, flow field calculations were made using the three transducer locations as points of interest. The first location, however, at $r = 0.42$ inches was moved to $r = 0.632$ inches in the computations to avoid singularities in the calculation.

The position of the elliptical body relative to the three points of interest was described by a 24 "quasi-steady" point coordinate system at rest with respect to the rotating body. All is symmetric about 180° . See Figure 22 and Table 2. In order to determine the velocity potential (equation 3) at each point of interest the elliptical coordinates for each point were determined using equations 6, 7, and 9 in an iterative procedure. The computed elliptical coordinates are tabulated in Table 2. Equations 3, 4, and 5 are used to determine the value of potential and stream function for each point of interest. The constant C (equation 5) was determined to be $6.5 \text{ ft}^2/\text{sec}$ for angular rotation of 50K RPM and $10.3 \text{ ft}^2/\text{sec}$ for 80K RPM. Representative values of ϕ and ψ are presented in Table 3 and plotted in Figures 23 and 24. The resultant velocities were calculated using equations 15 and 16 and are presented in Table 4 and Figures 25, 26 and 27.

Equation 17 was used to calculate the flowfield pressure at the various points of interest. Since in this study we are interested only in changes of pressure for a given rotation of the elliptical body, the equation can be simplified to

$$P_i - P_j = 1/2 \rho (V_j^2 - V_i^2)$$

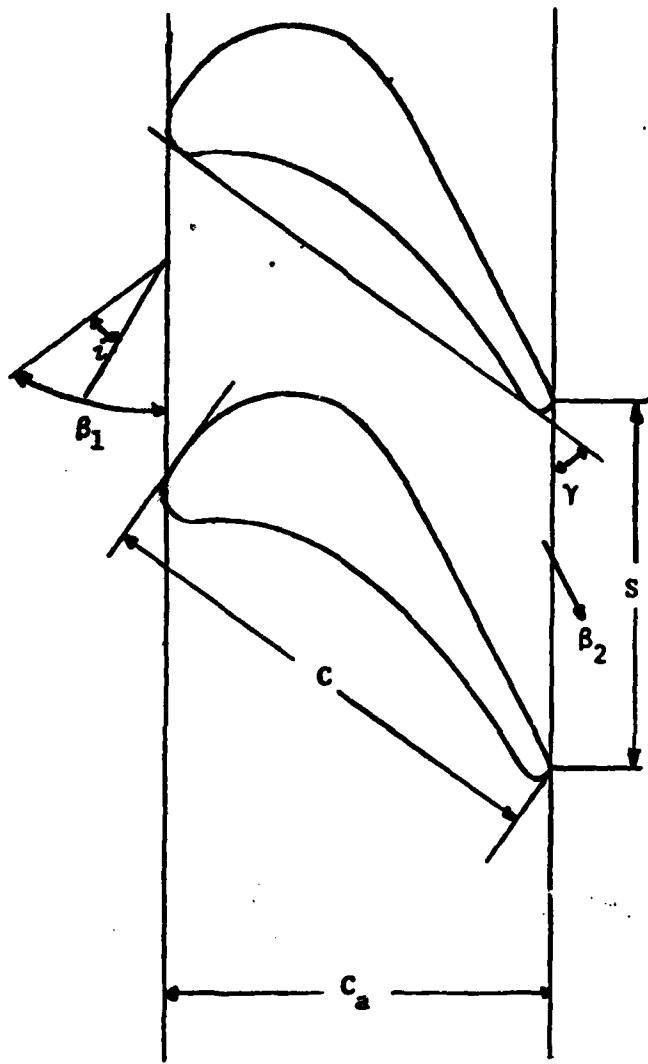
Table 5 presents the results of the pressure calculations in terms of dynamic pressure. As can be seen, the pressure change at location 1 is much greater than at locations 2 and 3 for both cases under consideration. In terms of pressure changes per revolution, at location 1 the total change is 1.10 psi at 50K RPM whereas at 80K RPM the change is 2.81 psi. The following summarizes the calculation:

<u>Location</u>	<u>50K RPM</u>	<u>80K RPM</u>
1	1.10 psi	2.81 psi
2	1.55×10^{-3} psi	3.98×10^{-3} psi
3	$.88 \times 10^{-5}$ psi	2.24×10^{-5} psi

The results of the air turbine tests for transducer location 1 (under the elliptical body) are shown in Figure 28 and in Table 6. In the graph 1 psi is about 27 mv. Hence, for 50K RPM, the average output was .47 psi whereas for 80K RPM, 1.1 psi. The analogous procedures for calculating pressures for 20K, 30K, 40K, 60K, 70K, and 90K RPM have been performed and the results are presented in Figure 29. Here the results of calculations and measurements are presented. The maximum ΔP values for each RPM are recorded, and show a closer correlation to the theoretical results.

References

1. Demuren, Harold O., "Aerodynamic Performance and Heat Transfer Characteristics of High Pressure Ratio Transonic Turbines," Doctor of Science Thesis, Department of Aeronautics and Astronautics, Massachusetts Institute of Technology, 1976..
2. Hajjar, Fred G., "The Heat Transfer Characteristics of Transonic Turbine Blades as a Function of Angle of Incidence" Master of Science Thesis, Department of Mechanical Engineering, Massachusetts Institute of Technology, 1977.
3. Streeter, Victor L., "Fluid Dynamics, First Edition, McGraw-Hill Book Co., Inc., New York, 1948.
4. Hildebrand, Francis B., "Advanced Calculus for Applications", Second Edition, Prentice-Hall Inc., New Jersey, 1976.
5. Milne-Thompson, L.M., "Theoretical Aerodynamics", Fourth Edition, Dover Publications, Inc., New York, 1966.



C - Chord 2.6"
 C_a - Axial Chord 2.0"
 S - Blade Space 2.0"

β_1 - Inlet angle 60°
 γ - Stagger Angle 51°
 β_2 - Exit Angle 25°
 i - Angle of Incidence

Drawing of Reference Blade Used For Tests

FIGURE 1. CASCADE GEOMETRY

DESIGNATION	X-COORD	Y-COORD	S/L
Pressure Side and Leading Edge			
P1	2.415	0.055	0.92
P2	2.300	0.110	0.87
P3	2.180	0.155	0.82
P4	2.015	0.210	0.76
P5	1.815	0.265	0.68
P6	1.630	0.305	0.59
P7	1.315	0.345	0.49
P8	1.030	0.340	0.38
P9	0.770	0.300	0.28
P10	0.500	0.195	0.17
P11	0.285	0.040	0.07
LE	0.115	0.010	0
Suction Side and Trailing Edge			
S17	0.005	0.165	0.06
S16	0.005	0.410	0.13
S15	0.115	0.705	0.22
S14	0.230	0.830	0.26
S13	0.330	0.900	0.30
S12	0.440	0.945	0.33
S11	0.550	0.965	0.36
S10	0.740	0.945	0.41
S9	0.830	0.920	0.44
S8	1.070	0.820	0.51
S7	1.290	0.720	0.58
S6	1.535	0.610	0.65
S5	1.745	0.510	0.72
S4	1.970	0.405	0.79
S3	2.185	0.300	0.85
S2	2.400	0.195	0.92
S1	2.535	0.120	0.96
TE	2.605	0.030	1

Dimensions given in inches, T = ±0.005

TABLE 1. LOCATION OF PRESSURE TAPS

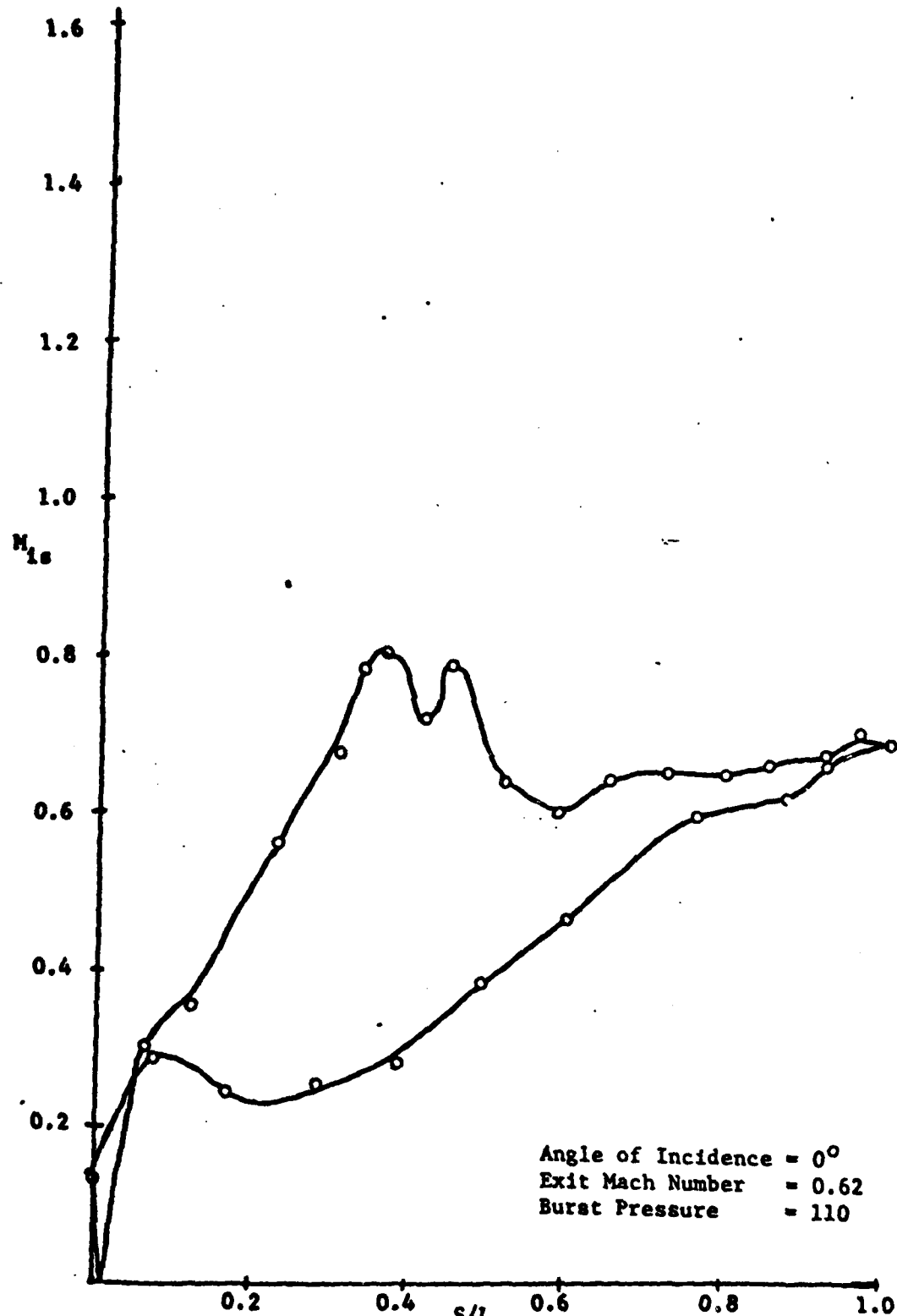


FIGURE 2A LOCAL ISENTROPIC MACH NUMBER VS SURFACE LOCATION.

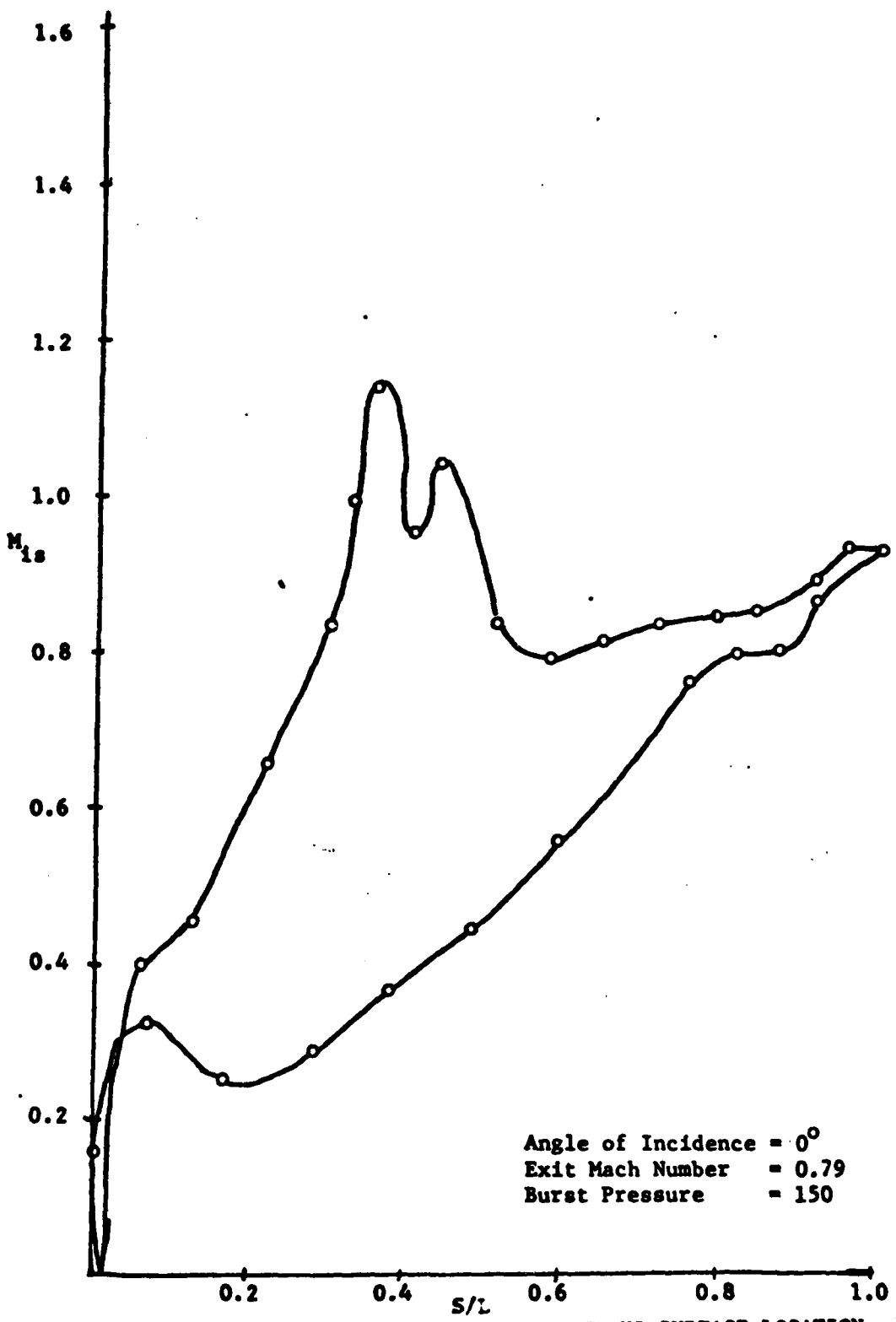


FIGURE 25. LOCAL ISENTROPIC MACH NUMBER VS SURFACE LOCATION

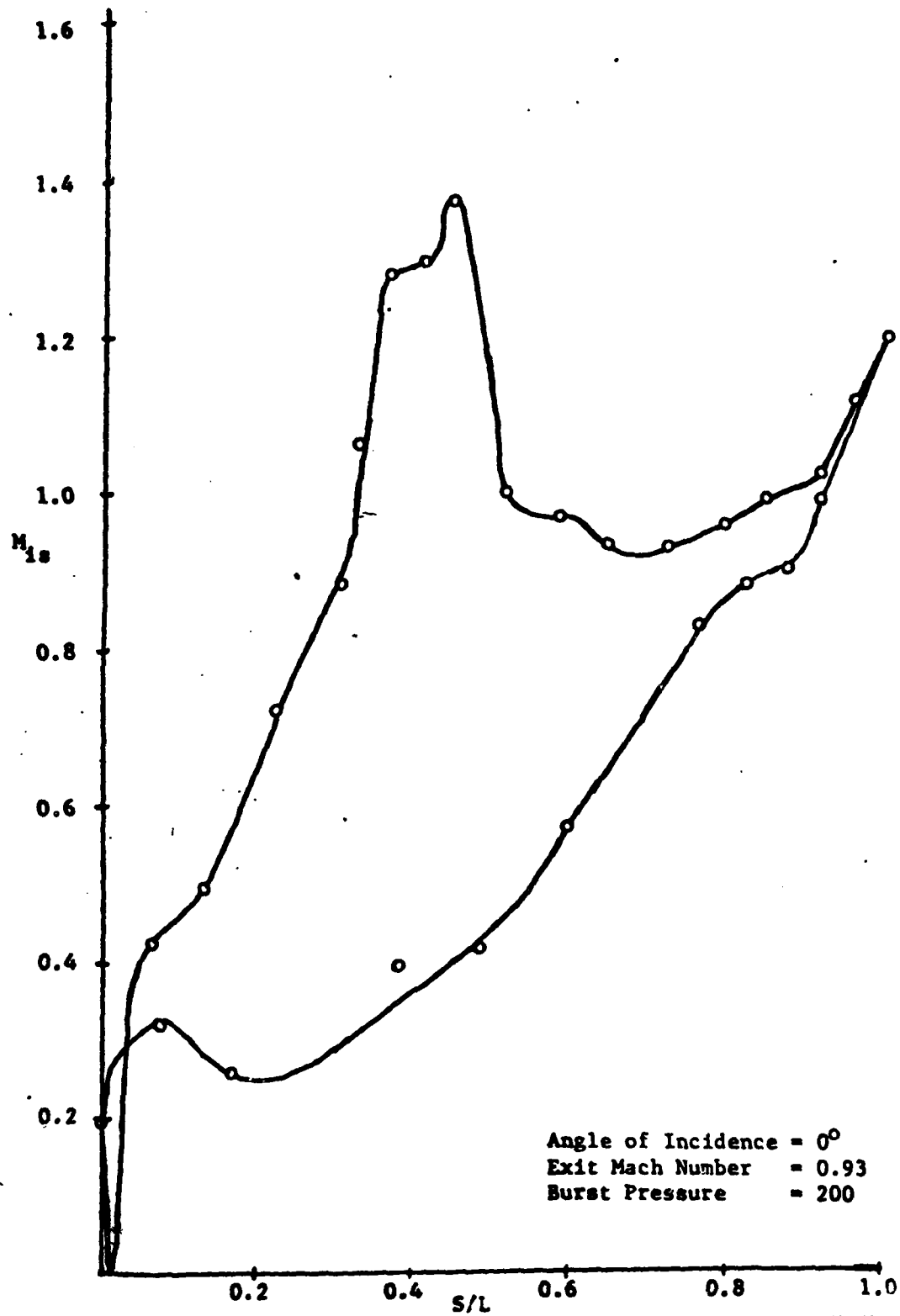
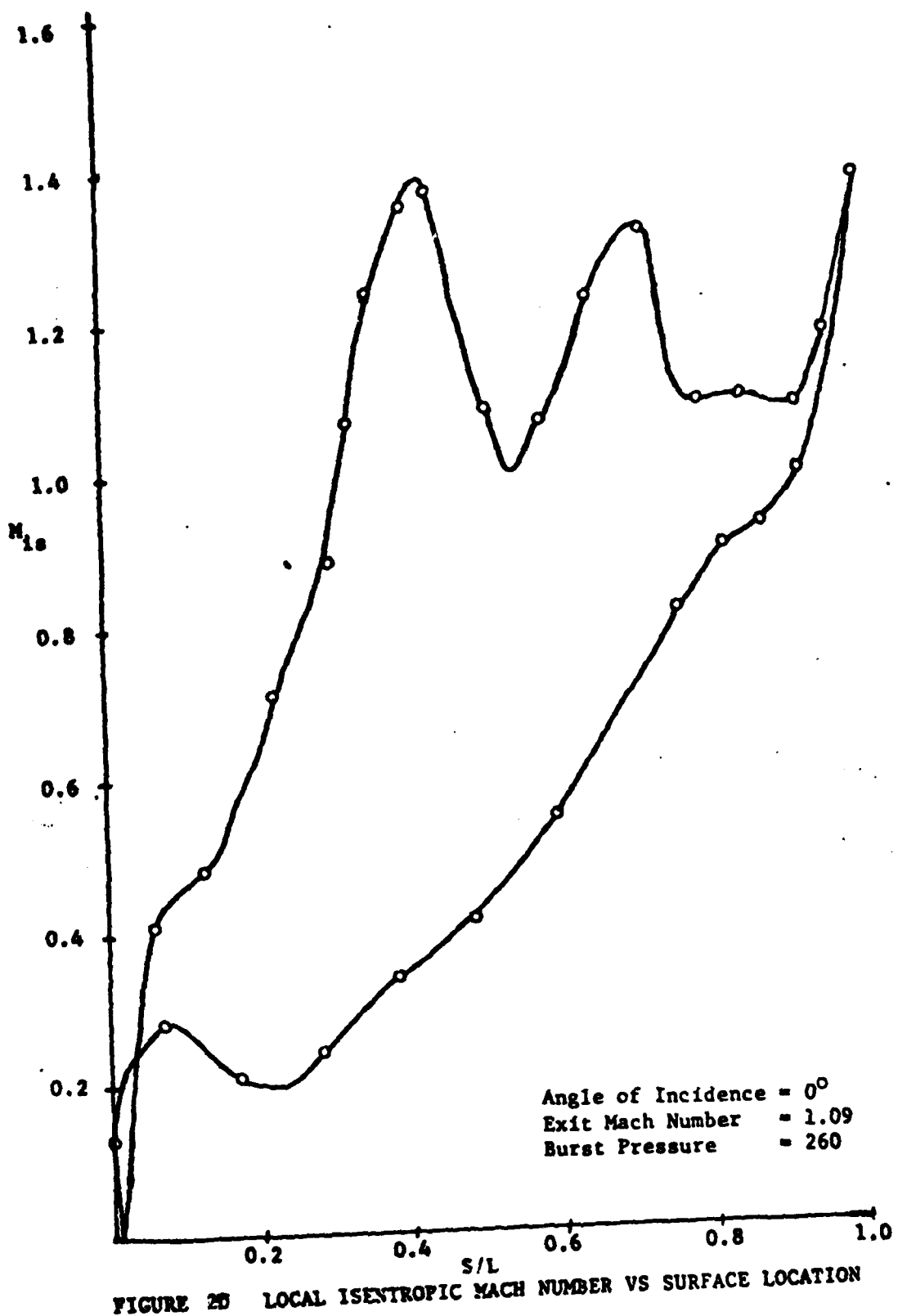


FIGURE 2C LOCAL ISENTROPIC MACH NUMBER VS SURFACE LOCATION



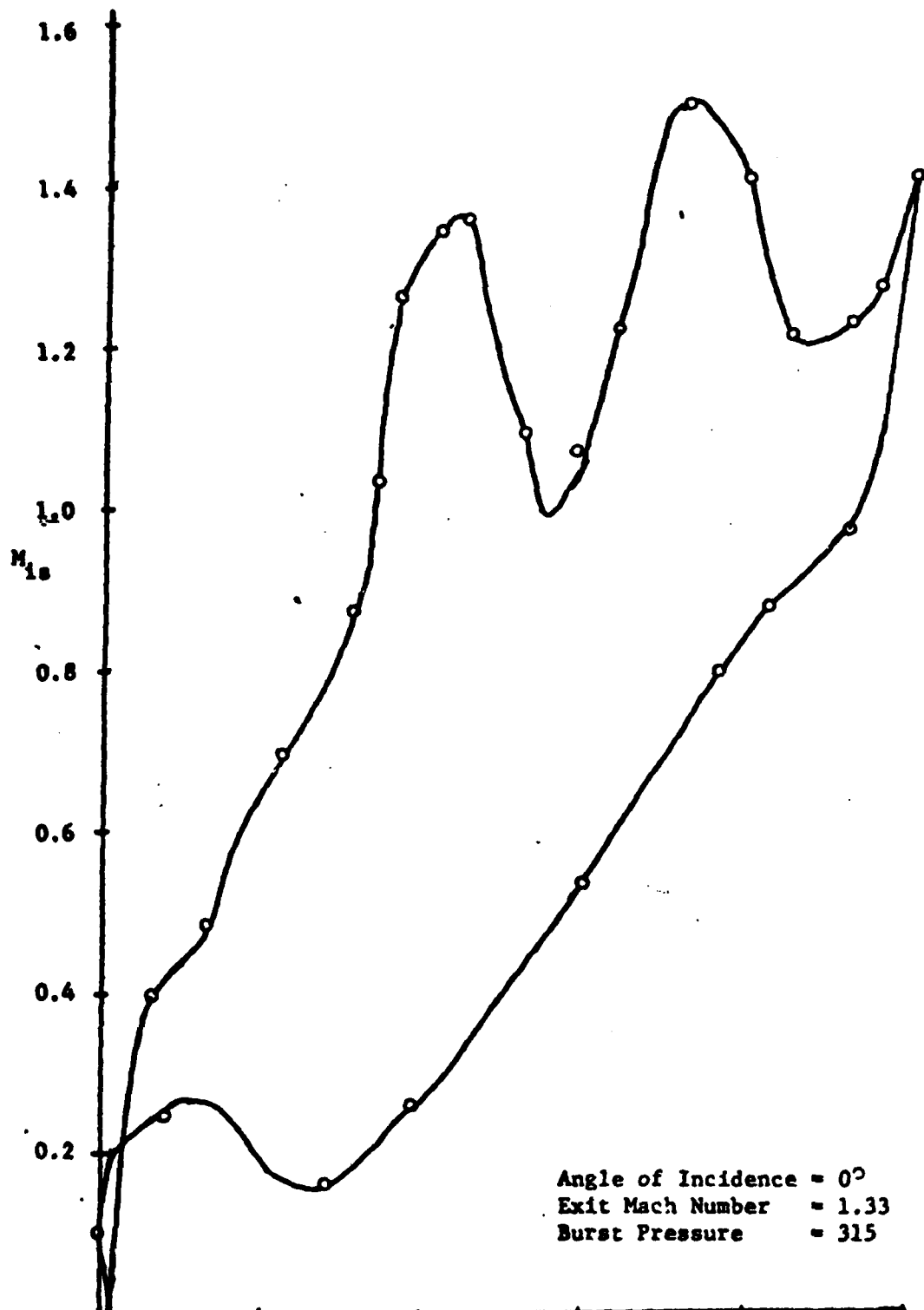


FIGURE 24. LOCAL ISENTROPIC MACH NUMBER VS SURFACE LOCATION

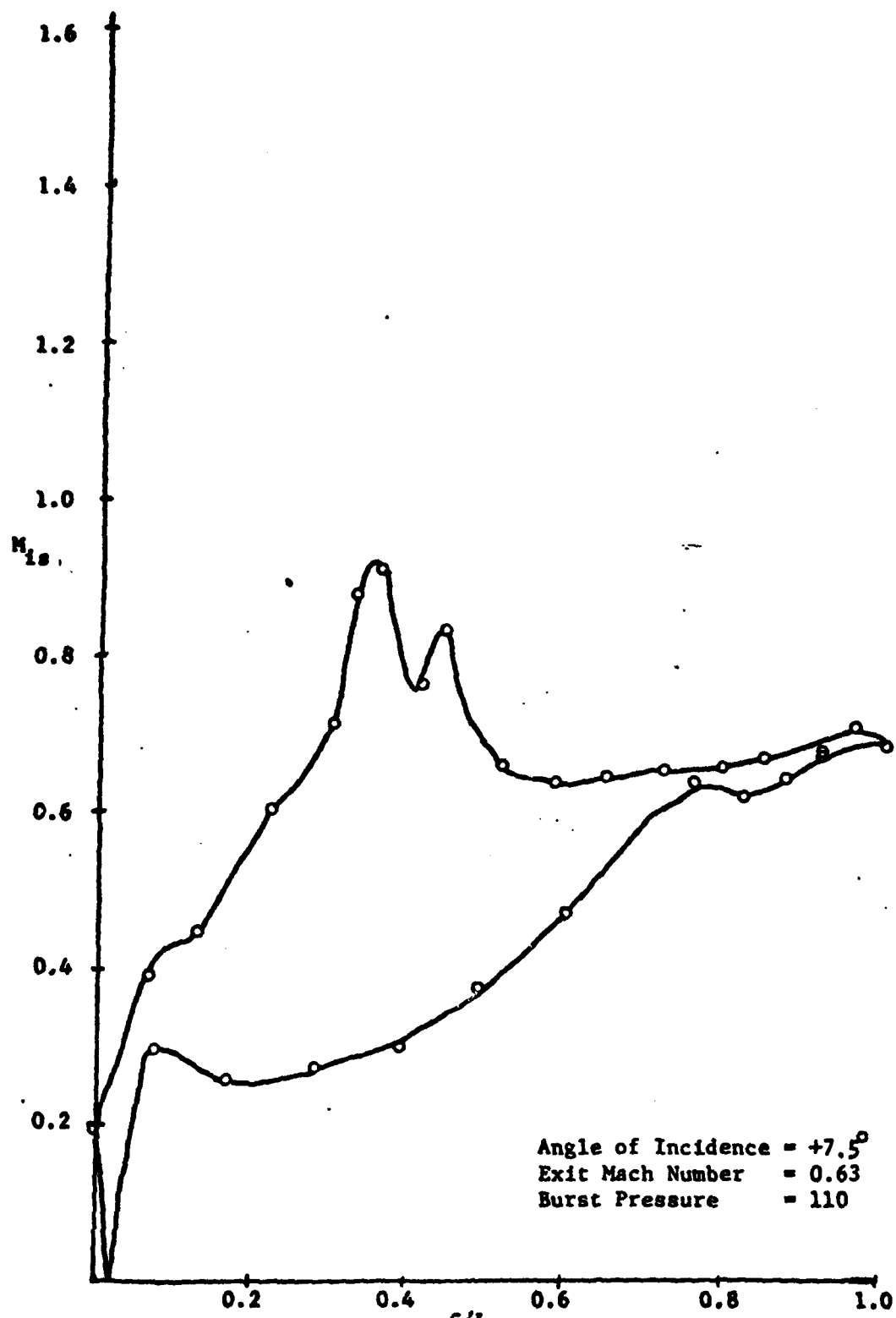


FIGURE 3A - LOCAL ISENTROPIC MACH NUMBER VS SURFACE LOCATION

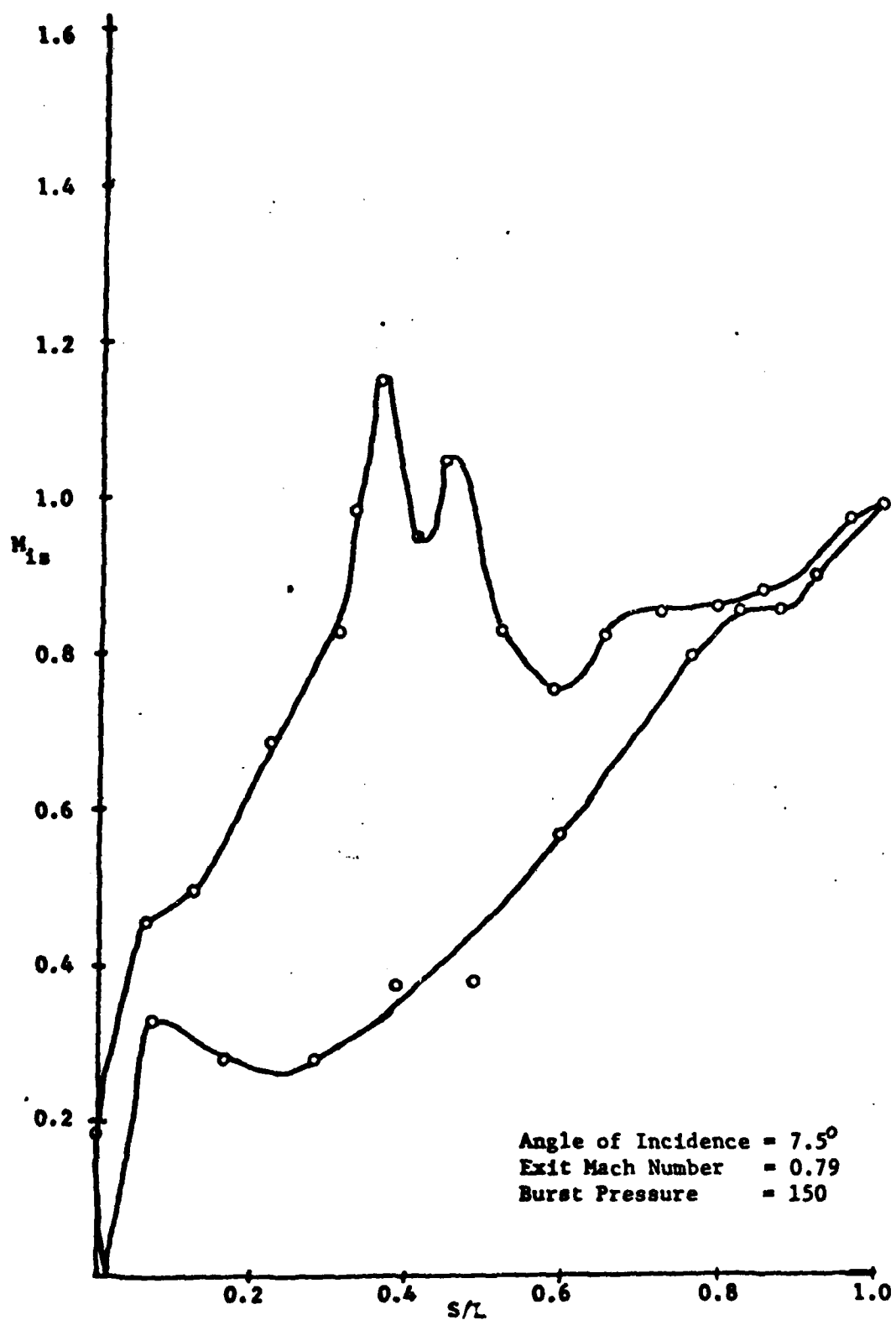


FIGURE 2 LOCAL ISENTROPIC MACH NUMBER VS SURFACE LOCATION

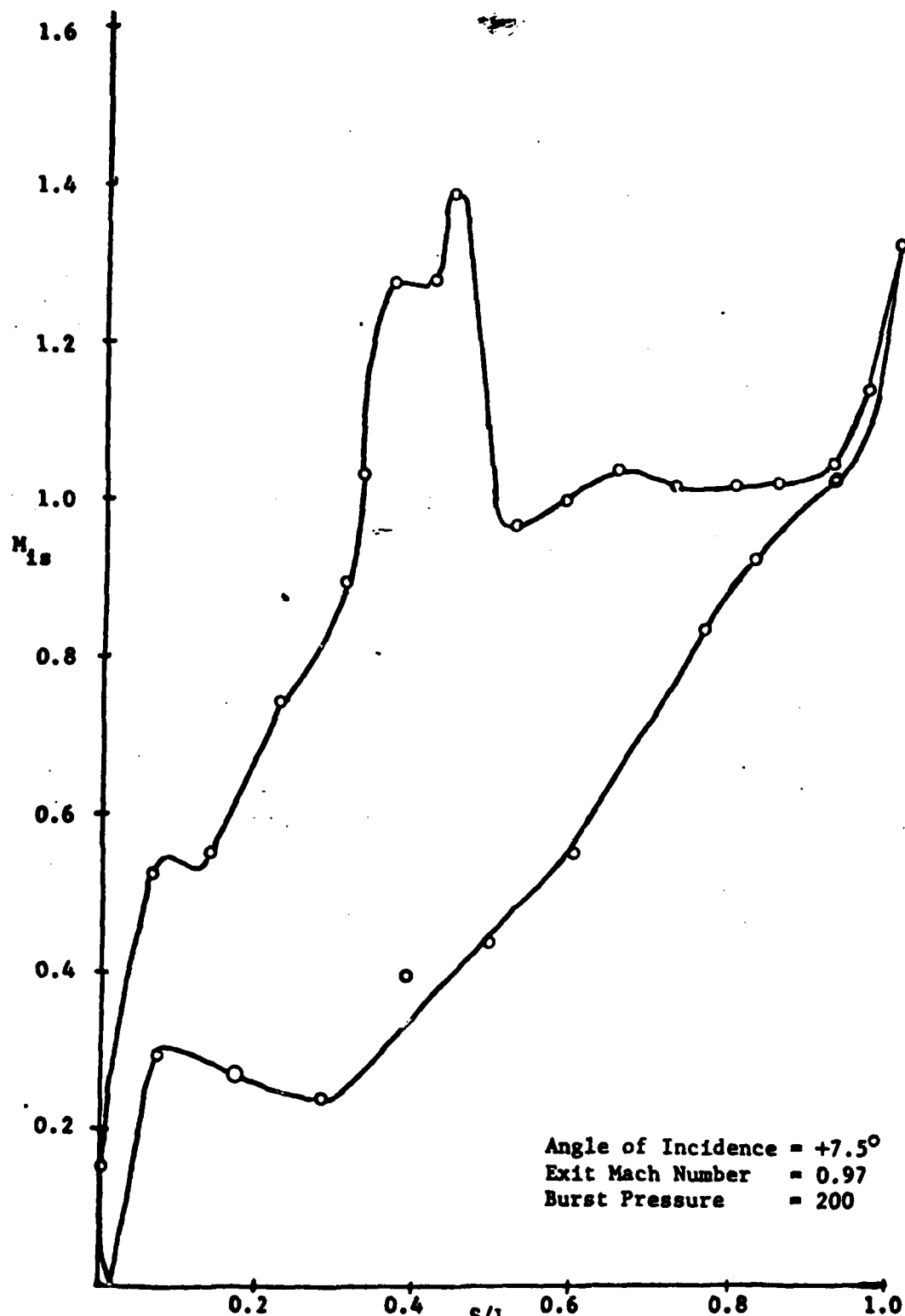


FIGURE 38. LOCAL ISENTROPIC MACH NUMBER VS SURFACE LOCATION

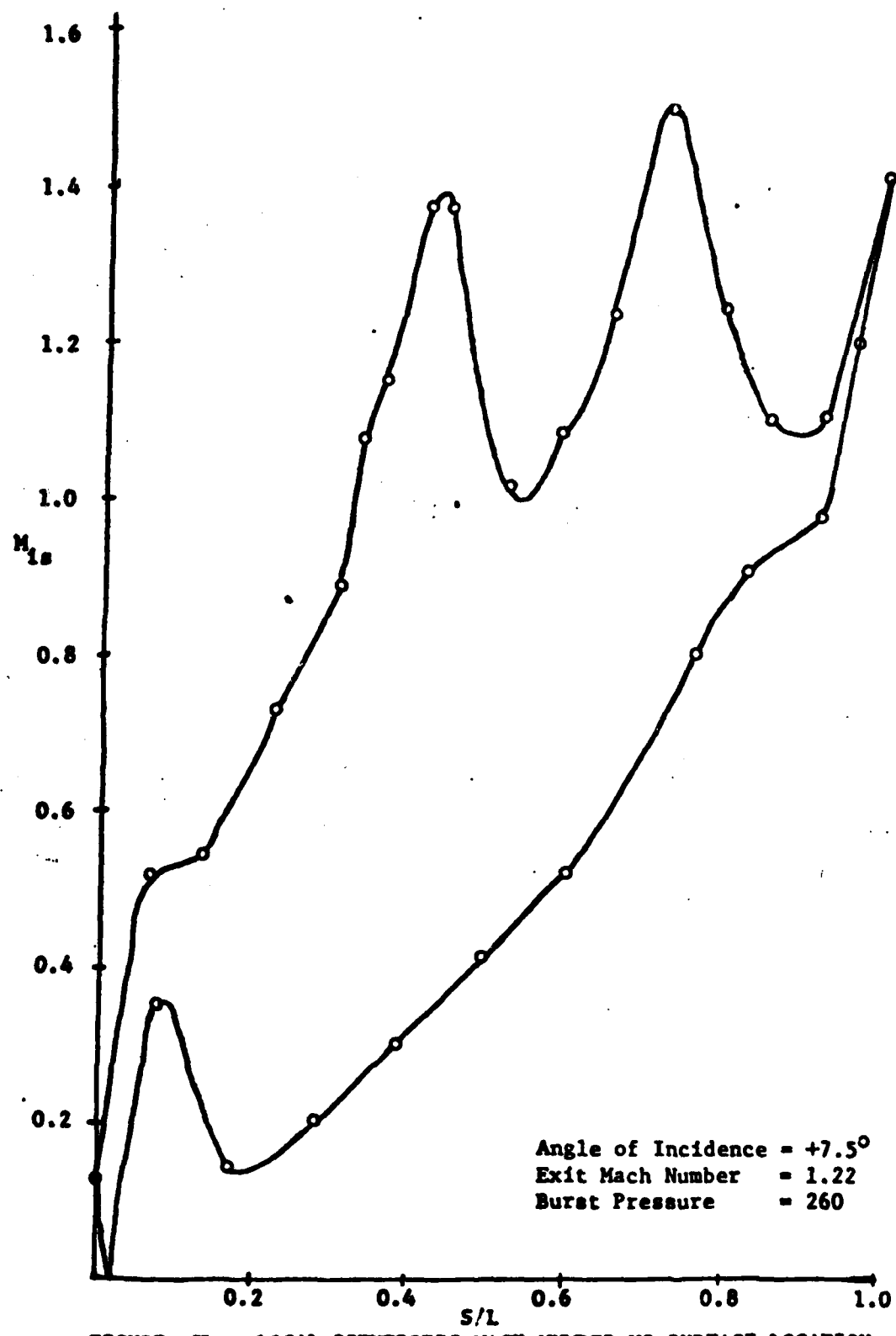


FIGURE 23D. LOCAL ISENTROPIC MACH NUMBER VS SURFACE LOCATION

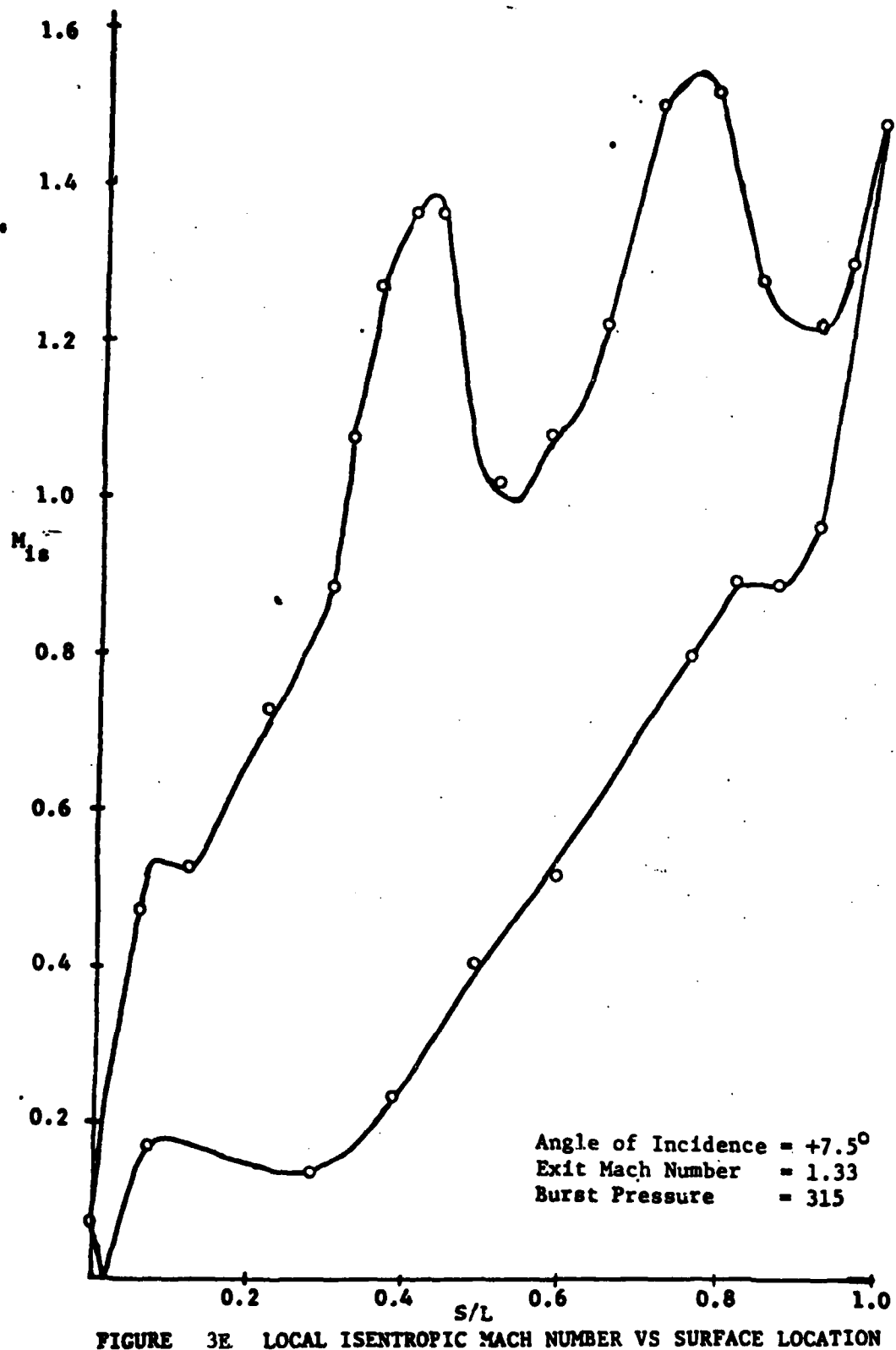


FIGURE 3E LOCAL ISENTROPIC MACH NUMBER VS SURFACE LOCATION

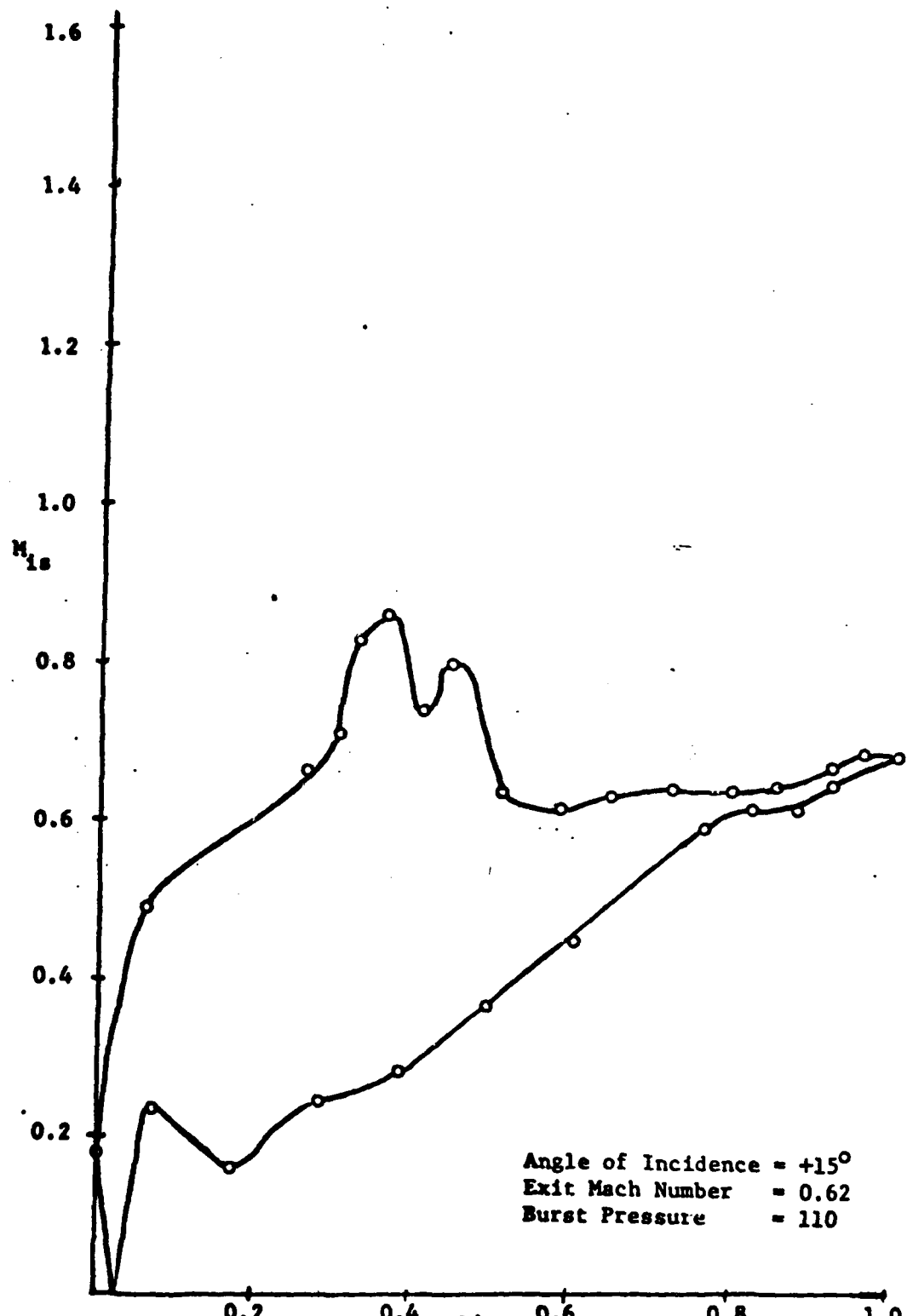


FIGURE 4A LOCAL ISENTROPIC MACH NUMBER VS SURFACE LOCATION

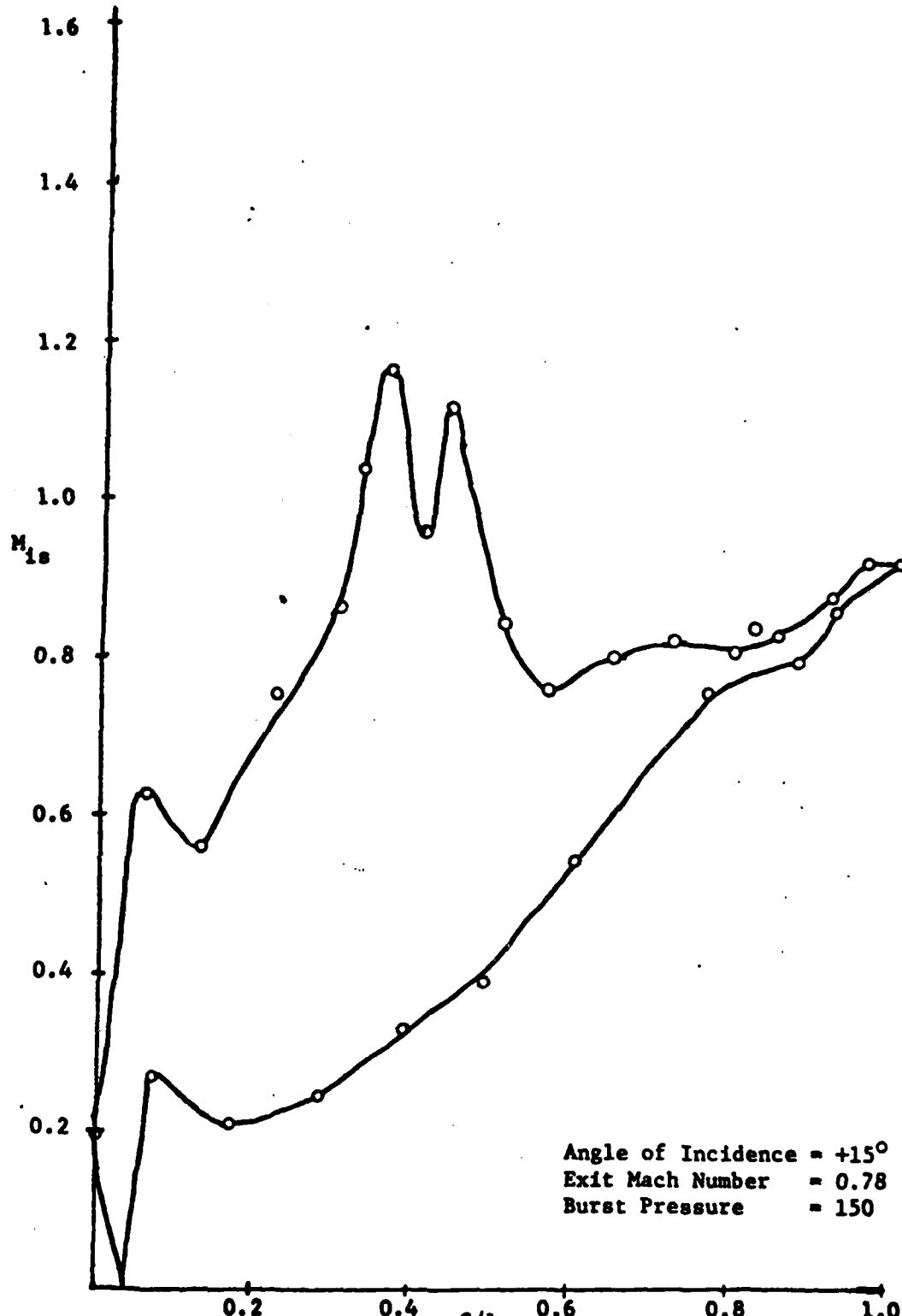


FIGURE 12 LOCAL ISENTROPIC MACH NUMBER VS SURFACE LOCATION

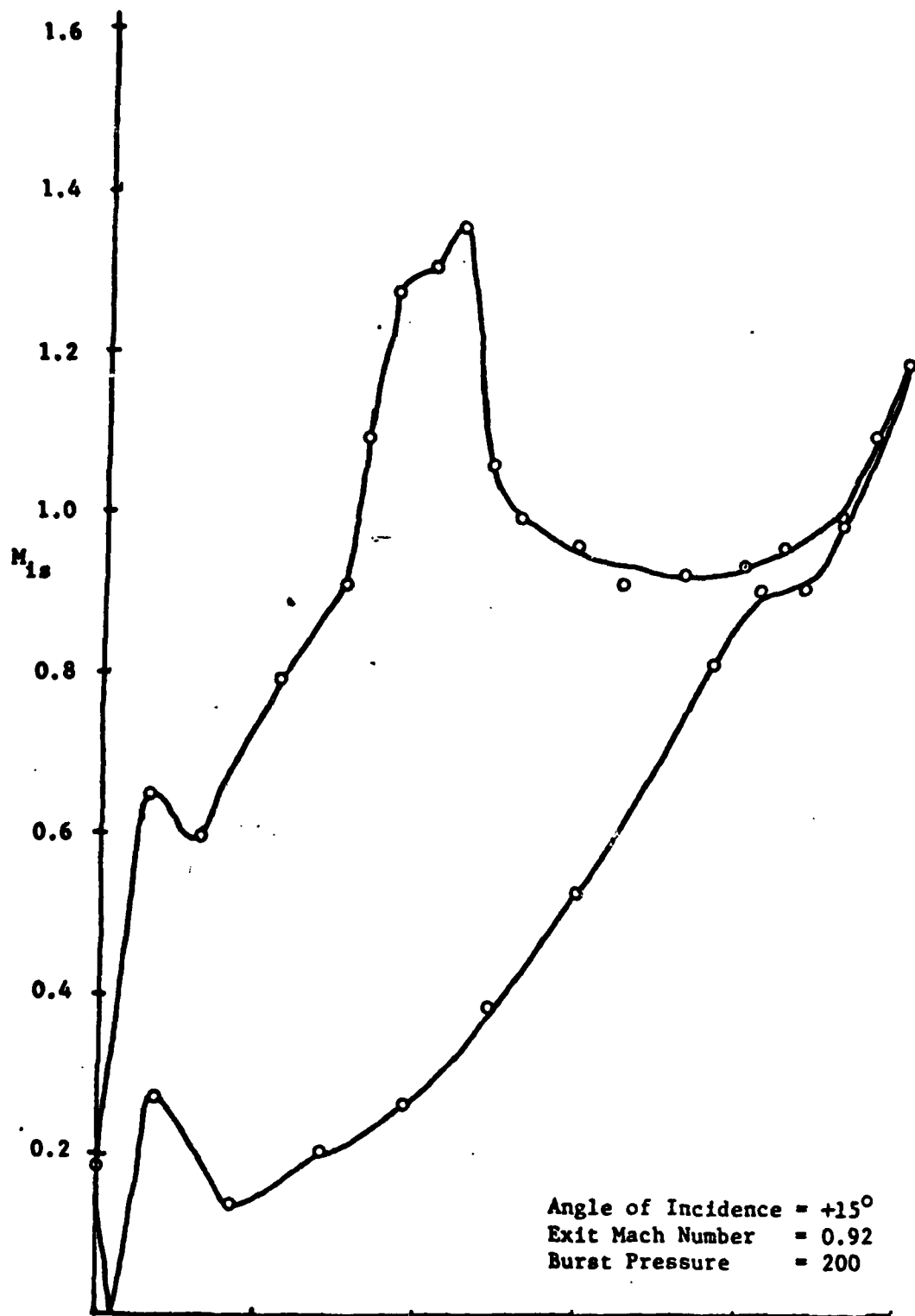


FIGURE 14C LOCAL ISENTROPIC MACH NUMBER VS SURFACE LOCATION

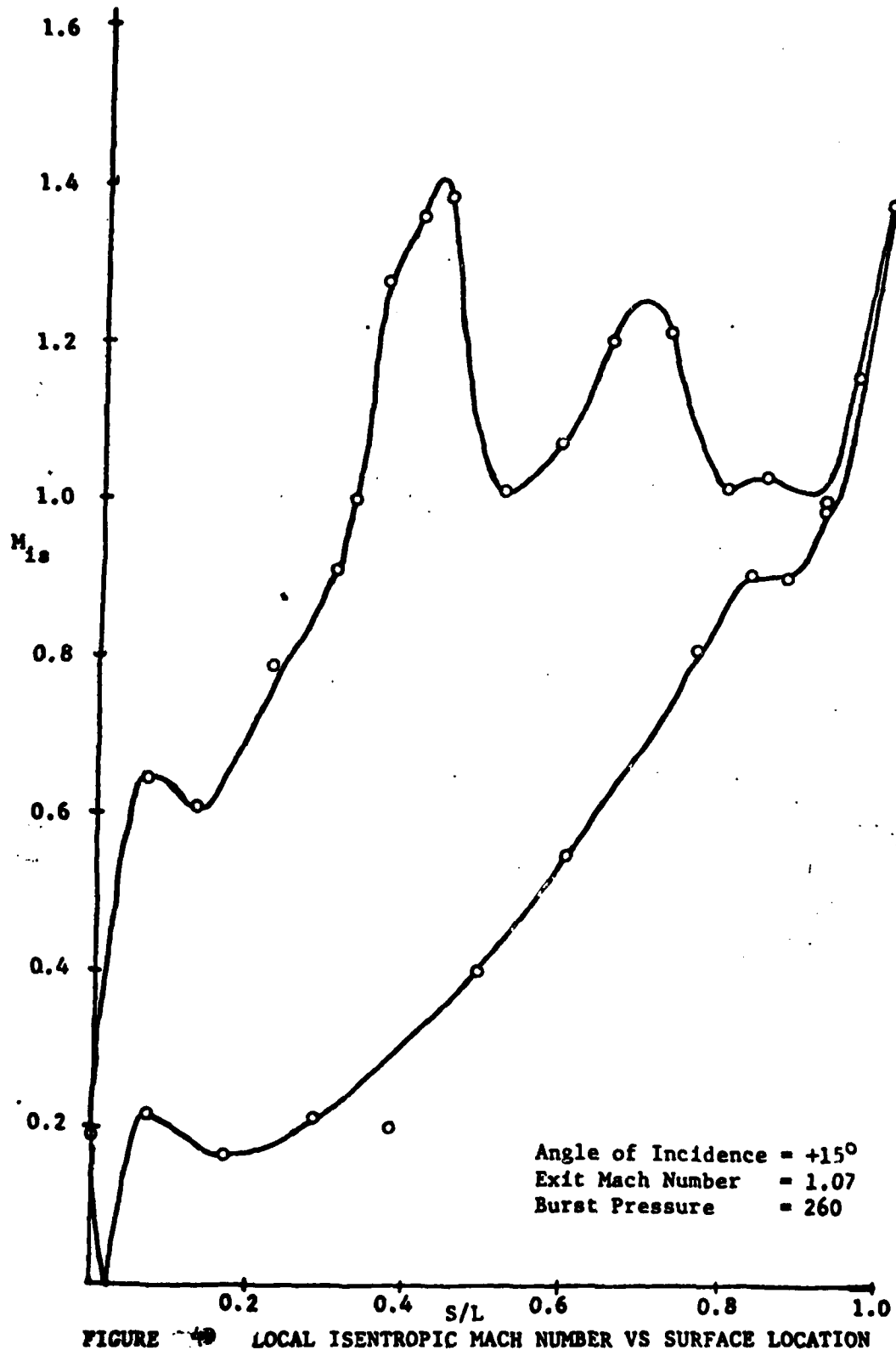


FIGURE 49 LOCAL ISENTROPIC MACH NUMBER VS SURFACE LOCATION

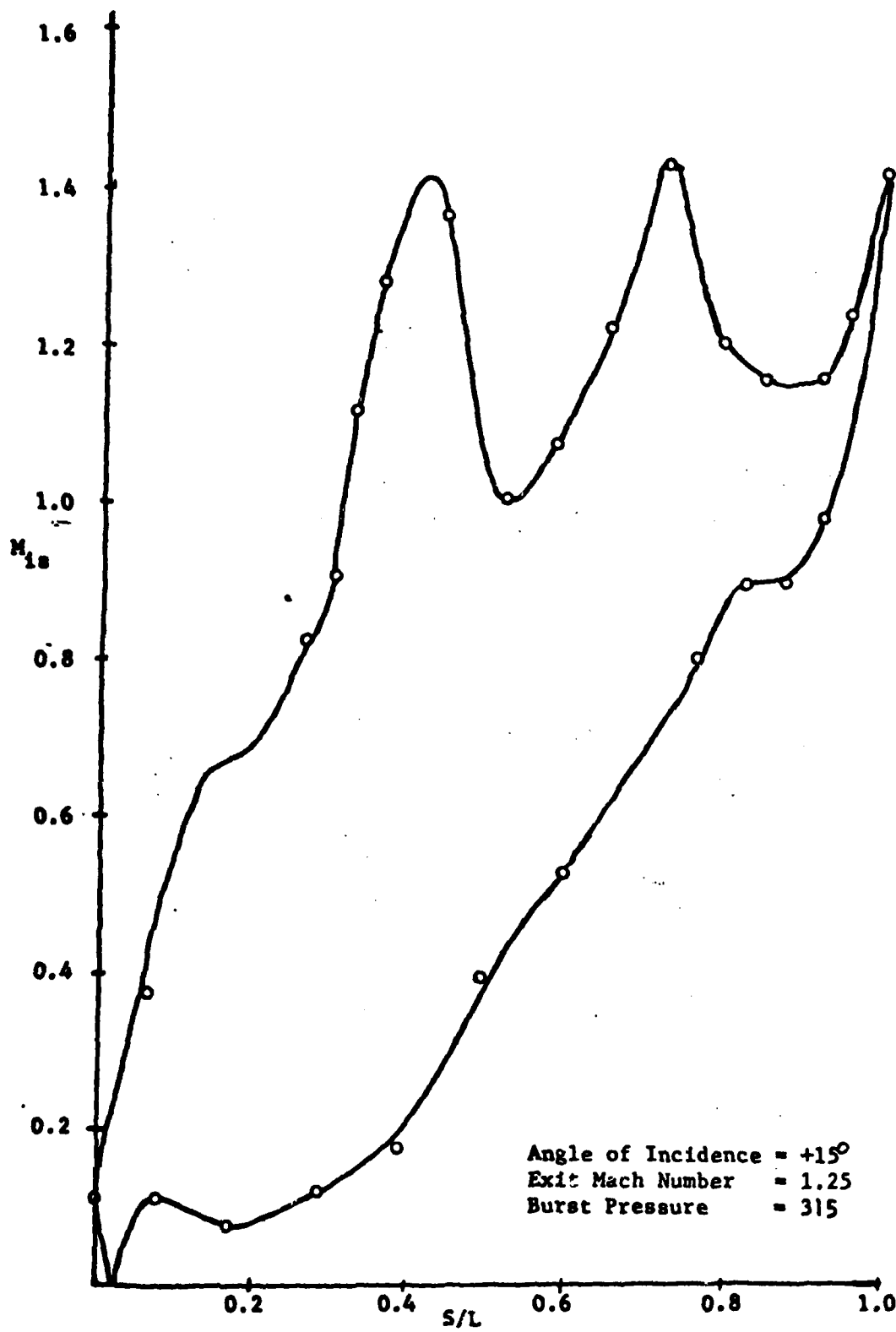


FIGURE 4E LOCAL ISENTROPIC MACH NUMBER VS SURFACE LOCATION

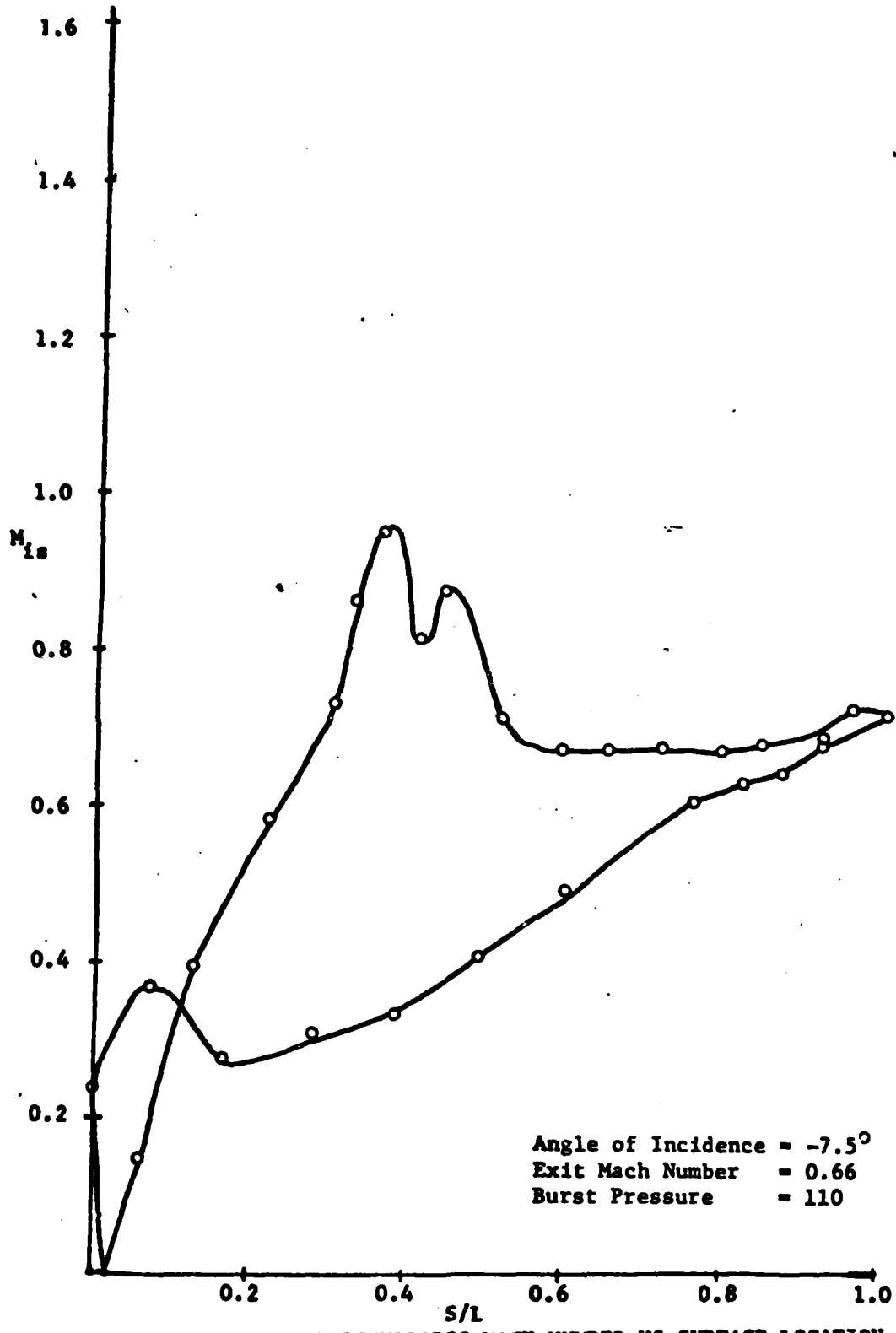


FIGURE 5A LOCAL ISENTROPIC MACH NUMBER VS SURFACE LOCATION

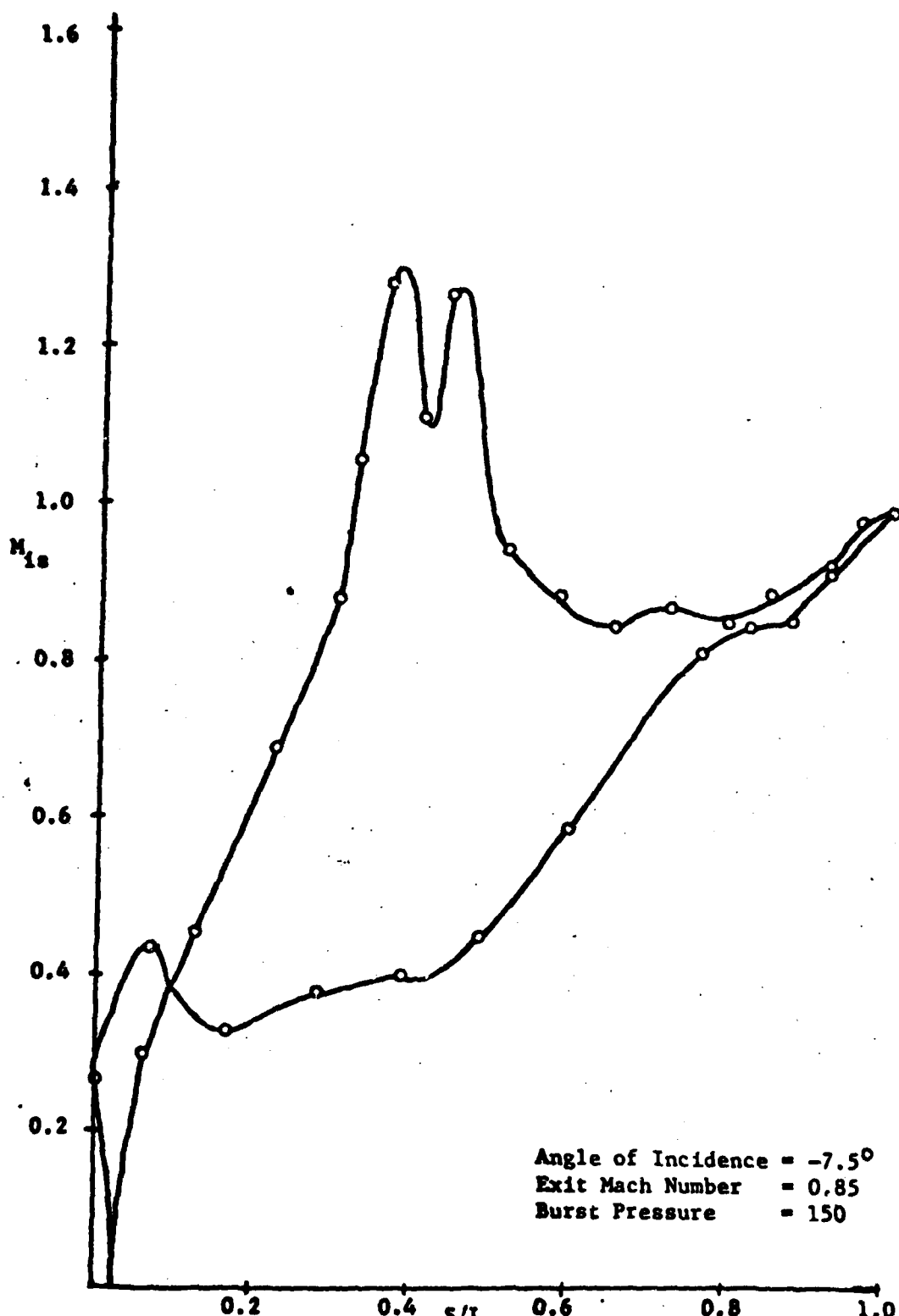


FIGURE 5B. LOCAL ISENTROPIC MACH NUMBER VS SURFACE LOCATION

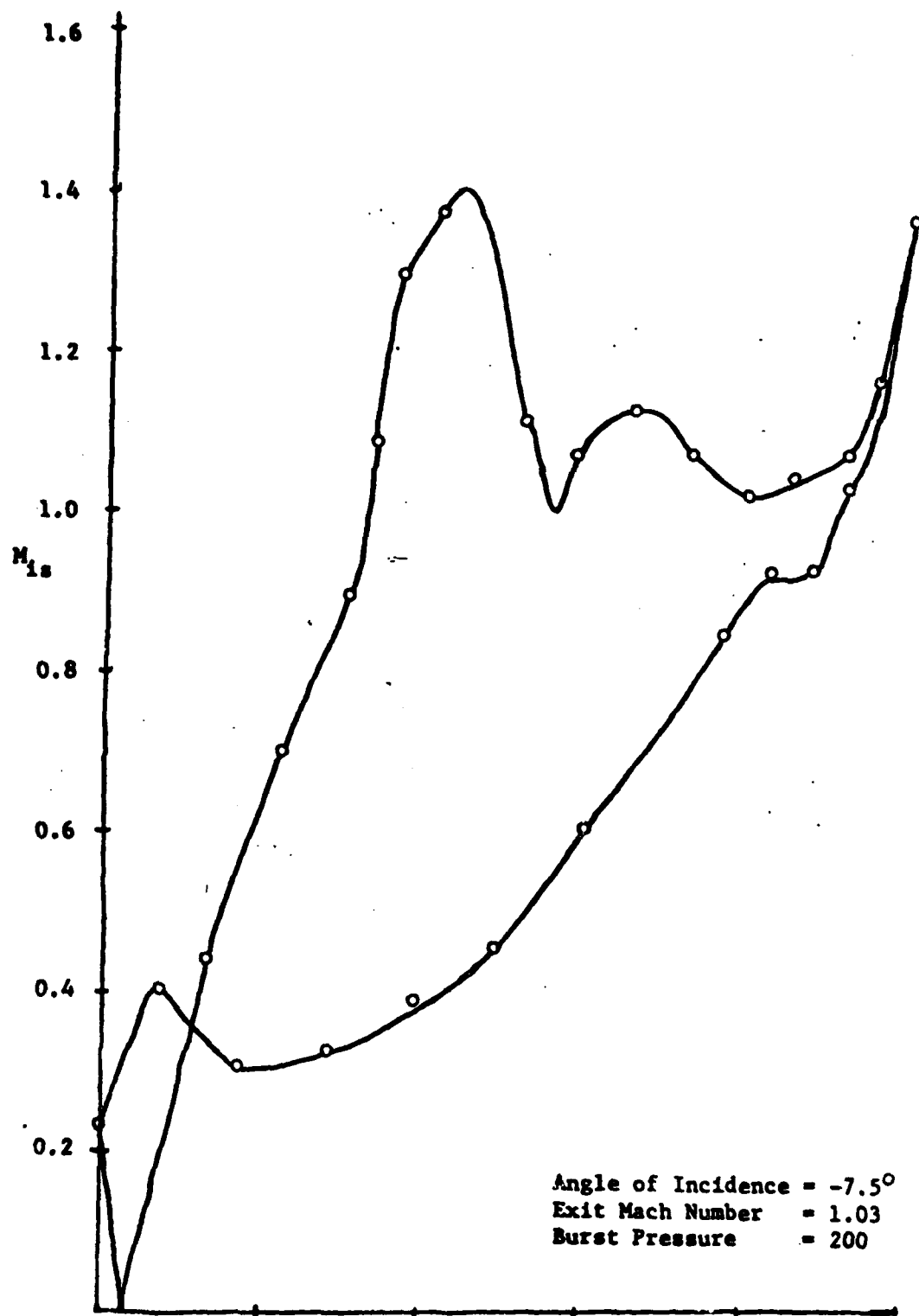


FIGURE 50 LOCAL ISENTROPIC MACH NUMBER VS SURFACE LOCATION

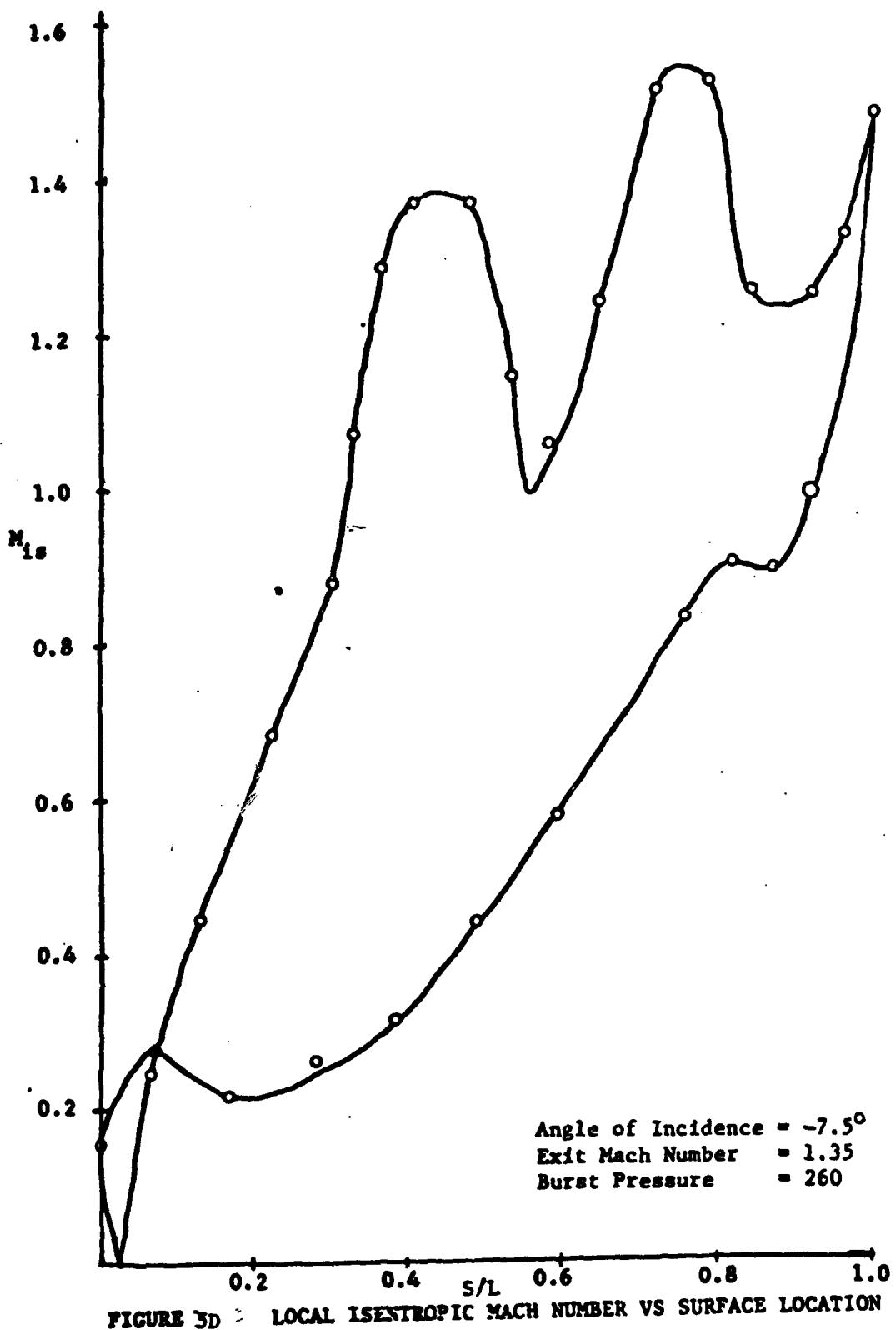


FIGURE 3D : LOCAL ISENTROPIC MACH NUMBER VS SURFACE LOCATION

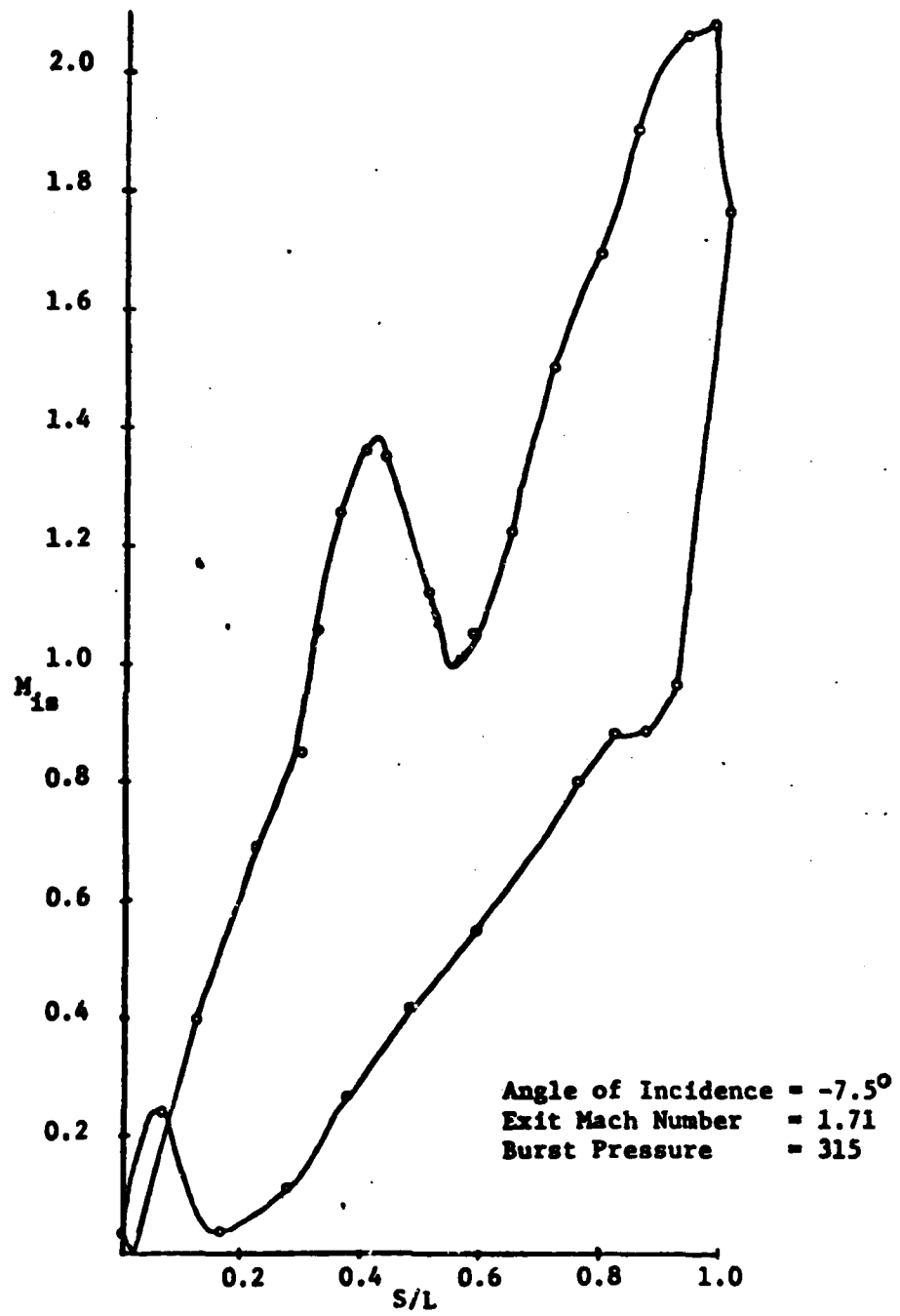


FIGURE 5E LOCAL ISENTROPIC MACH NUMBER VS SURFACE LOCATION

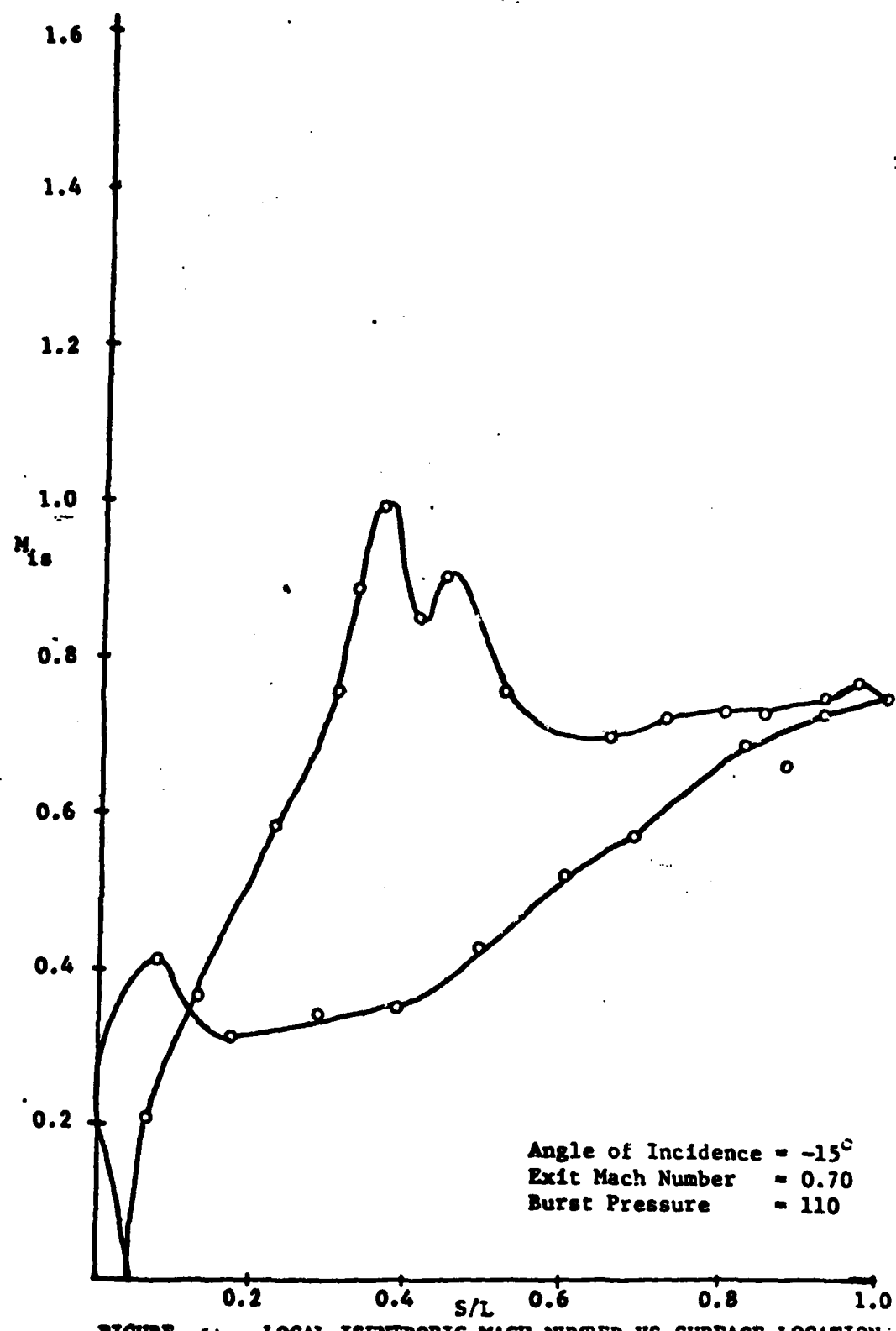


FIGURE .6A LOCAL ISENTROPIC MACH NUMBER VS SURFACE LOCATION

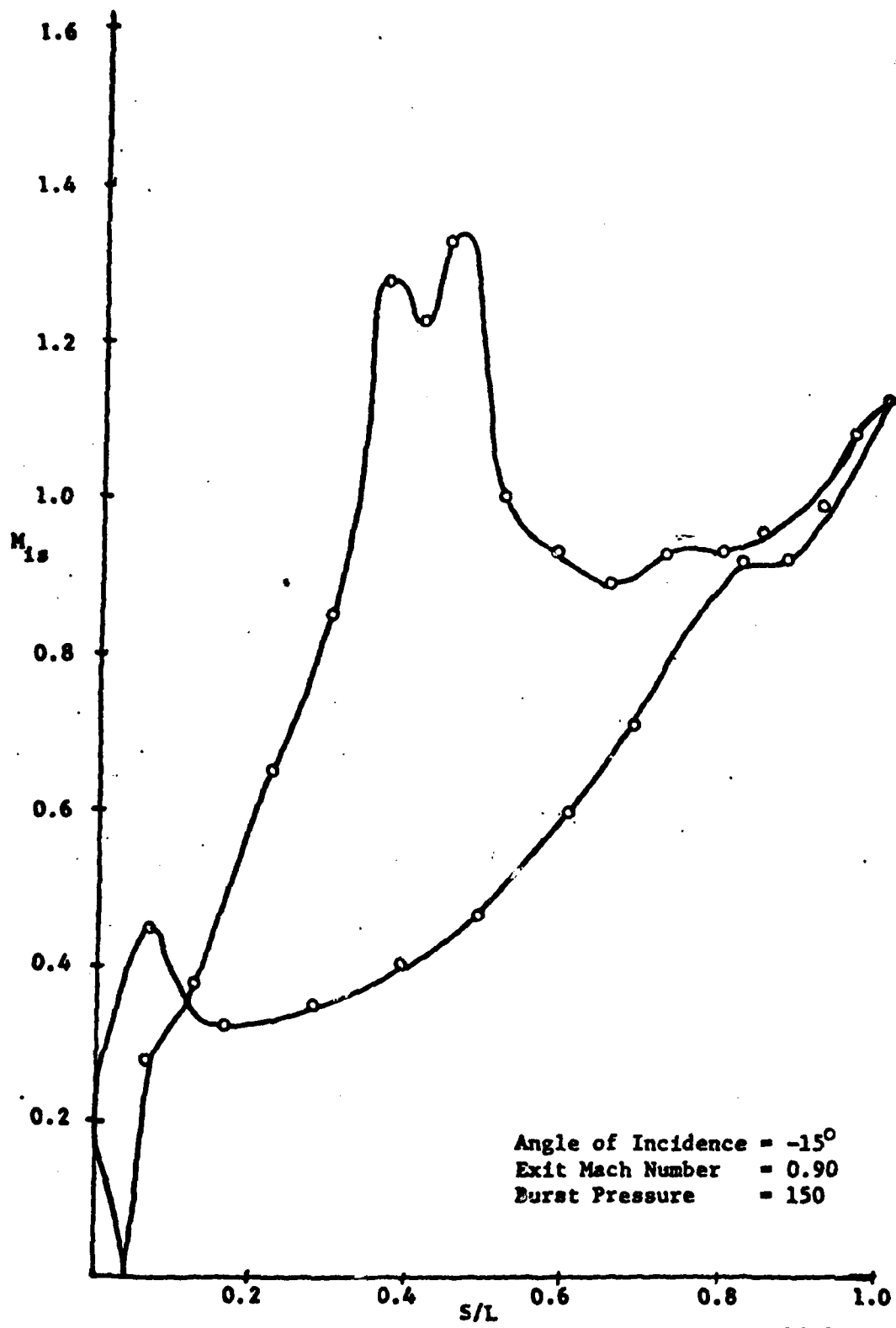


FIGURE 6B LOCAL ISENTROPIC MACH NUMBER VS SURFACE LOCATION

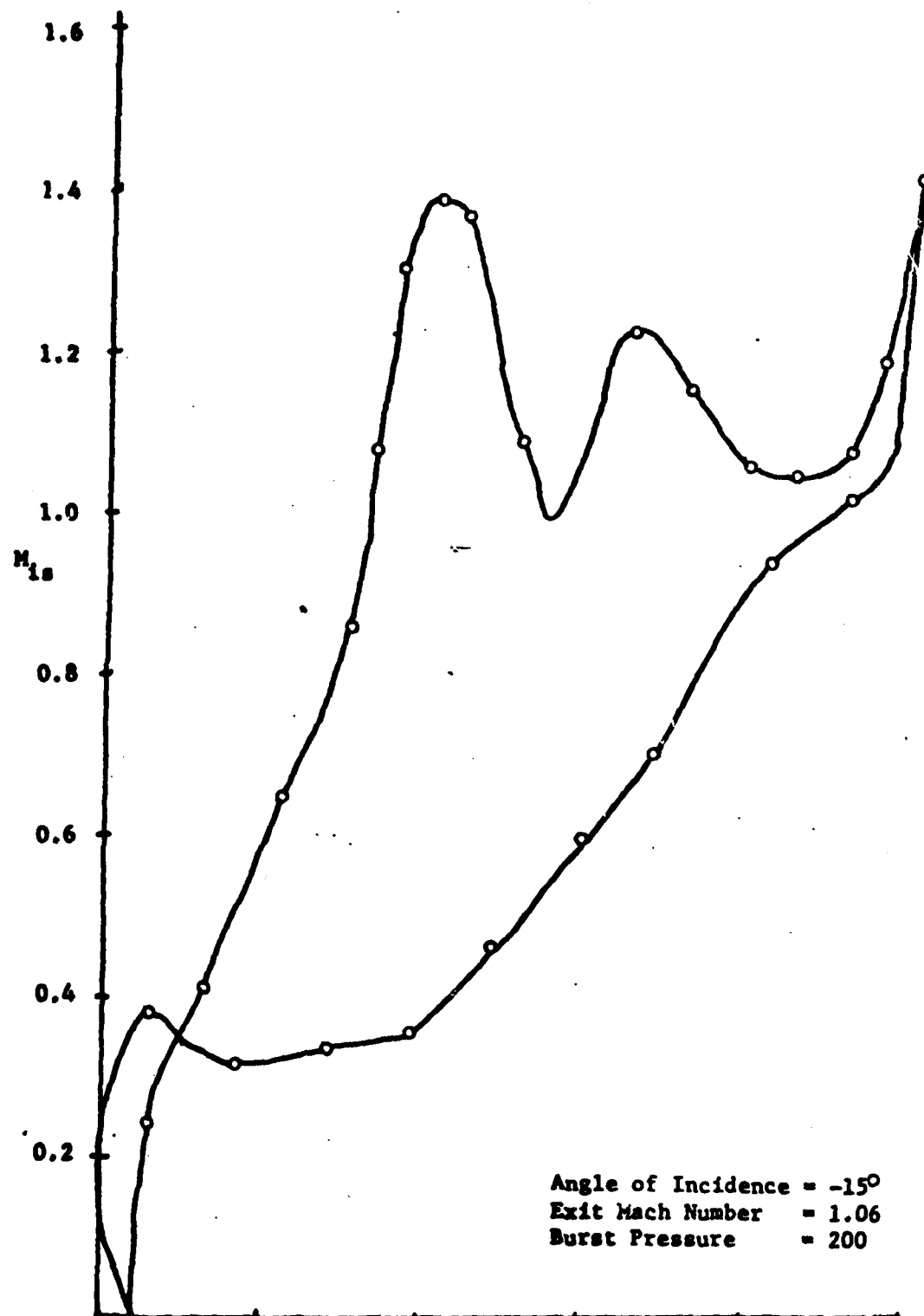


FIGURE 16a LOCAL ISENTROPIC MACH NUMBER VS SURFACE LOCATION

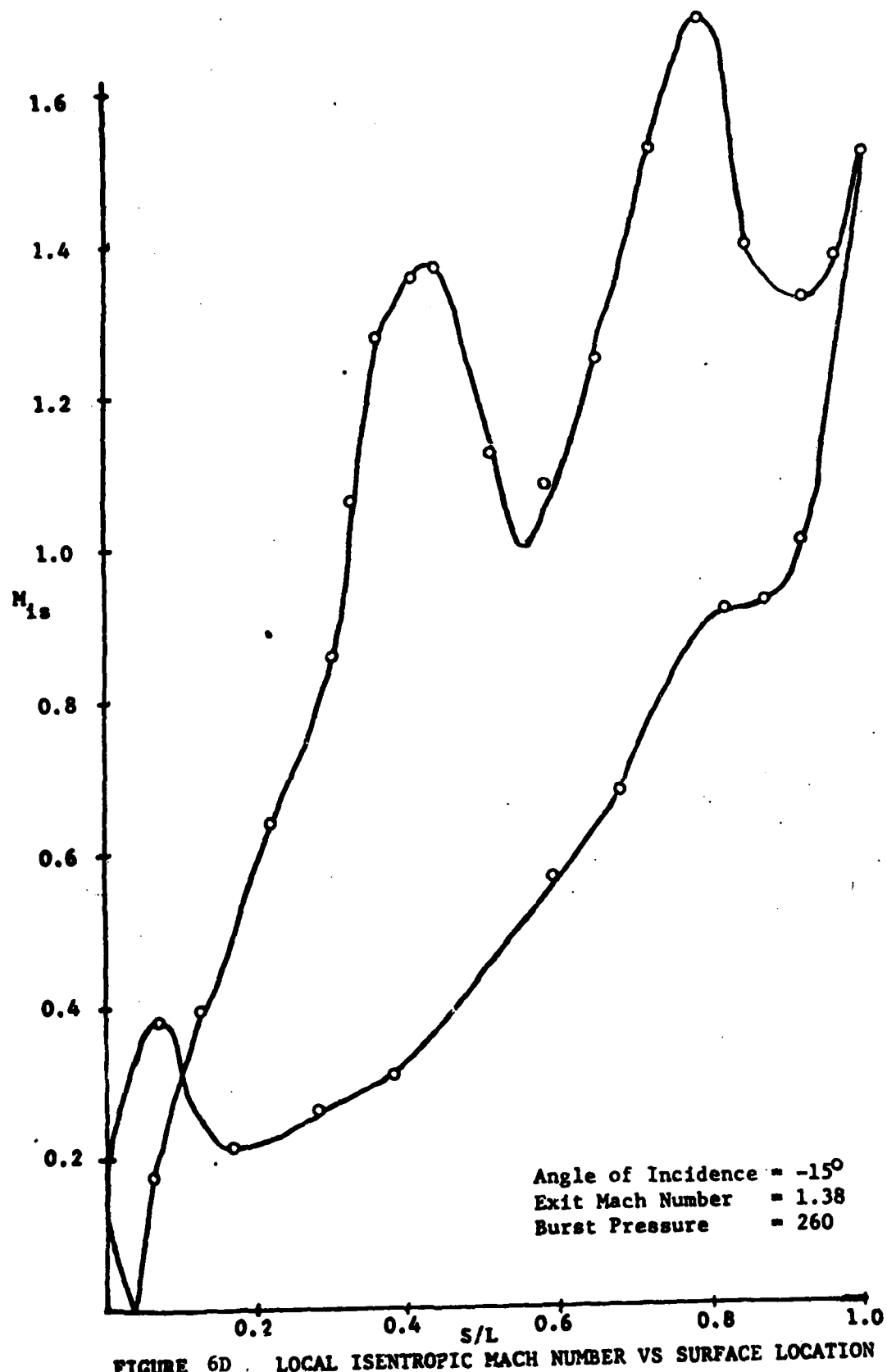


FIGURE 6D . LOCAL ISENTROPIC MACH NUMBER VS SURFACE LOCATION

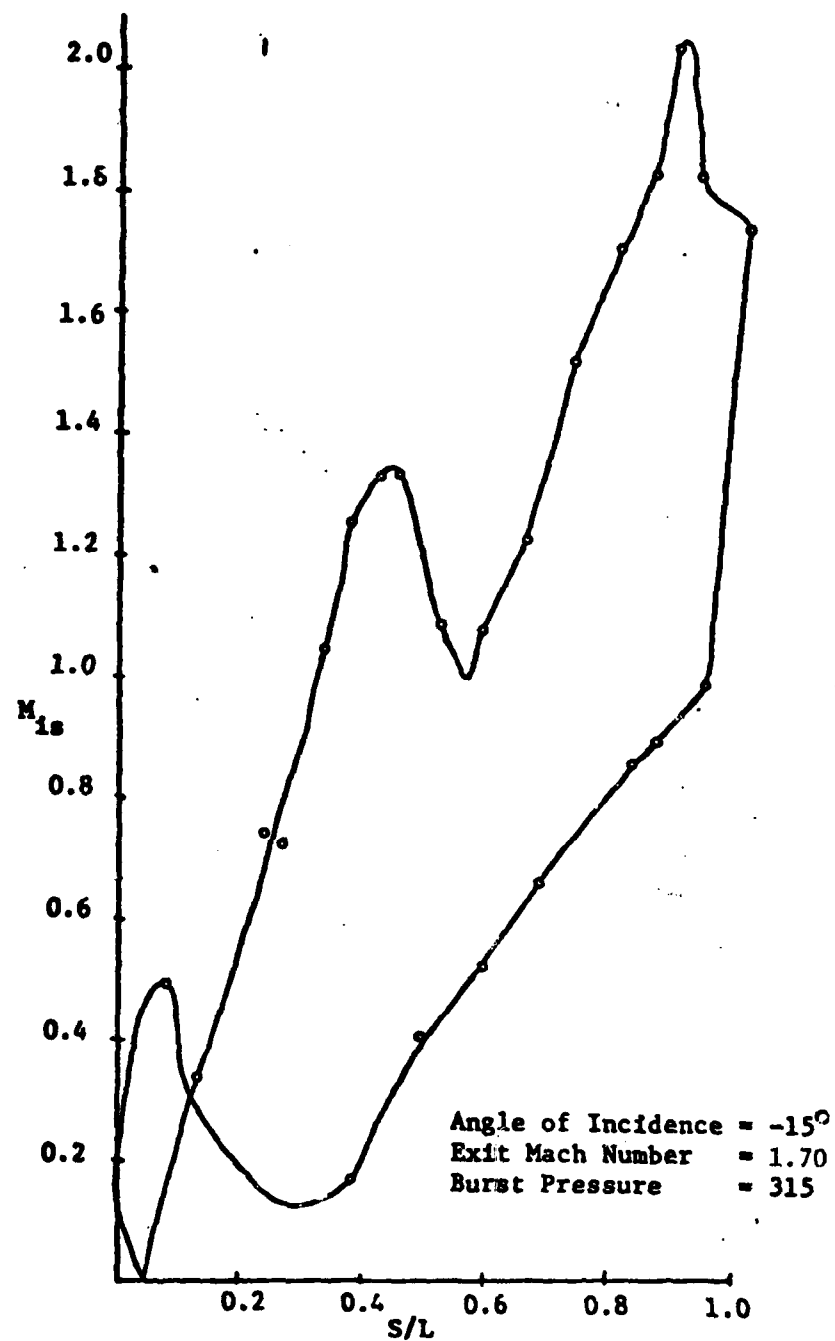


FIGURE 6E LOCAL ISENTROPIC MACH NUMBER VS SURFACE LOCATION

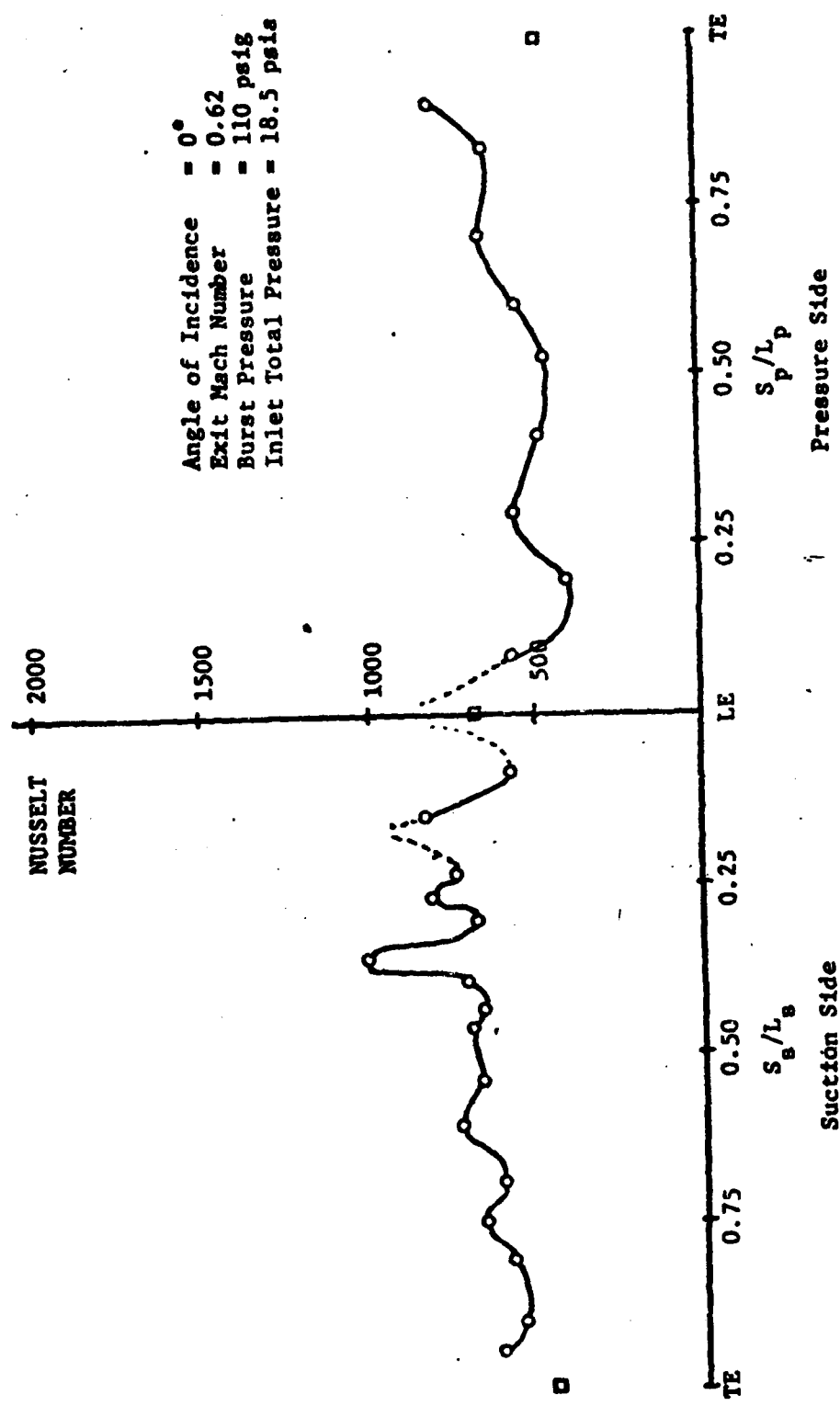


FIGURE 7A LOCAL NUSSELT NUMBER VS BLADE SURFACE LOCATION

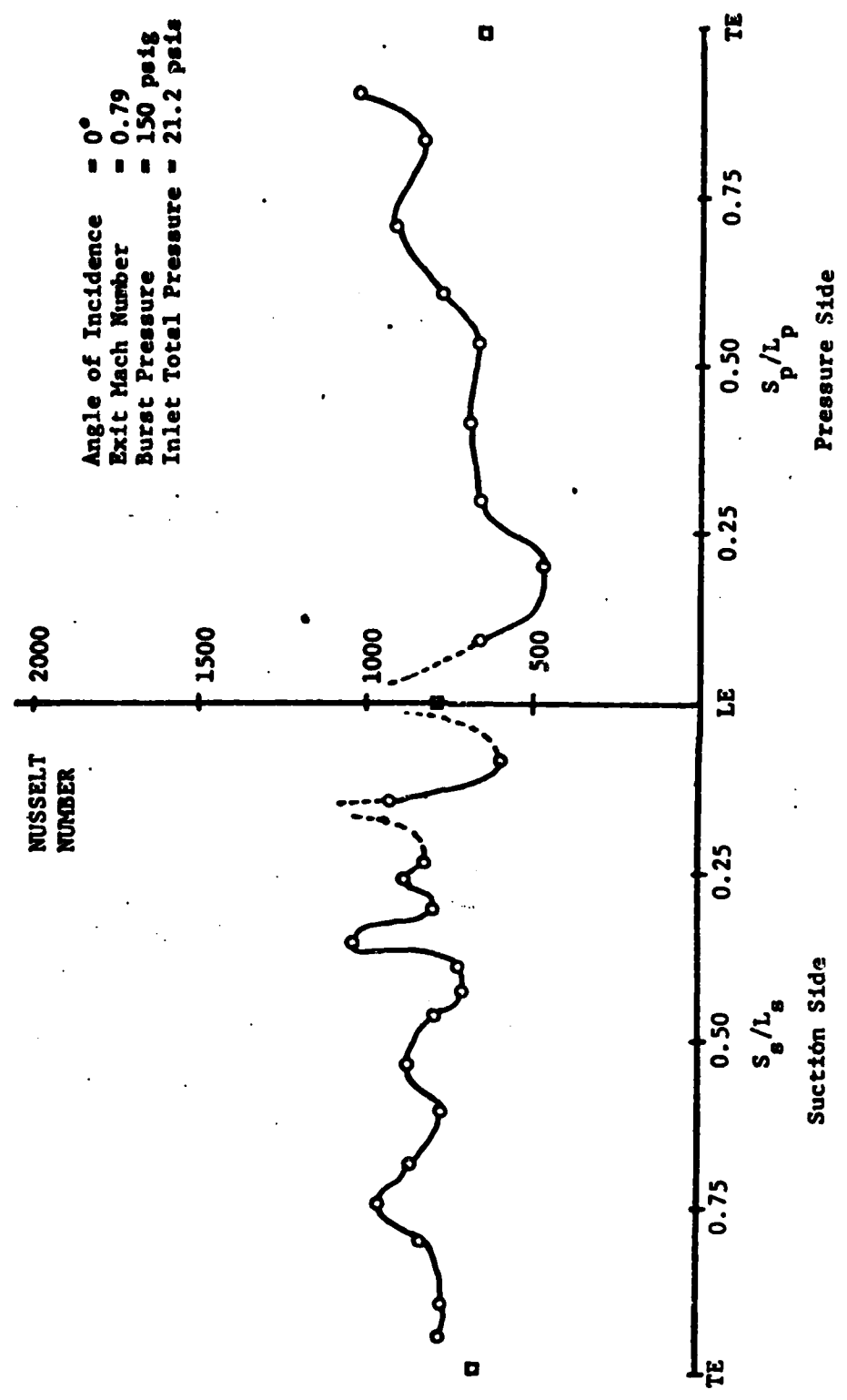


FIGURE 7B LOCAL NUSSELT NUMBER VS BLADE SURFACE LOCATION

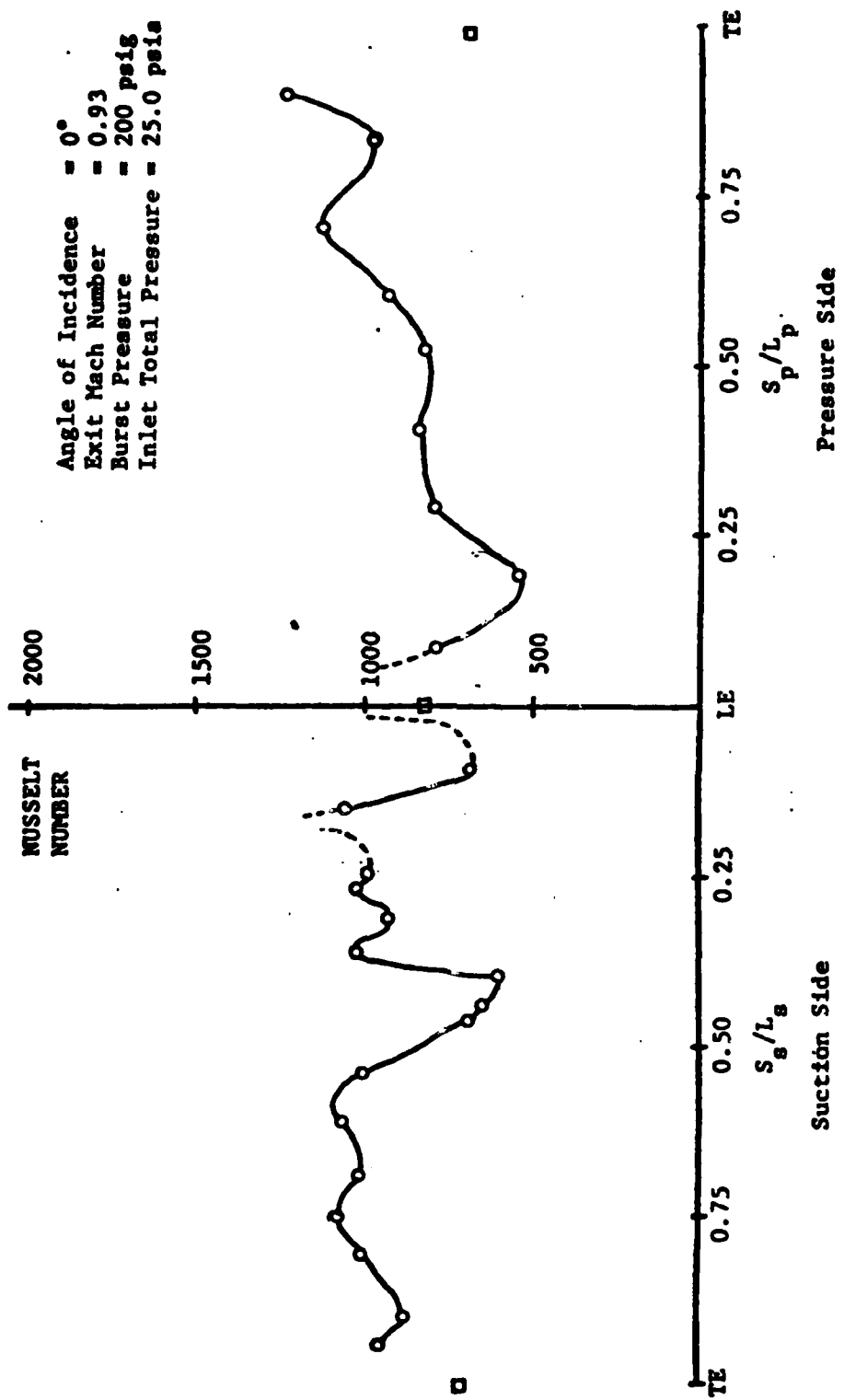


FIGURE 7C. LOCAL NUSSELT NUMBER VS BLADE SURFACE LOCATION

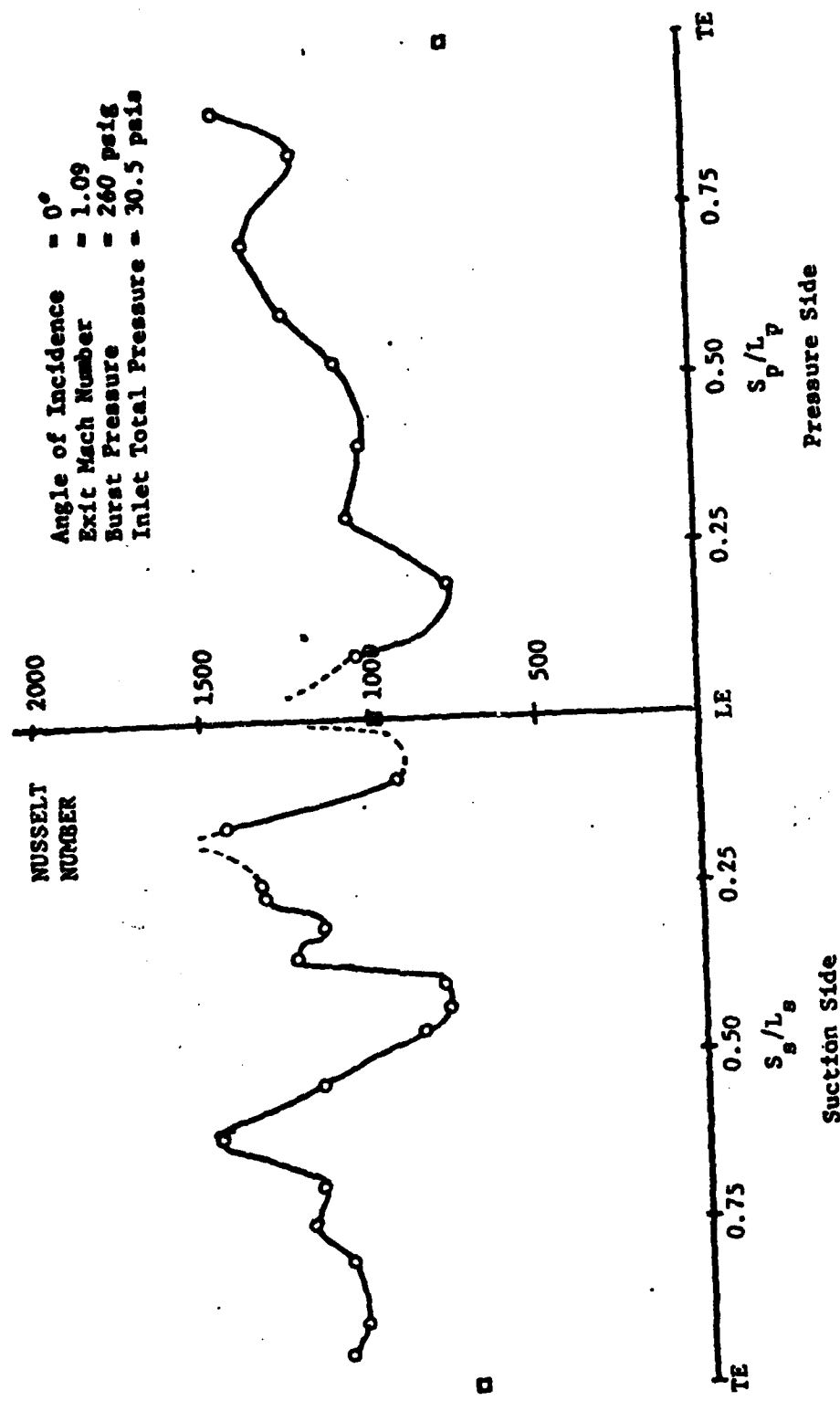


FIGURE 20. LOCAL NUSSELT NUMBER VS BLADE SURFACE LOCATION

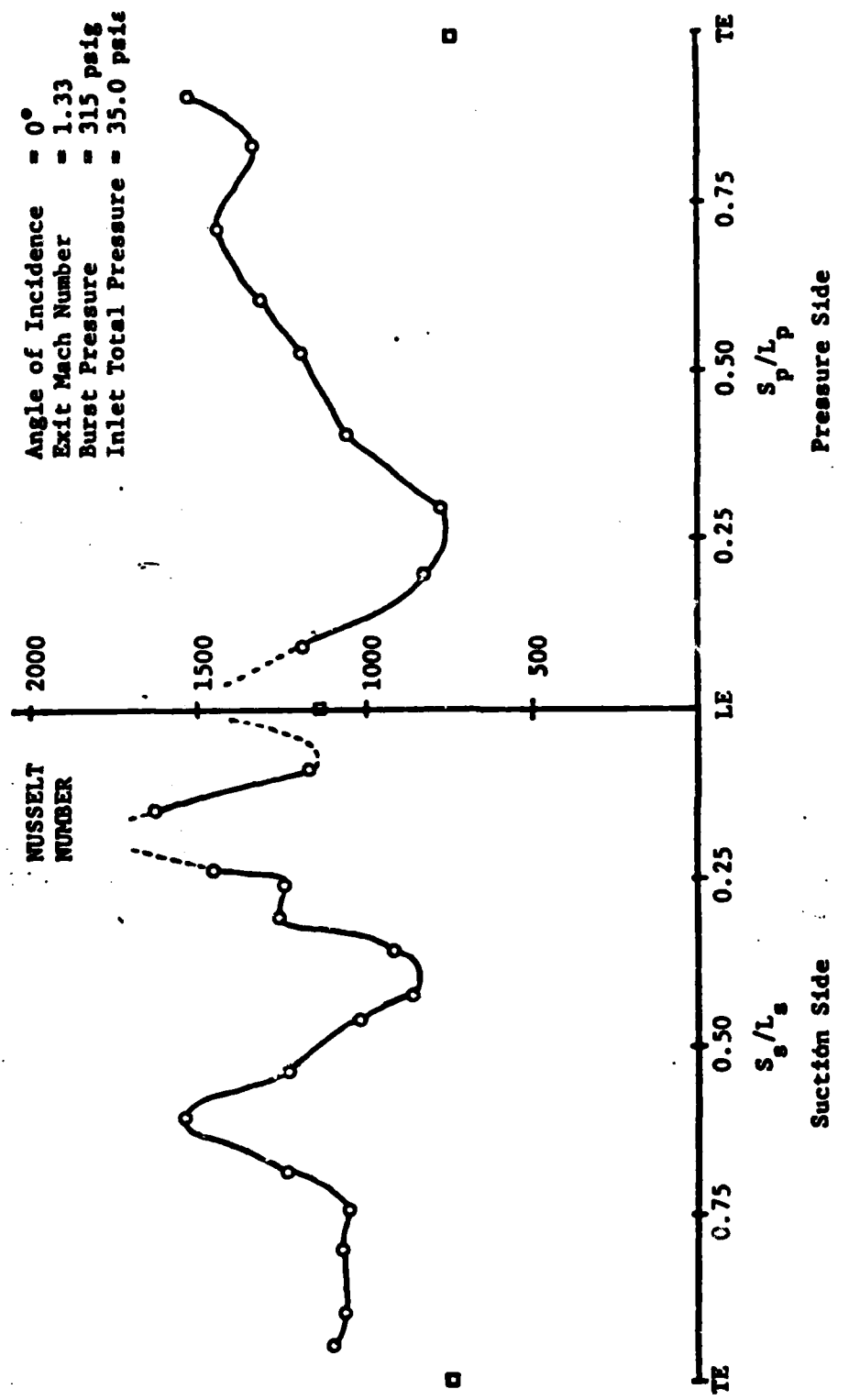


FIGURE 3a LOCAL NUSSELT NUMBER VS BLADE SURFACE LOCATION

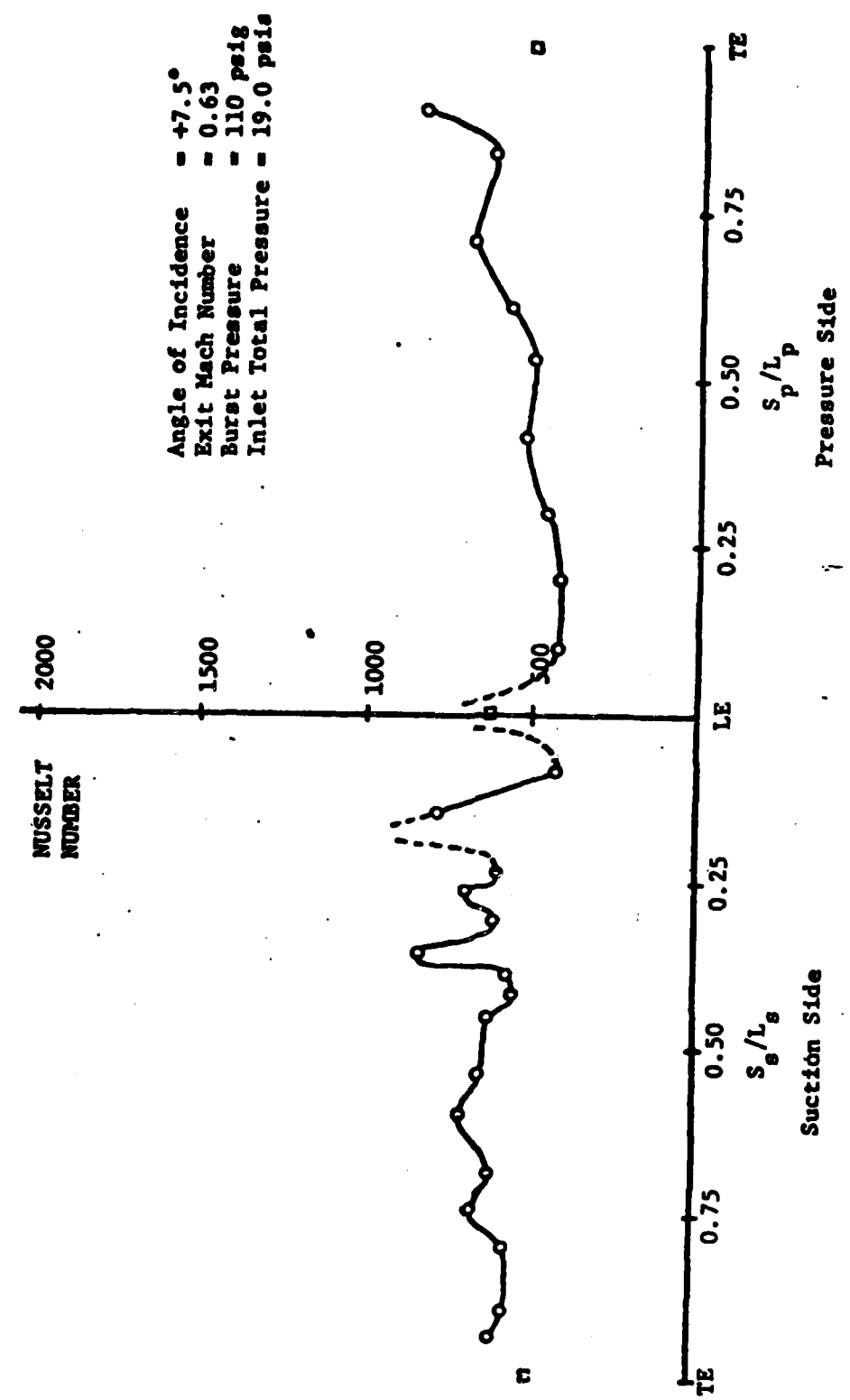


FIGURE 8a LOCAL NUSSELT NUMBER VS BLADE SURFACE LOCATION

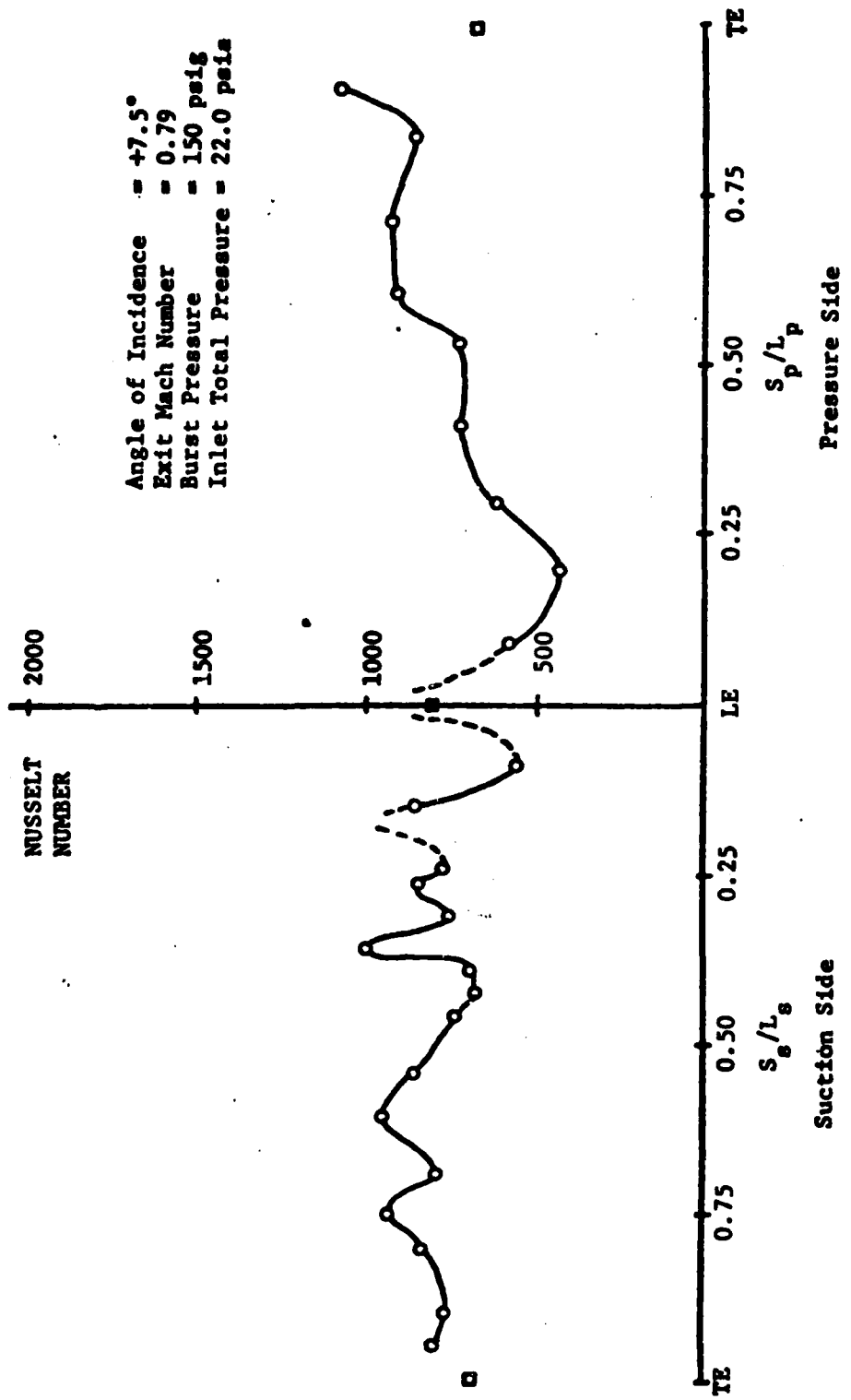


FIGURE 3a LOCAL NUSSELT NUMBER VS BLADE SURFACE LOCATION

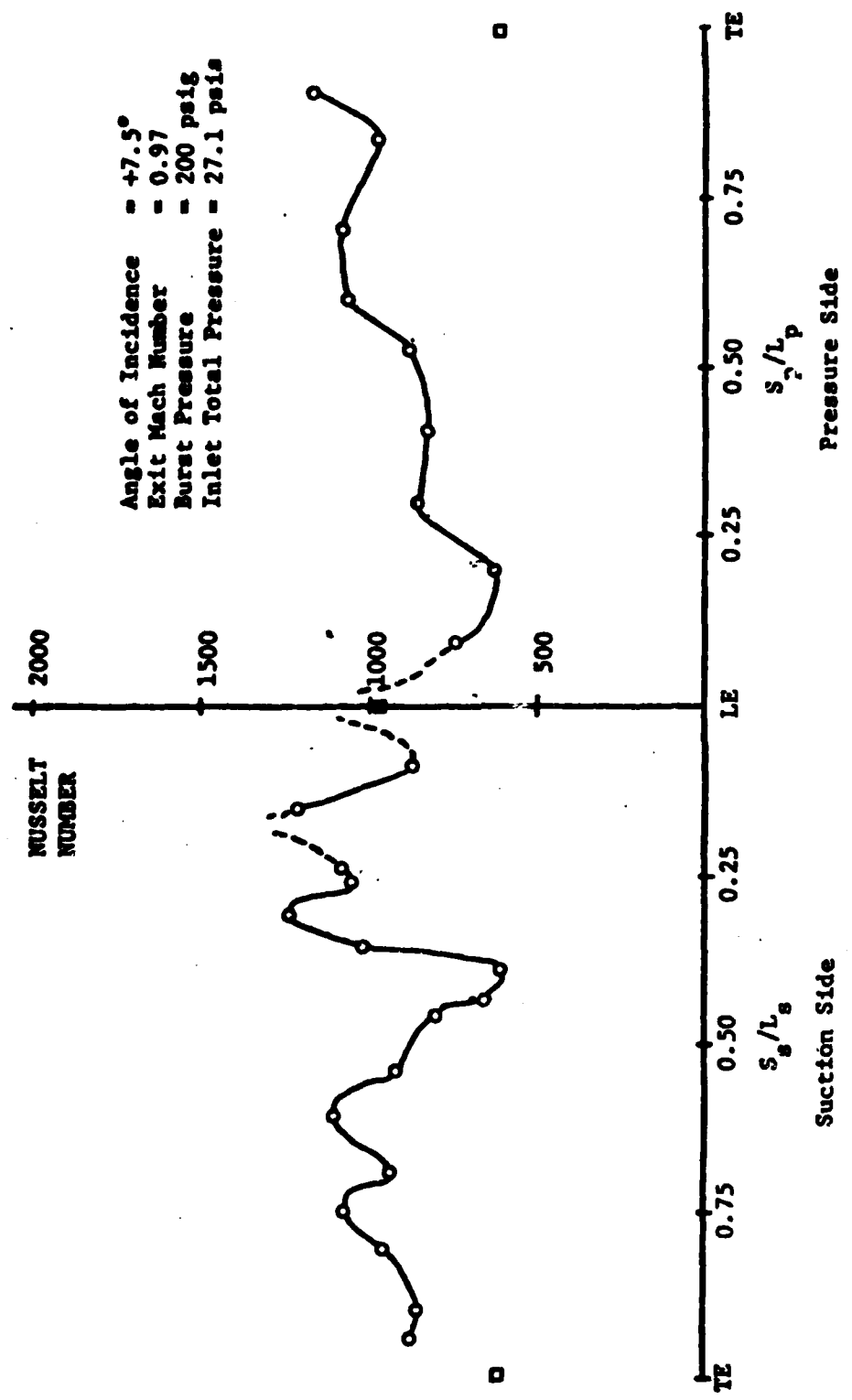


FIGURE 8C. LOCAL NUSSELT NUMBER VS BLADE SURFACE LOCATION

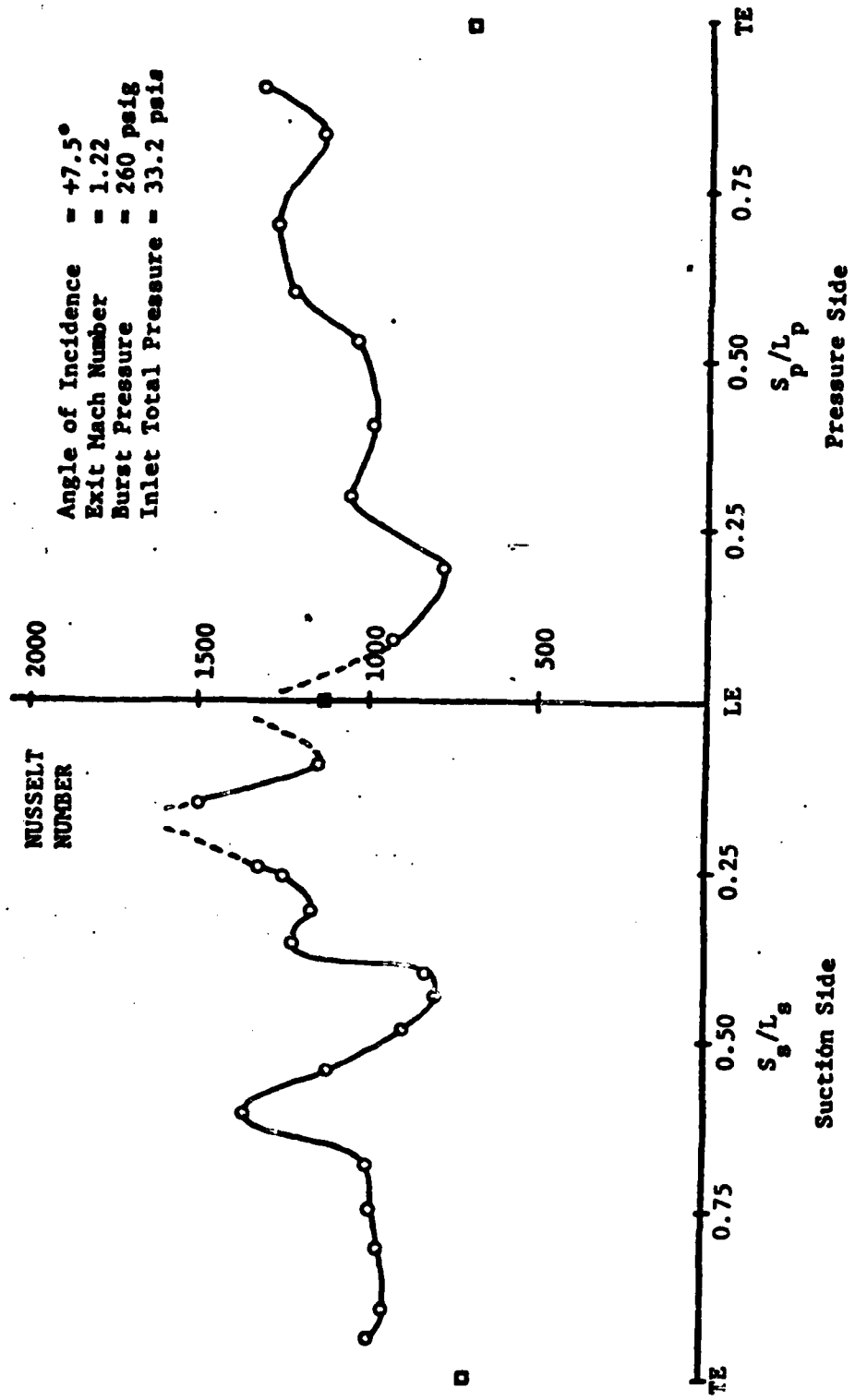


FIGURE 38D: LOCAL NUSSELT NUMBER VS BLADE SURFACE LOCATION

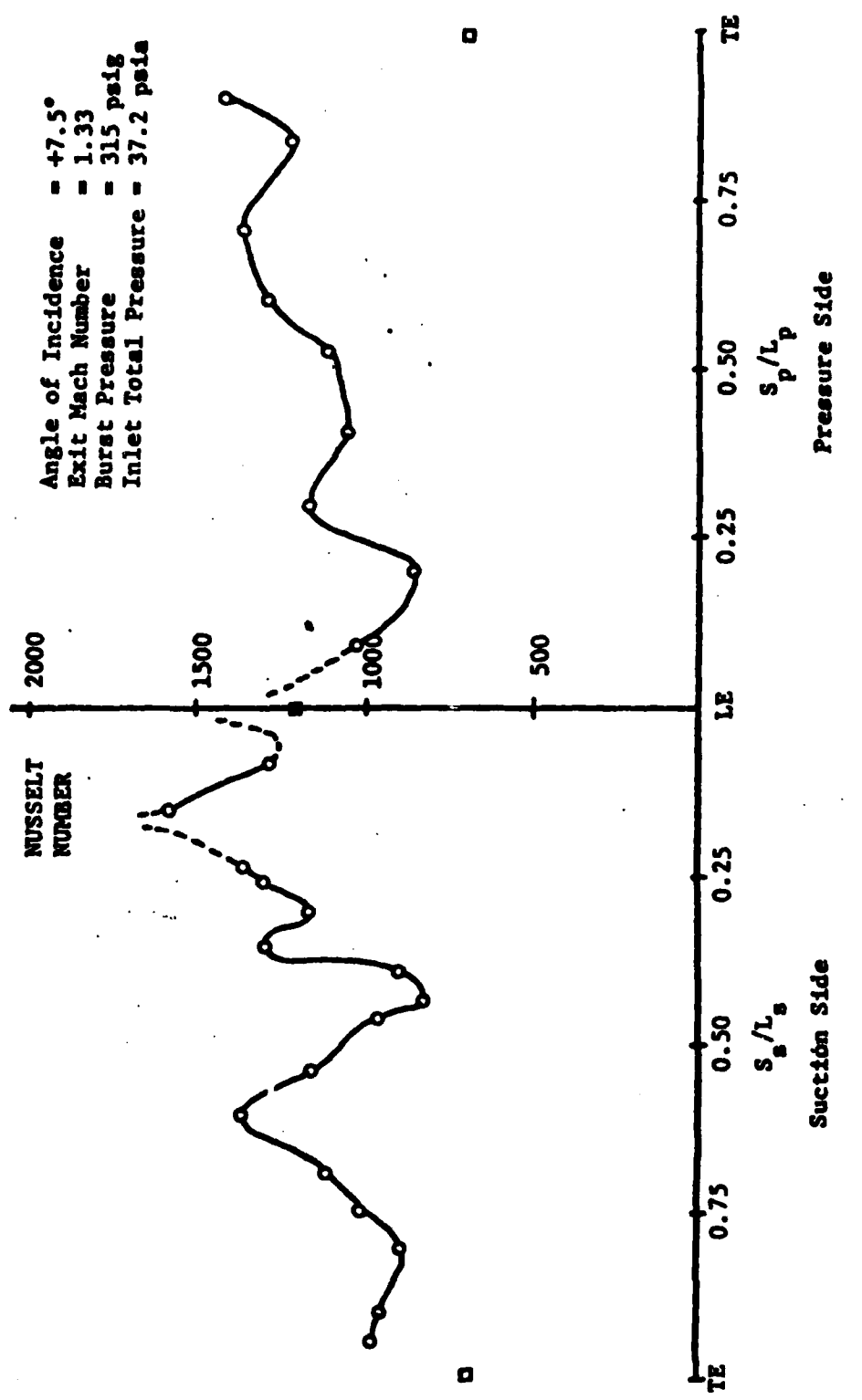


FIGURE 5 LOCAL NUSSELT NUMBER VS BLADE SURFACE LOCATION

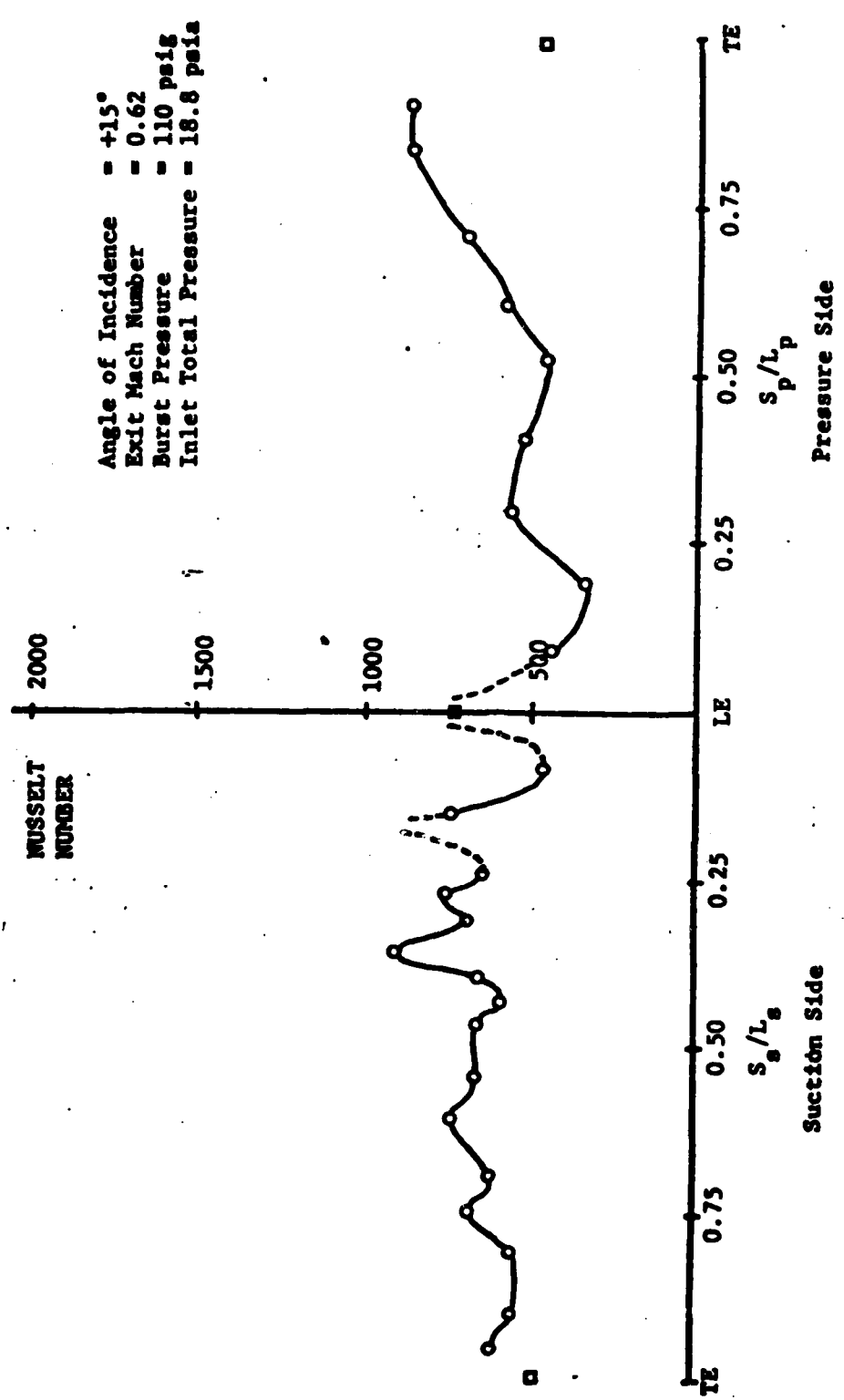


FIGURE 9A LOCAL NUSSELT NUMBER VS BLADE SURFACE LOCATION

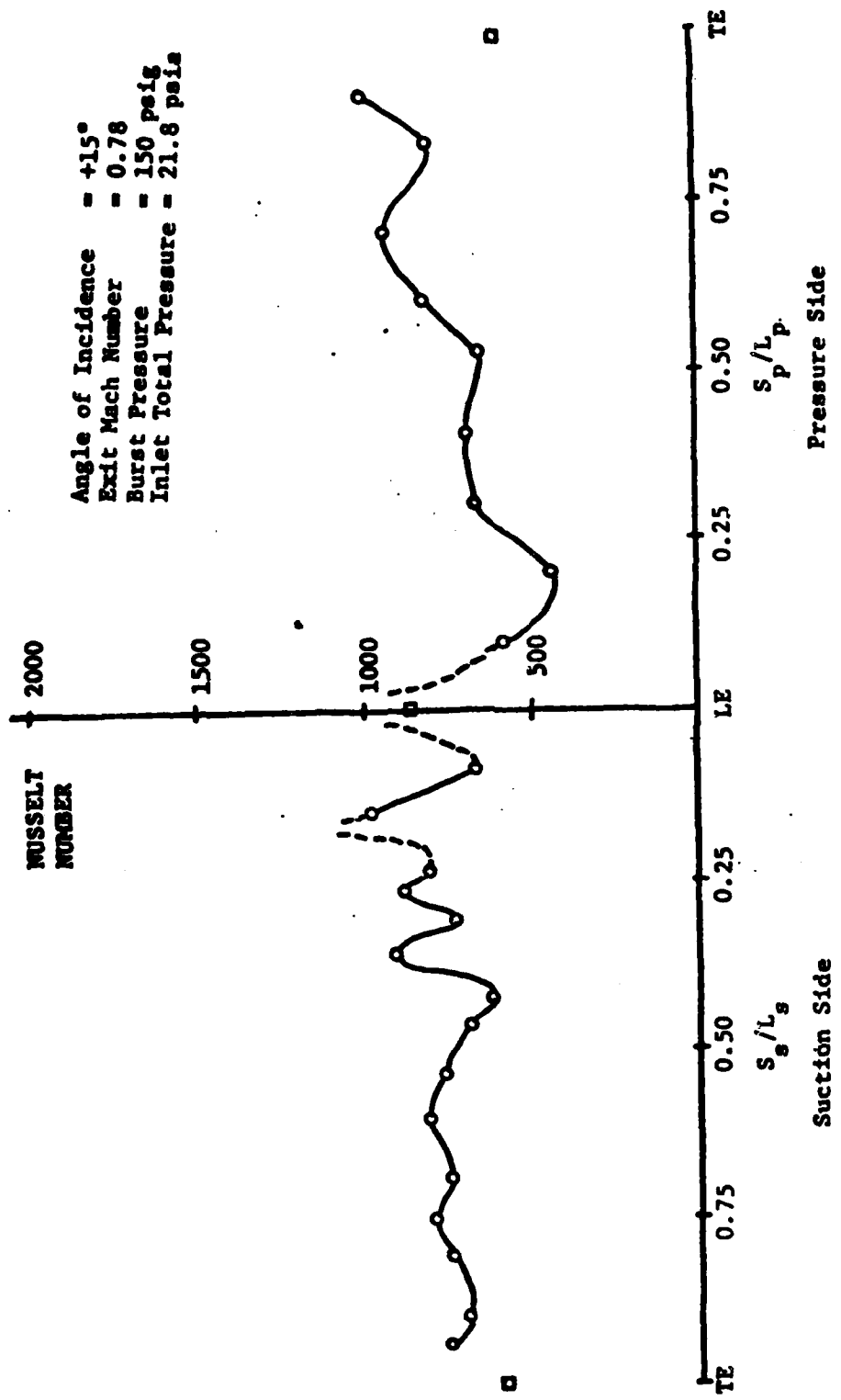


FIGURE 55. LOCAL NUSSELT NUMBER VS BLADE SURFACE LOCATION

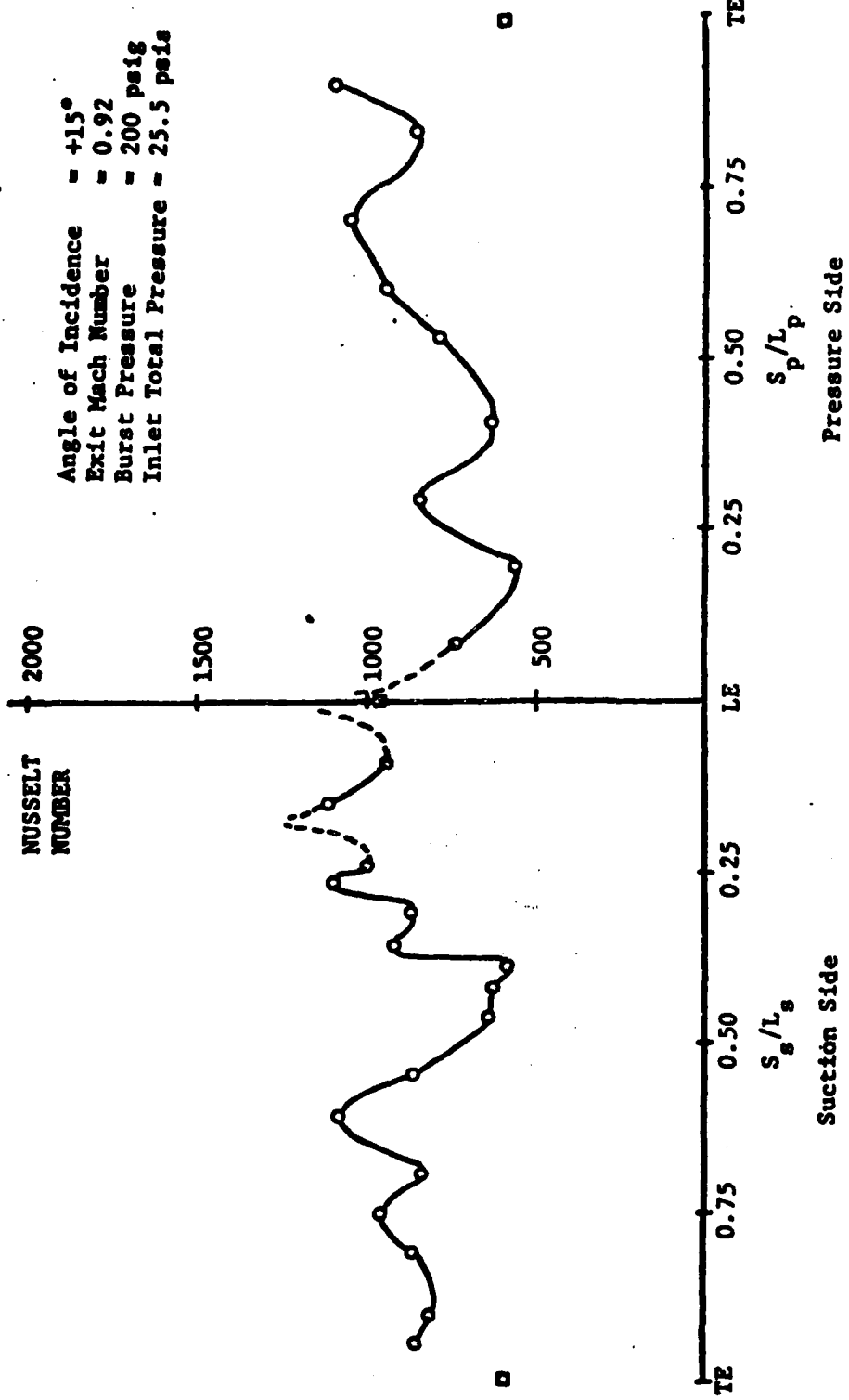


FIGURE 2-9a LOCAL NUSSELT NUMBER VS BLADE SURFACE LOCATION

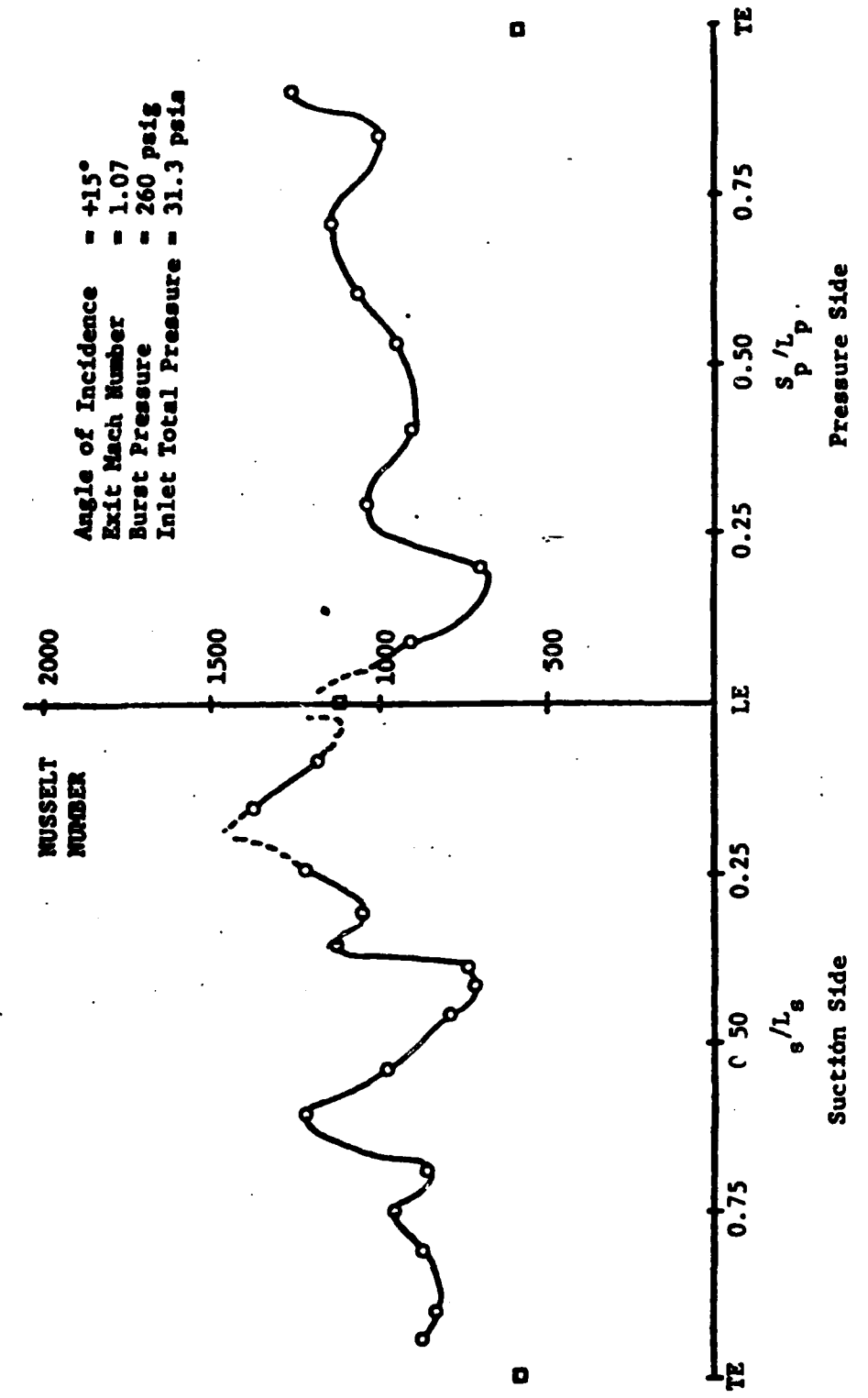


FIGURE 9D LOCAL NUSSELT NUMBER VS BLADE SURFACE LOCATION

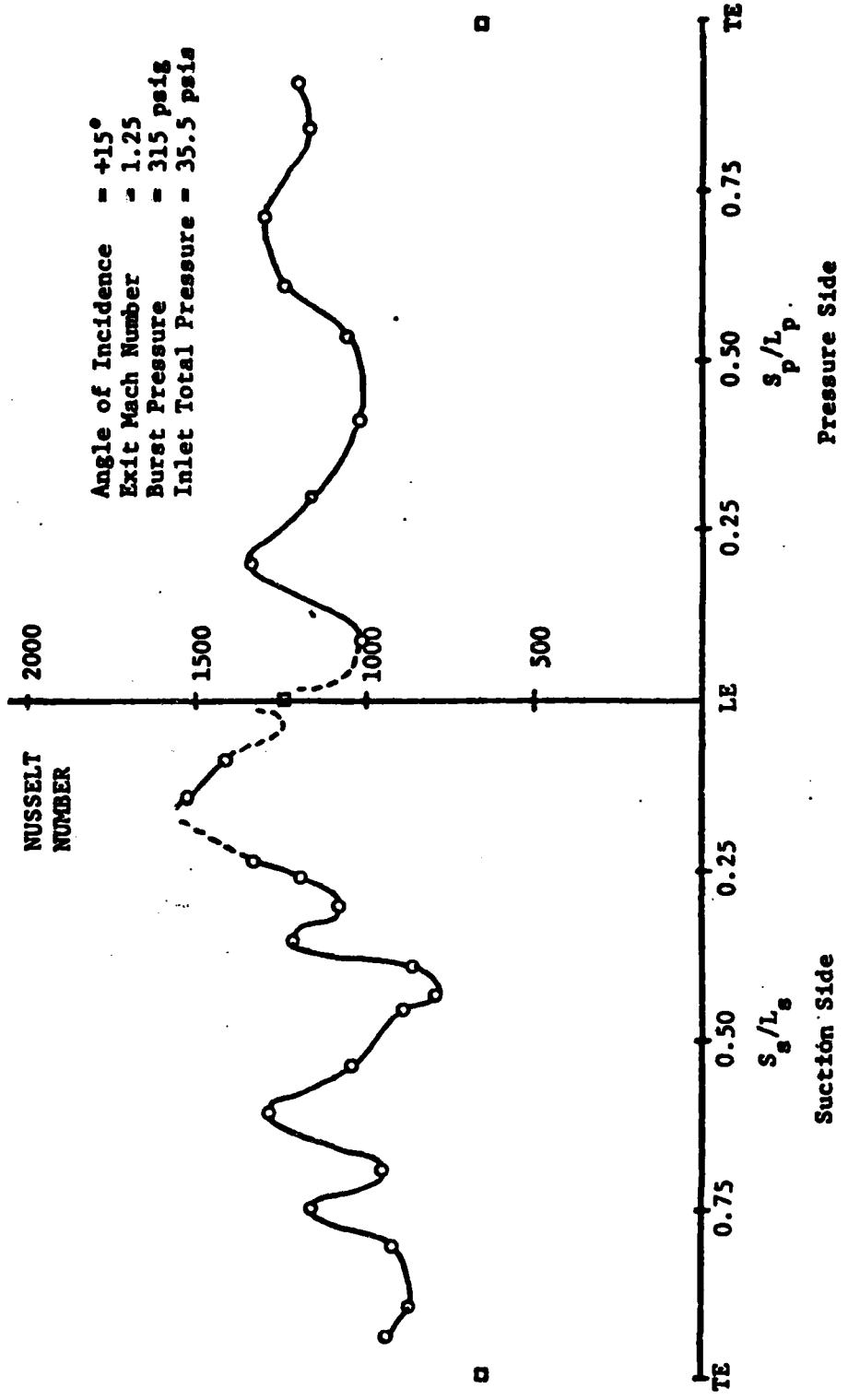


FIGURE 2 LOCAL NUSSLET NUMBER VS BLADE SURFACE LOCATION

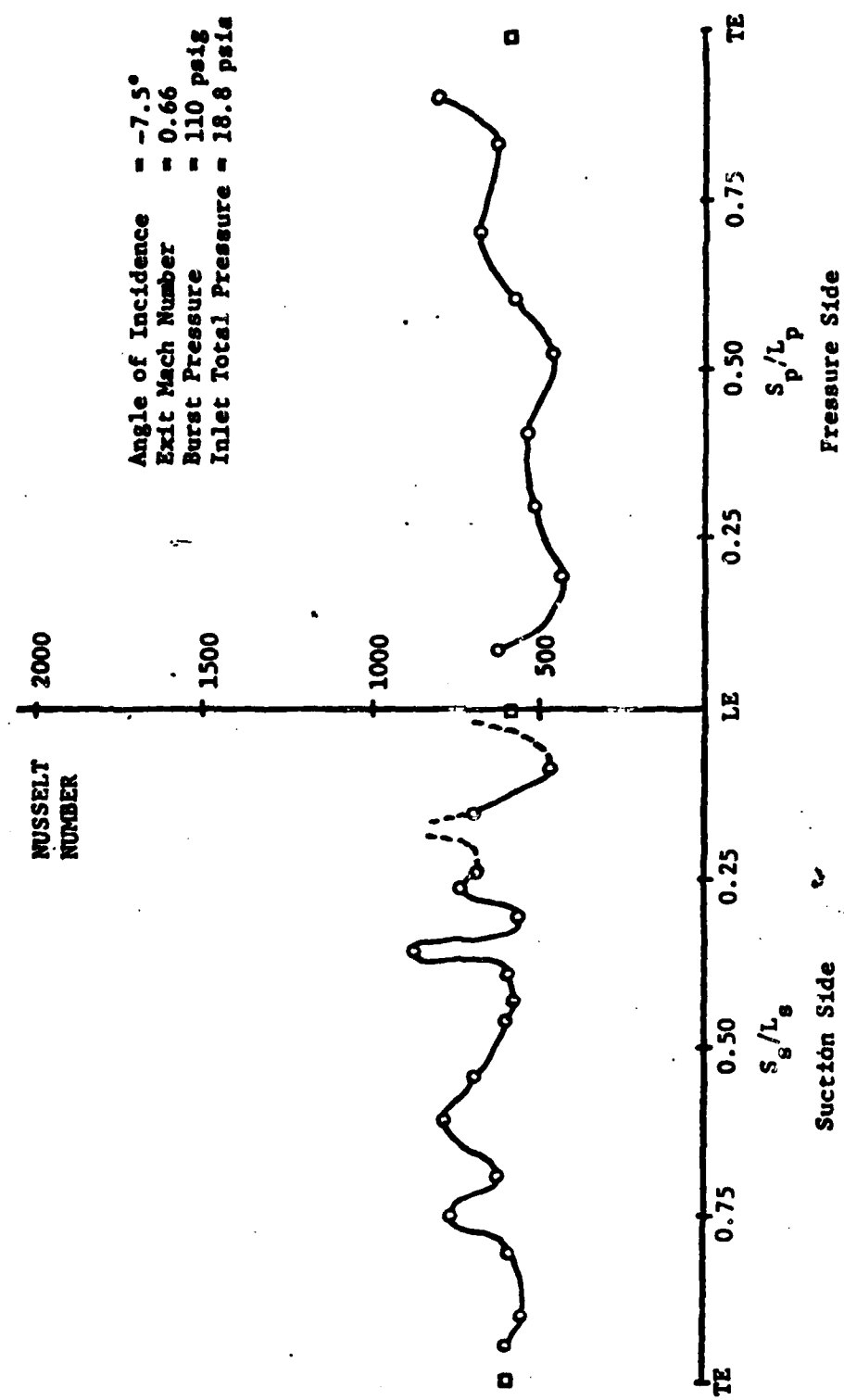


FIGURE 10A LOCAL NUSSELT NUMBER VS BLADE SURFACE LOCATION

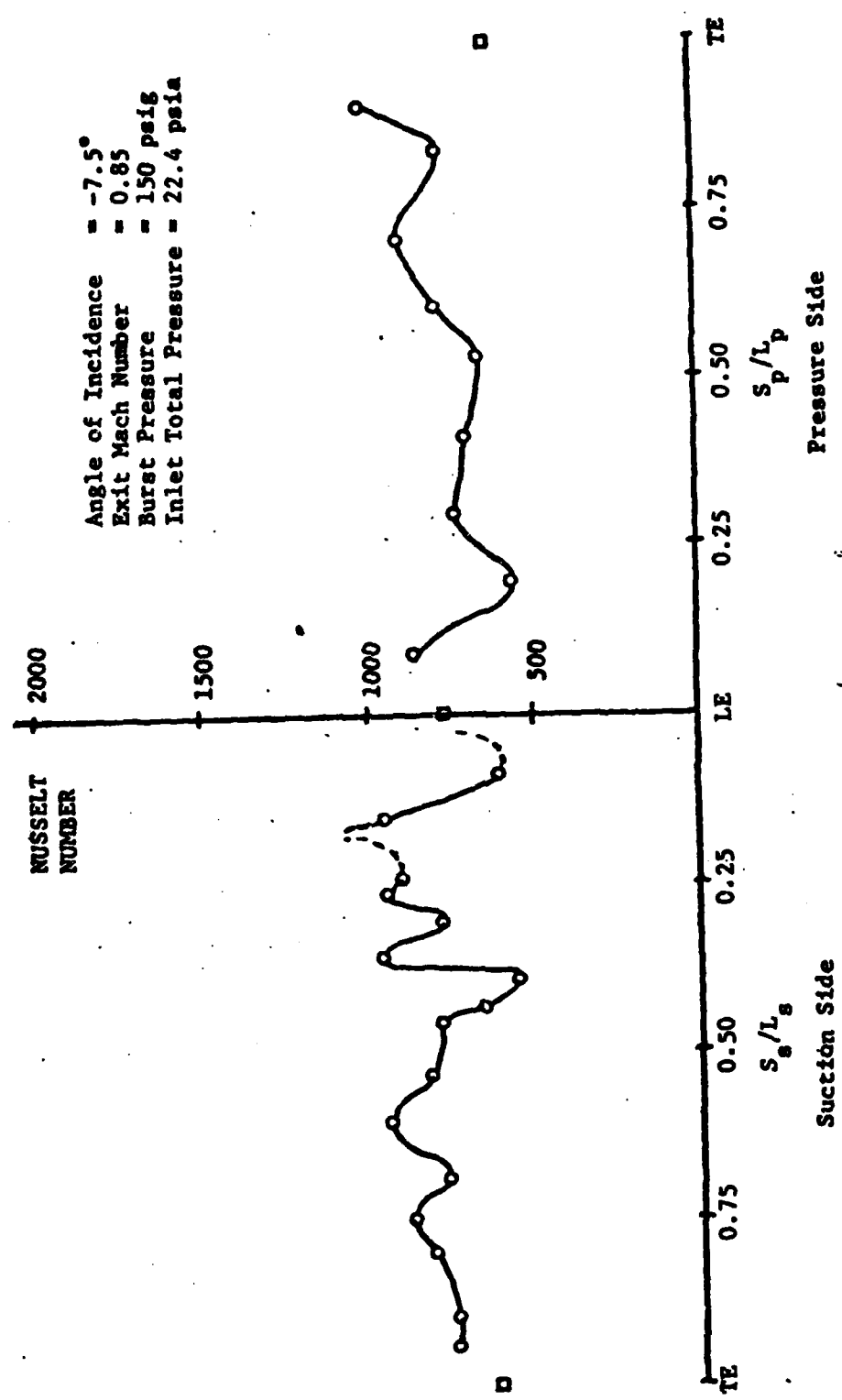


FIGURE 10B LOCAL NUSSELT NUMBER VS BLADE SURFACE LOCATION

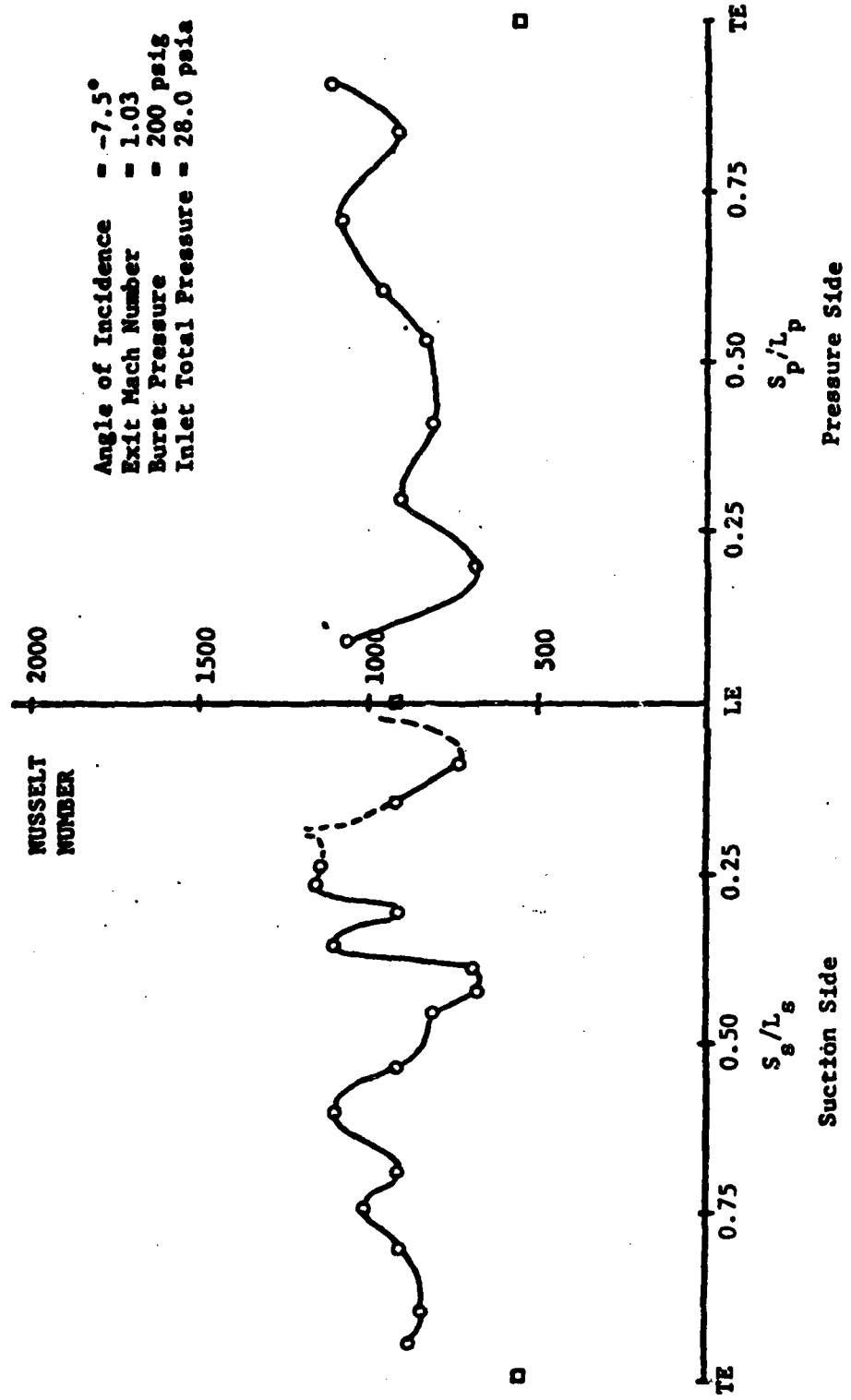


FIGURE 110c LOCAL NUSSELT NUMBER VS ELADE SURFACE LOCATION

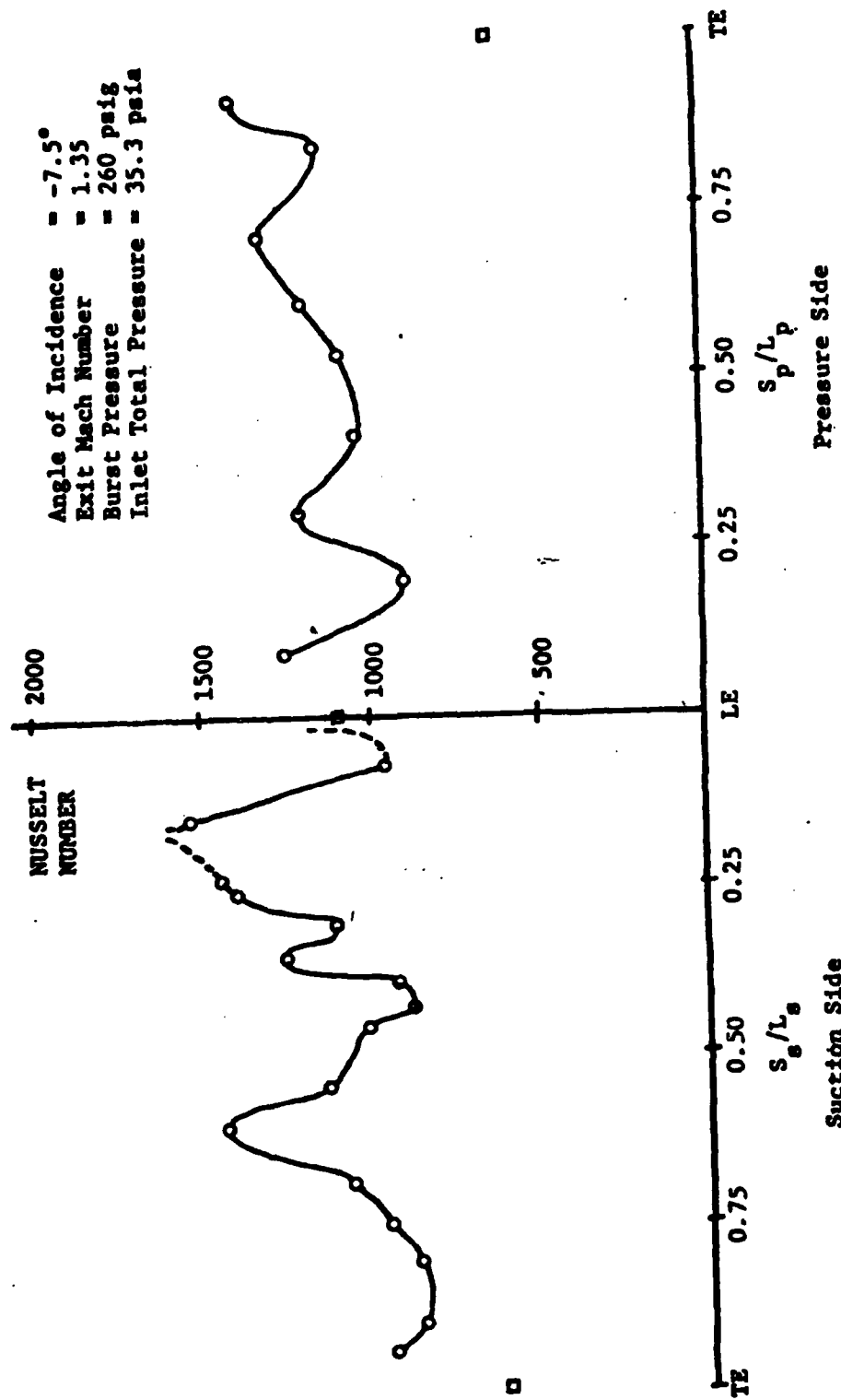


FIGURE 10D LOCAL NUSSELT NUMBER VS BLADE SURFACE LOCATION

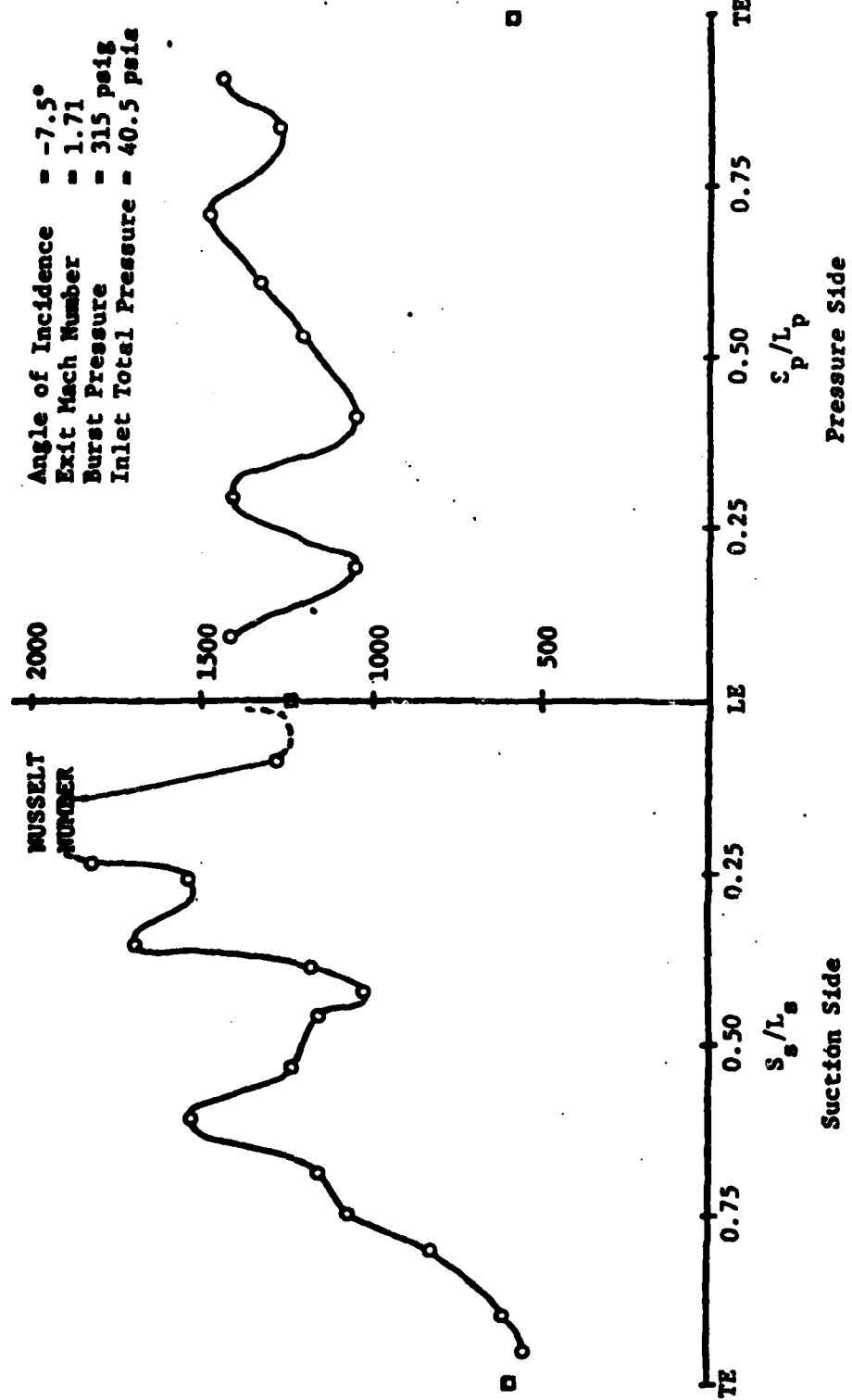


FIGURE 10E LOCAL NUSSELT NUMBER VS BLADE SURFACE LOCATION

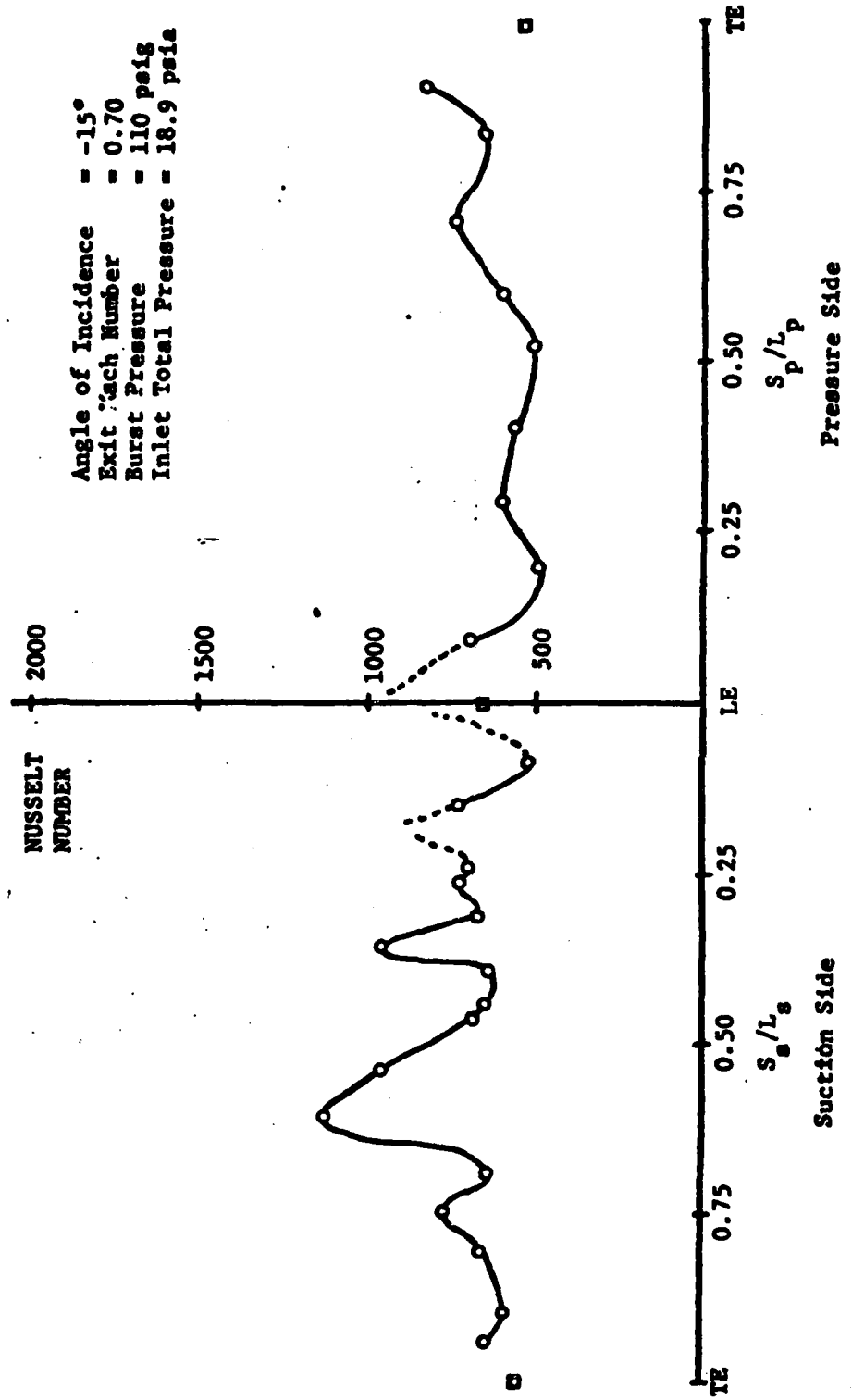


FIGURE 11a LOCAL NUSSELT NUMBER VS BLADE SURFACE LOCATION

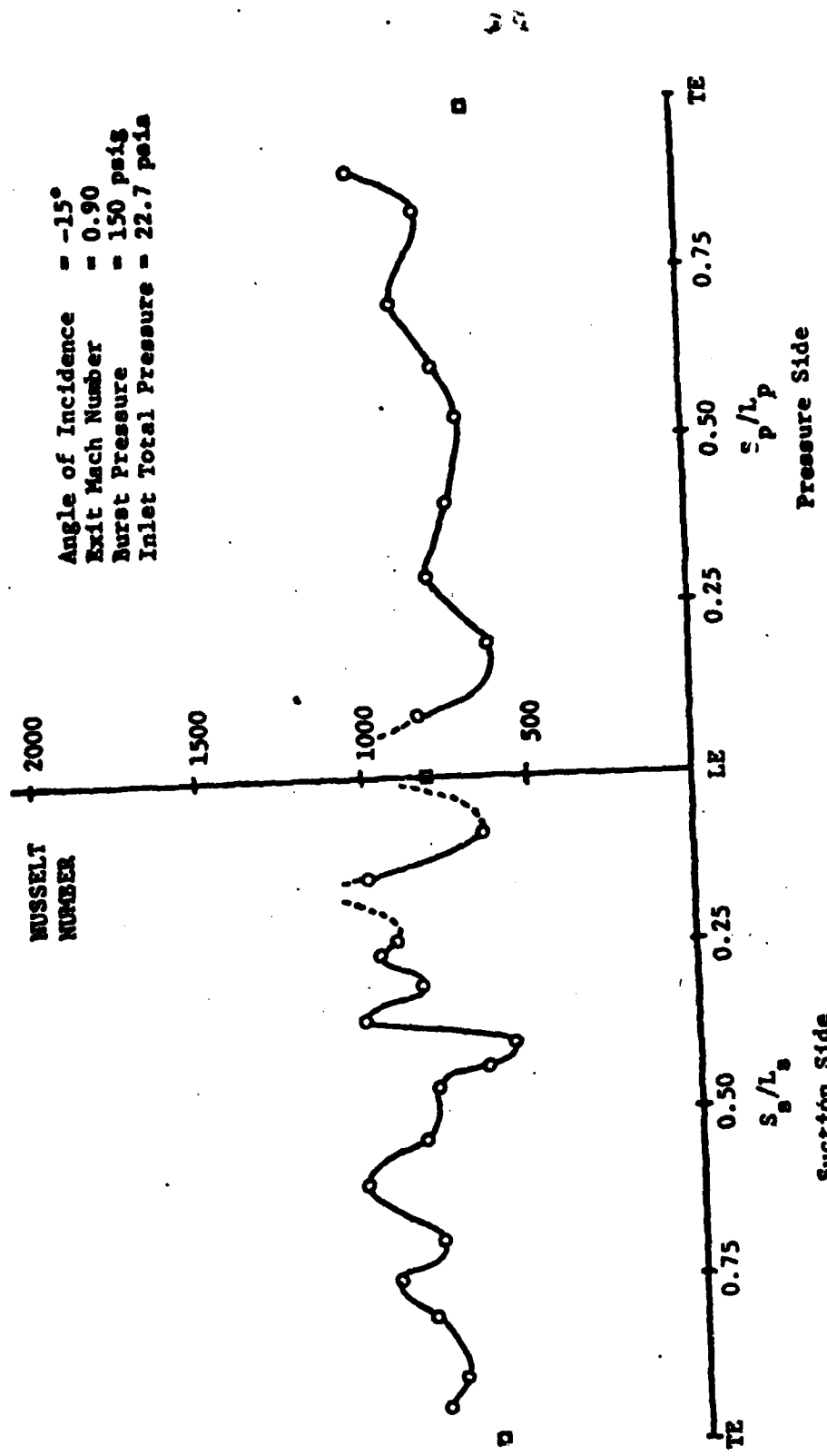


FIGURE 11F LOCAL NUSSELT NUMBER VS BLADE SURFACE LOCATION

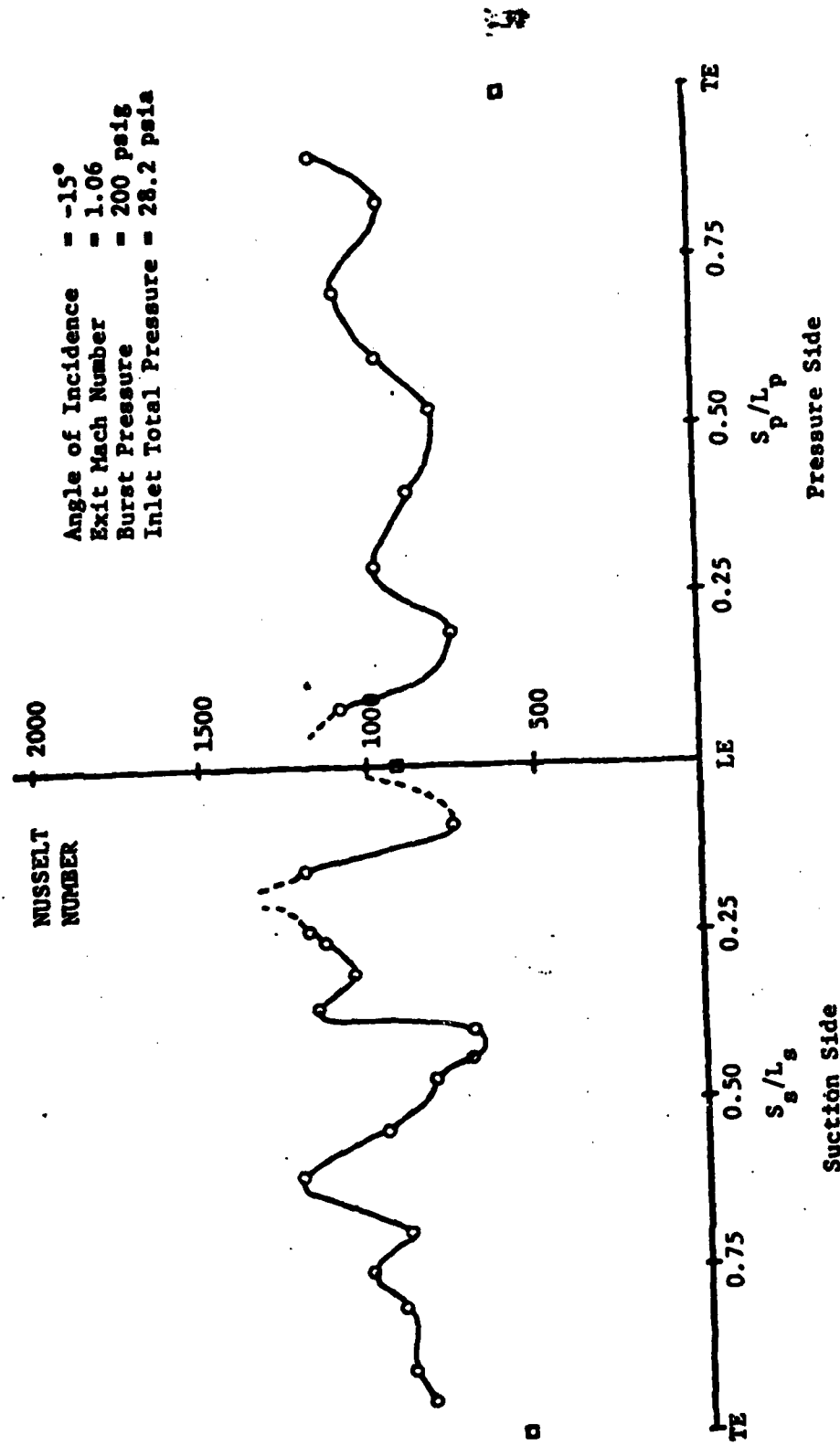


FIGURE 2-11c LOCAL NUSSELT NUMBER VS BLADE SURFACE LOCATION

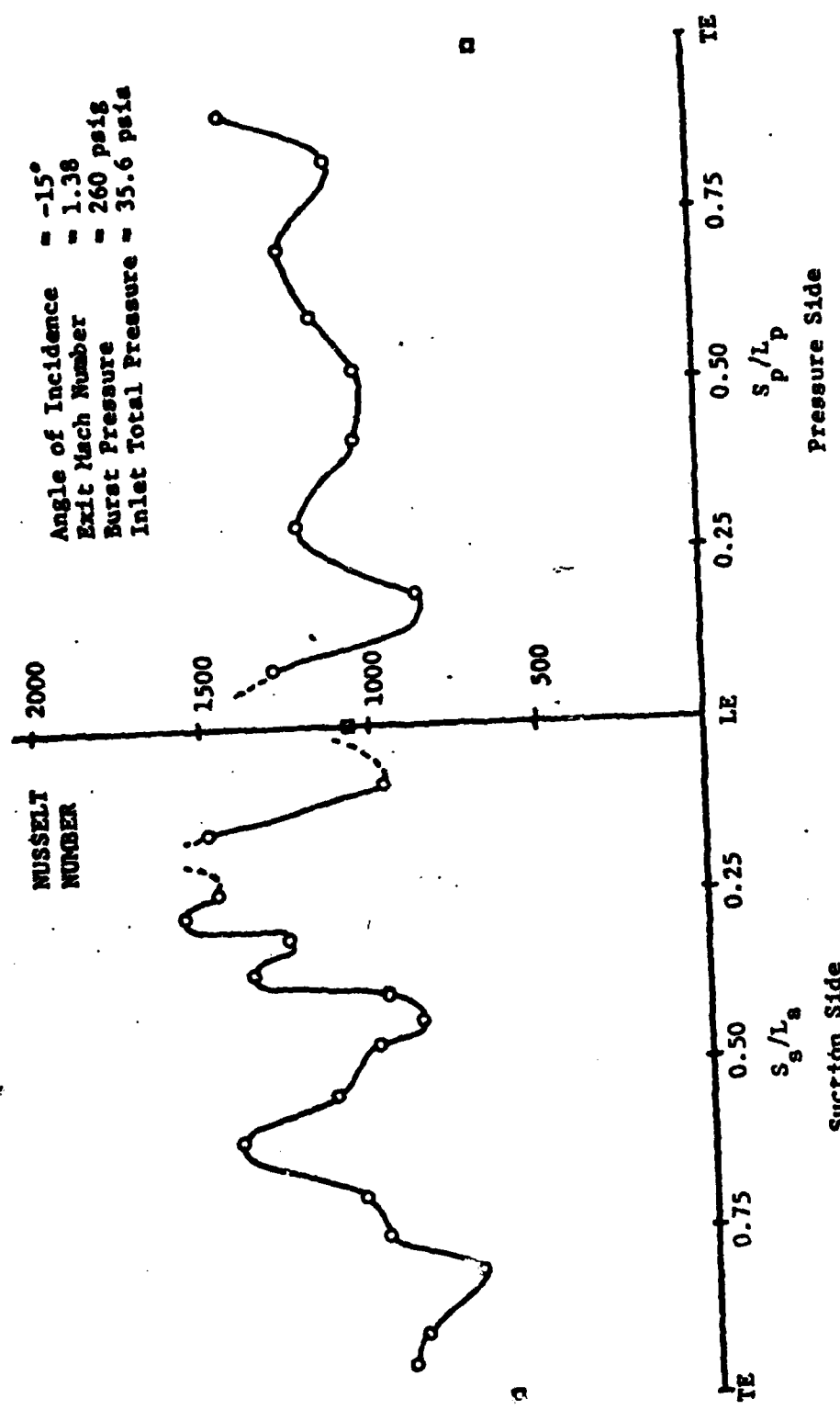


FIGURE 11b LOCAL NUSSELT NUMBER VS BLADE SURFACE LOCATION

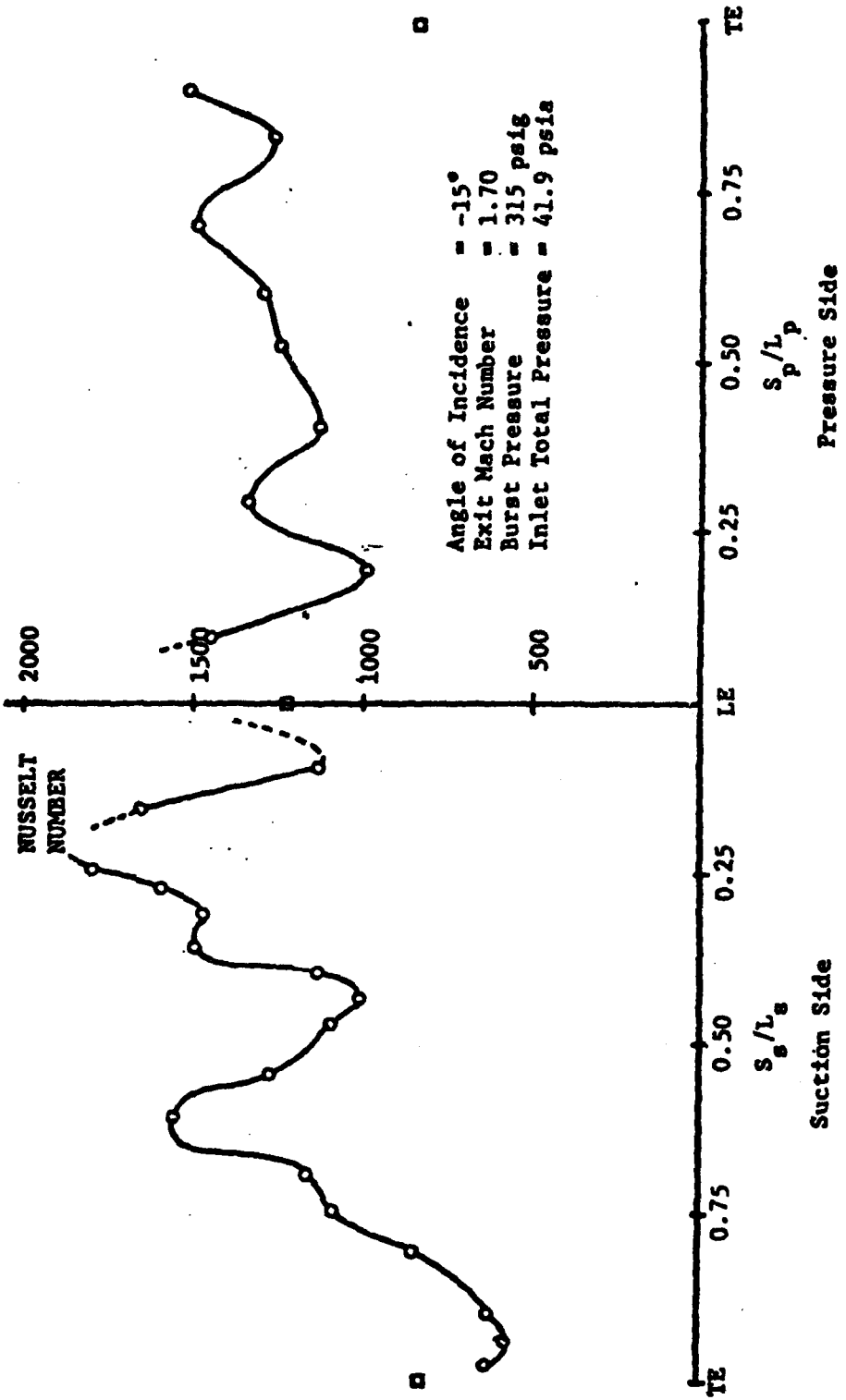


FIGURE 11E LOCAL NUSSELT NUMBER VS BLADE SURFACE LOCATION

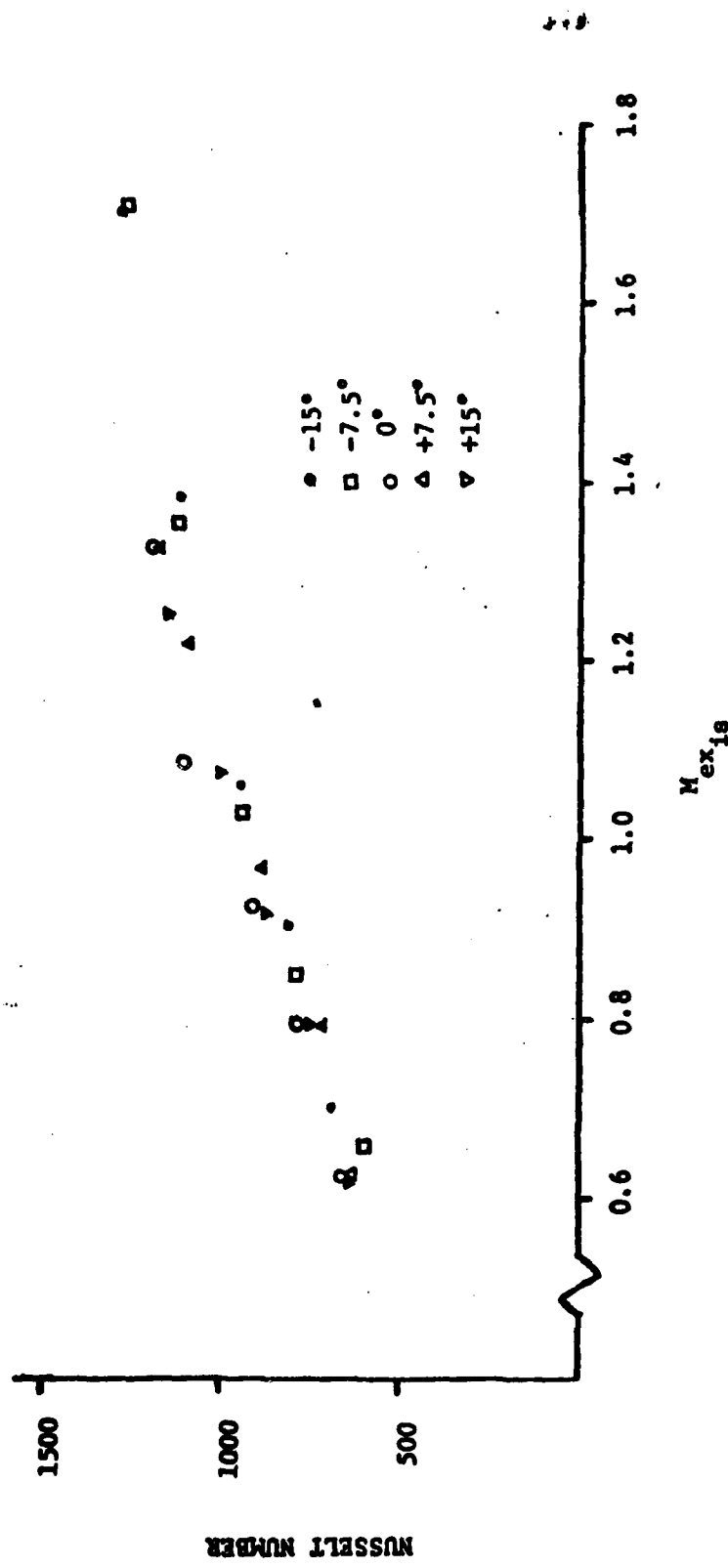


FIGURE 12: AVERAGE BLADE NUSSELT NUMBER VS EXIT MACH NUMBER FOR DIFFERENT INCIDENCES

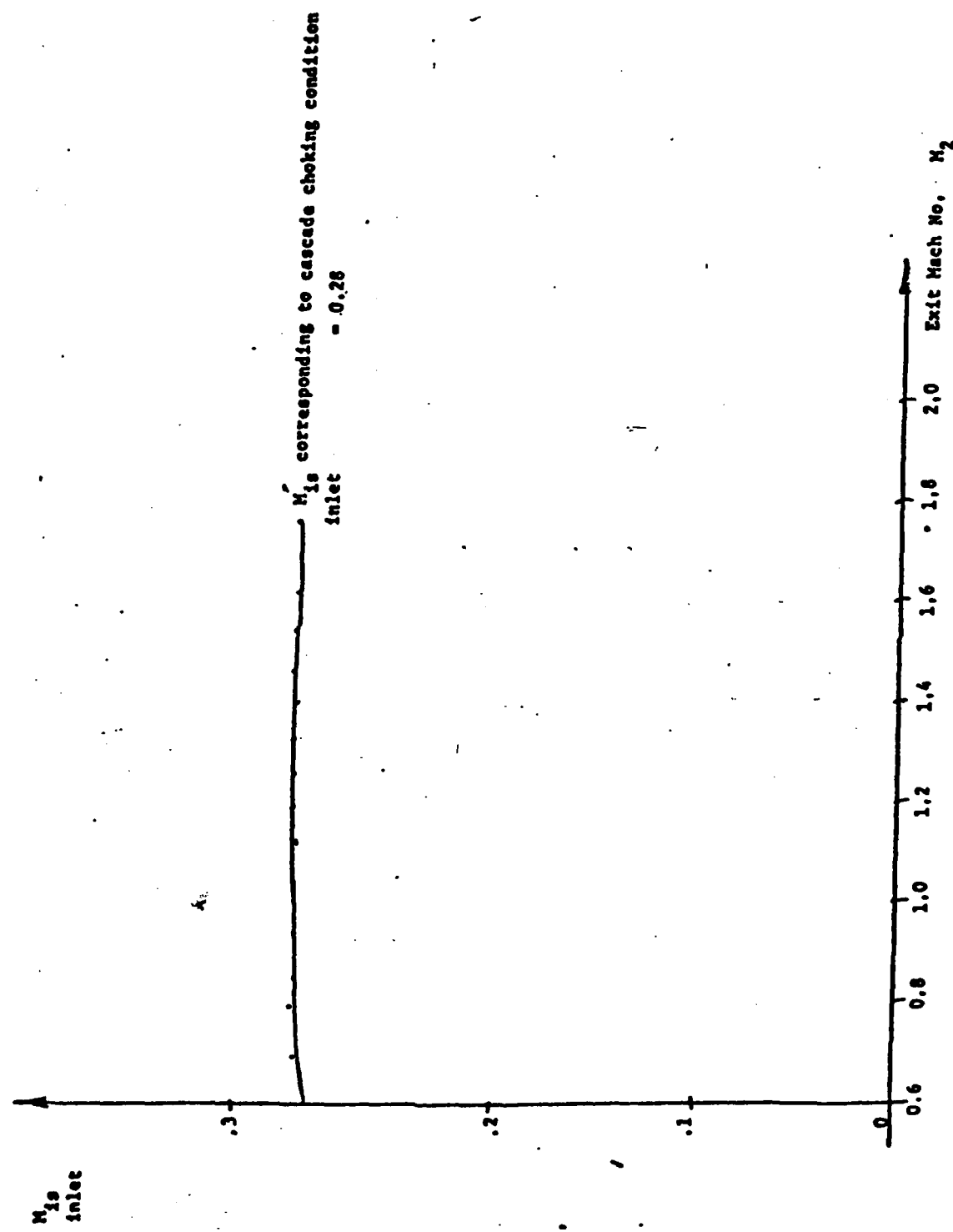


Figure 13 Inlet Mach Number versus Exit Mach Number

BLADE VELOCITY DISTRIBUTION
TRANSONIC BLADE WITH STRAIGHT SUCTION BACK

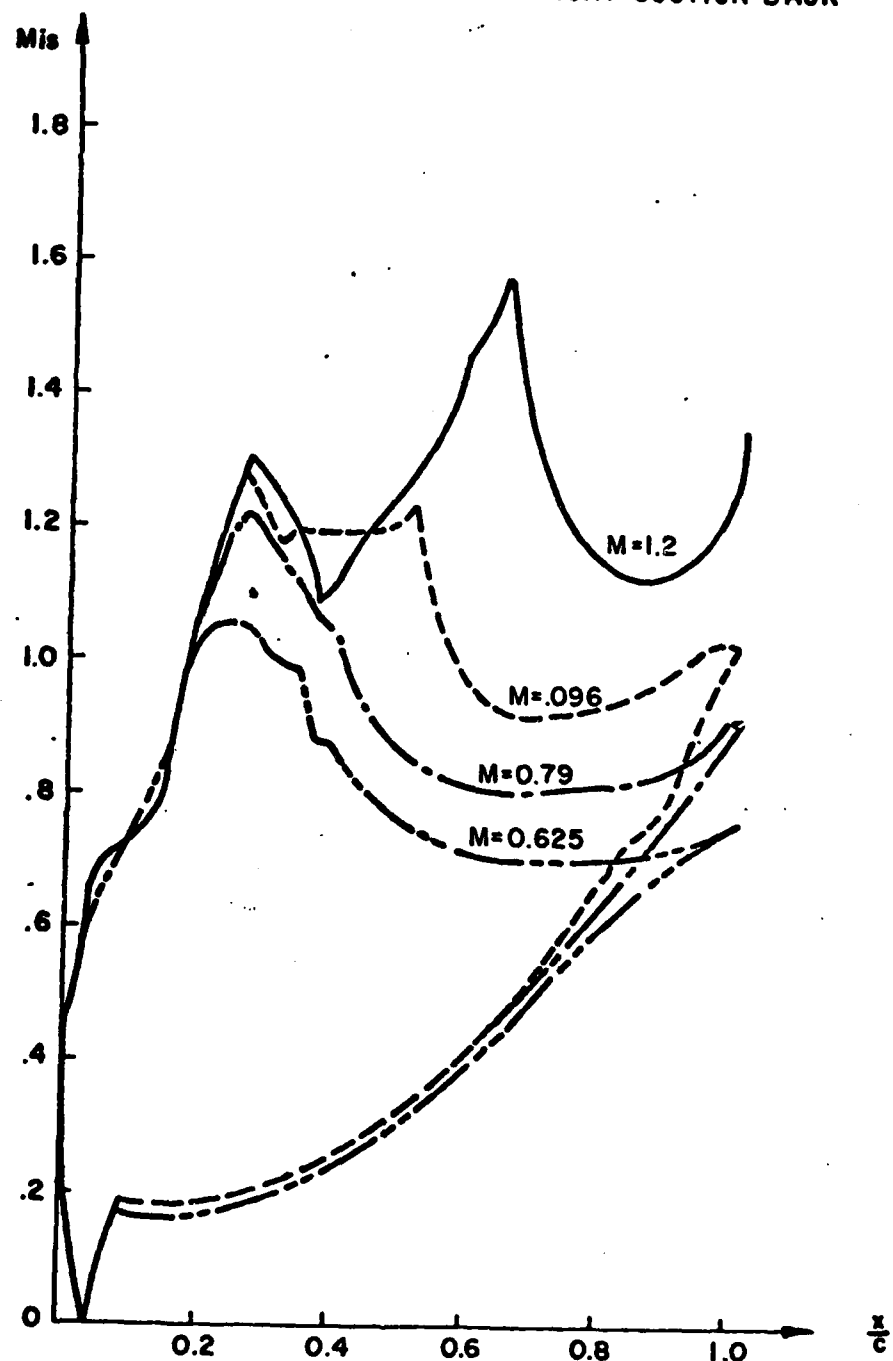
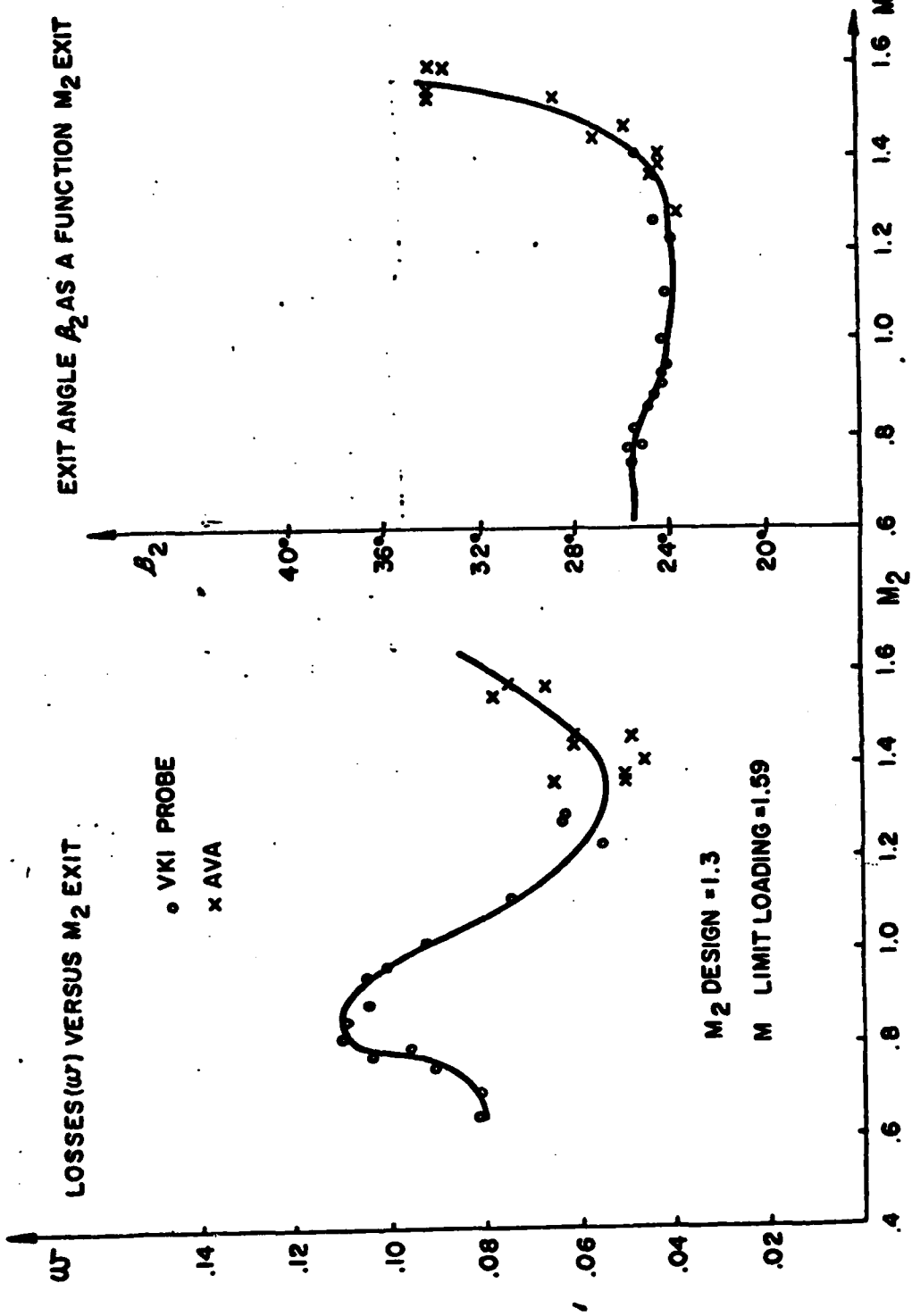


Figure 14 Blade 1 Surface Mach Number Distribution $g/c = 0.75$

Figure -15.

PERFORMANCE CURVE BLADE WITH STRAIGHT SUCTION BACK



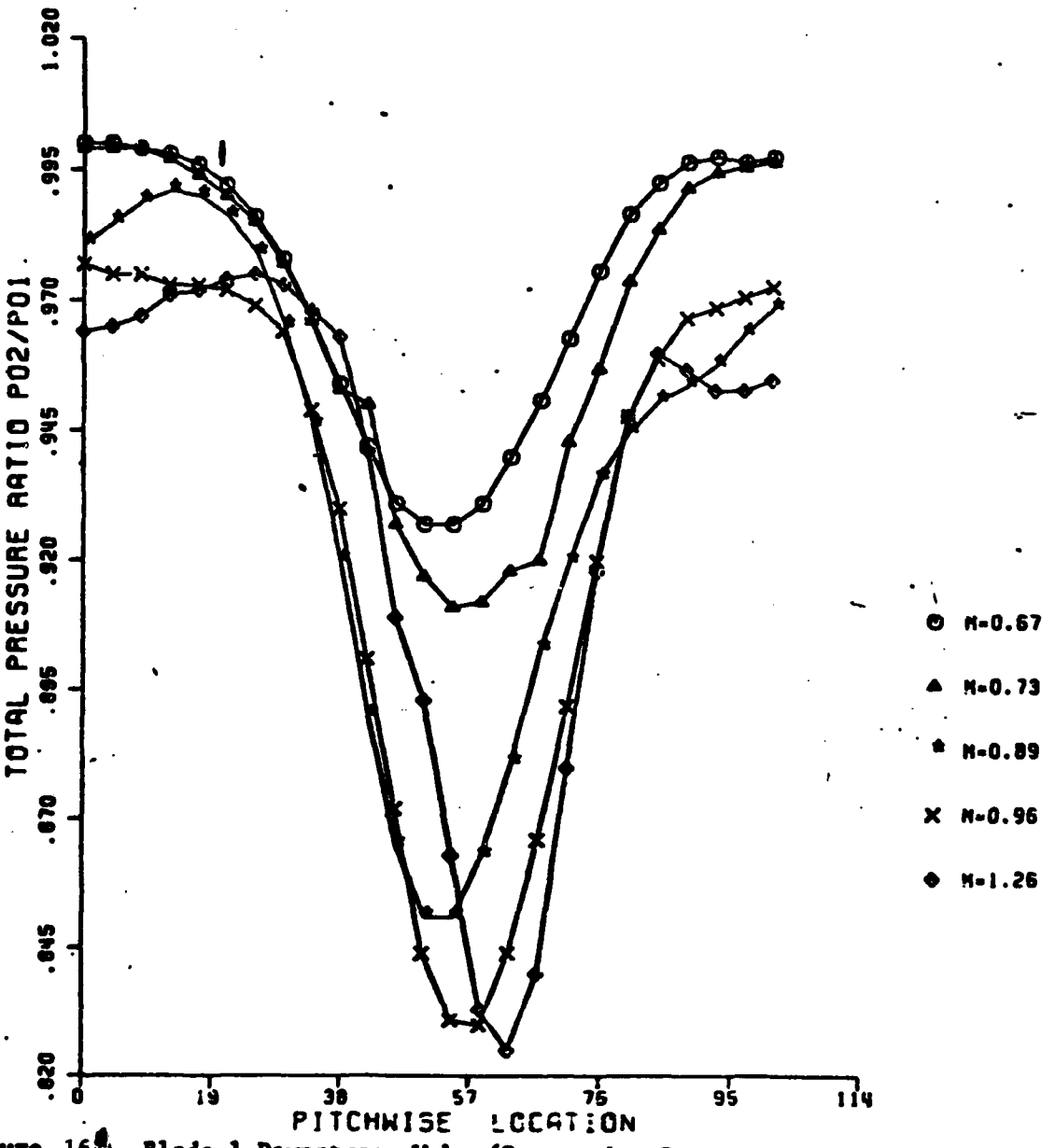
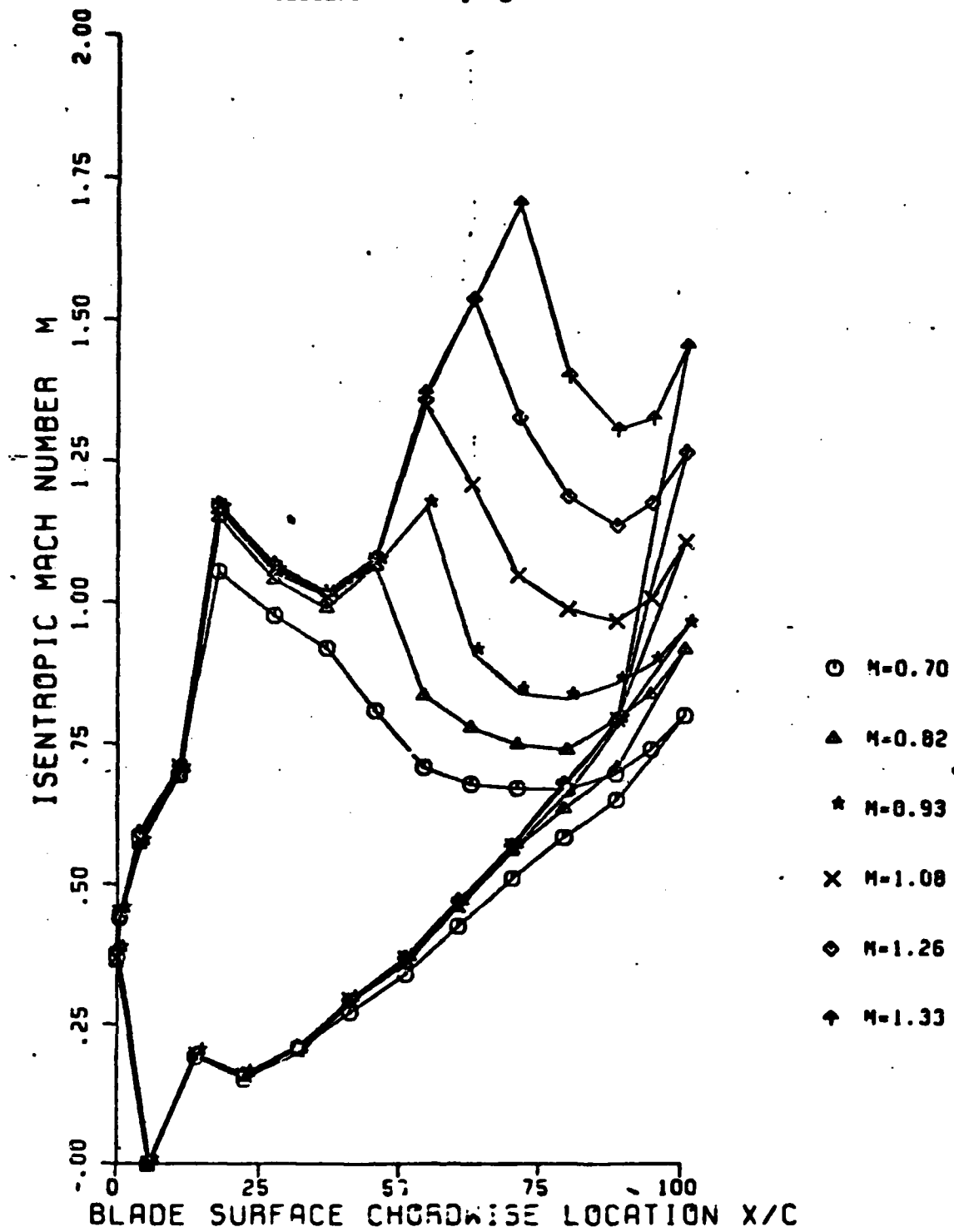


Figure 16. Blade 1 Downstream Wake (Stagnation Pressure ratio
variation across the pitch)

Figure 17 Blade 1 Mach number distribution tested in Hot Blowdown
Cascade Facility $g/c = 0.695$.



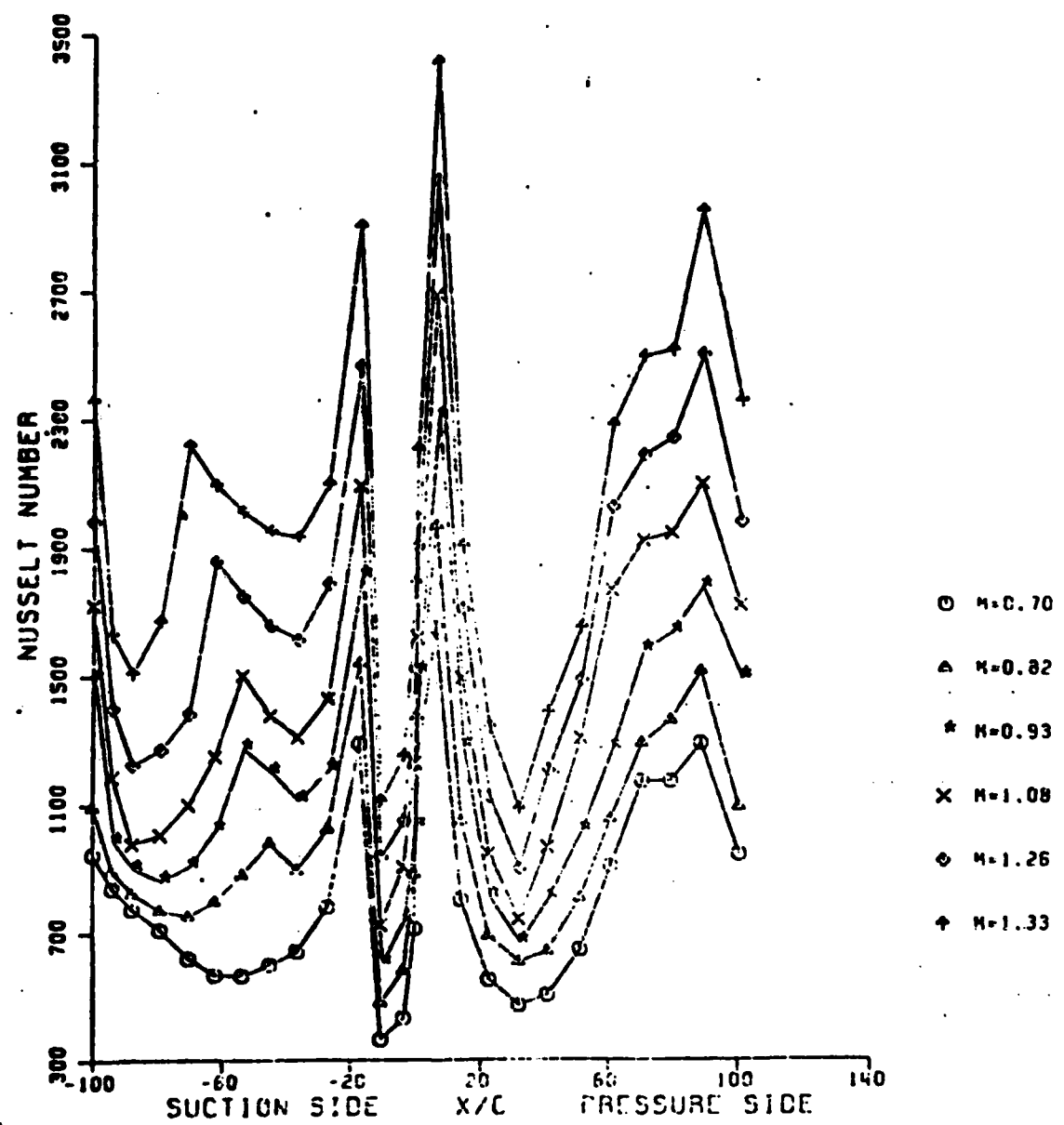


Figure 18 Blade 1 Nusselt number variation over the blade surface
for different exit Mach numbers.

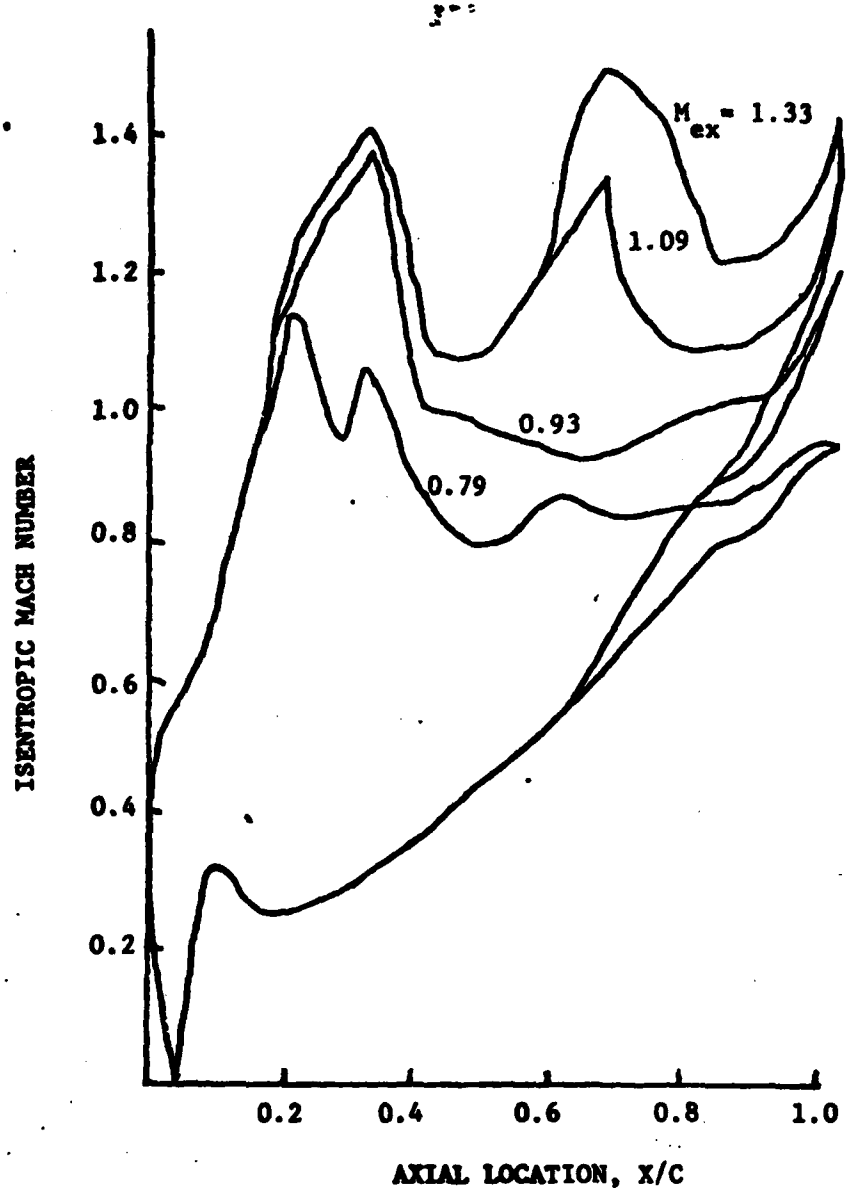
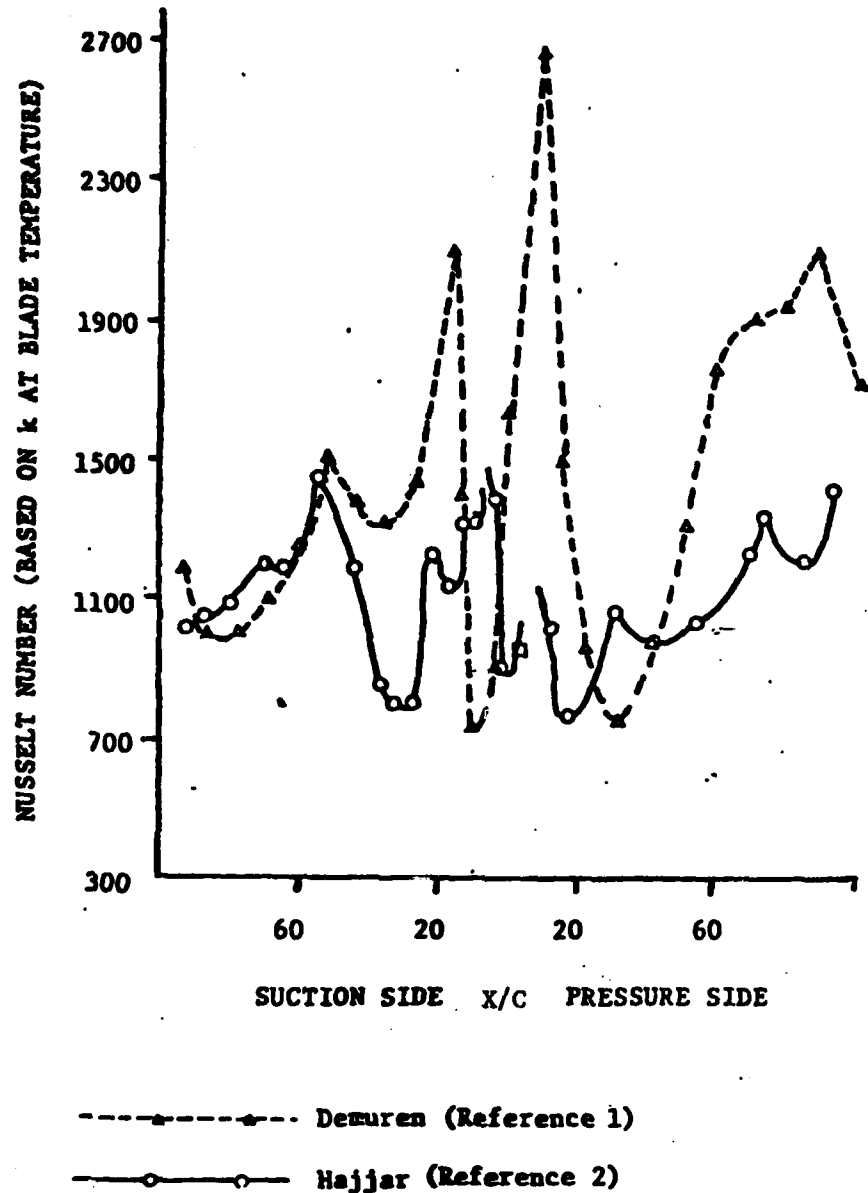


FIGURE 49. HAJJAR MACH NUMBER DISTRIBUTION FOR ZERO INCIDENCE, TAKEN AT M.I.T. BLOWDOWN FACILITY



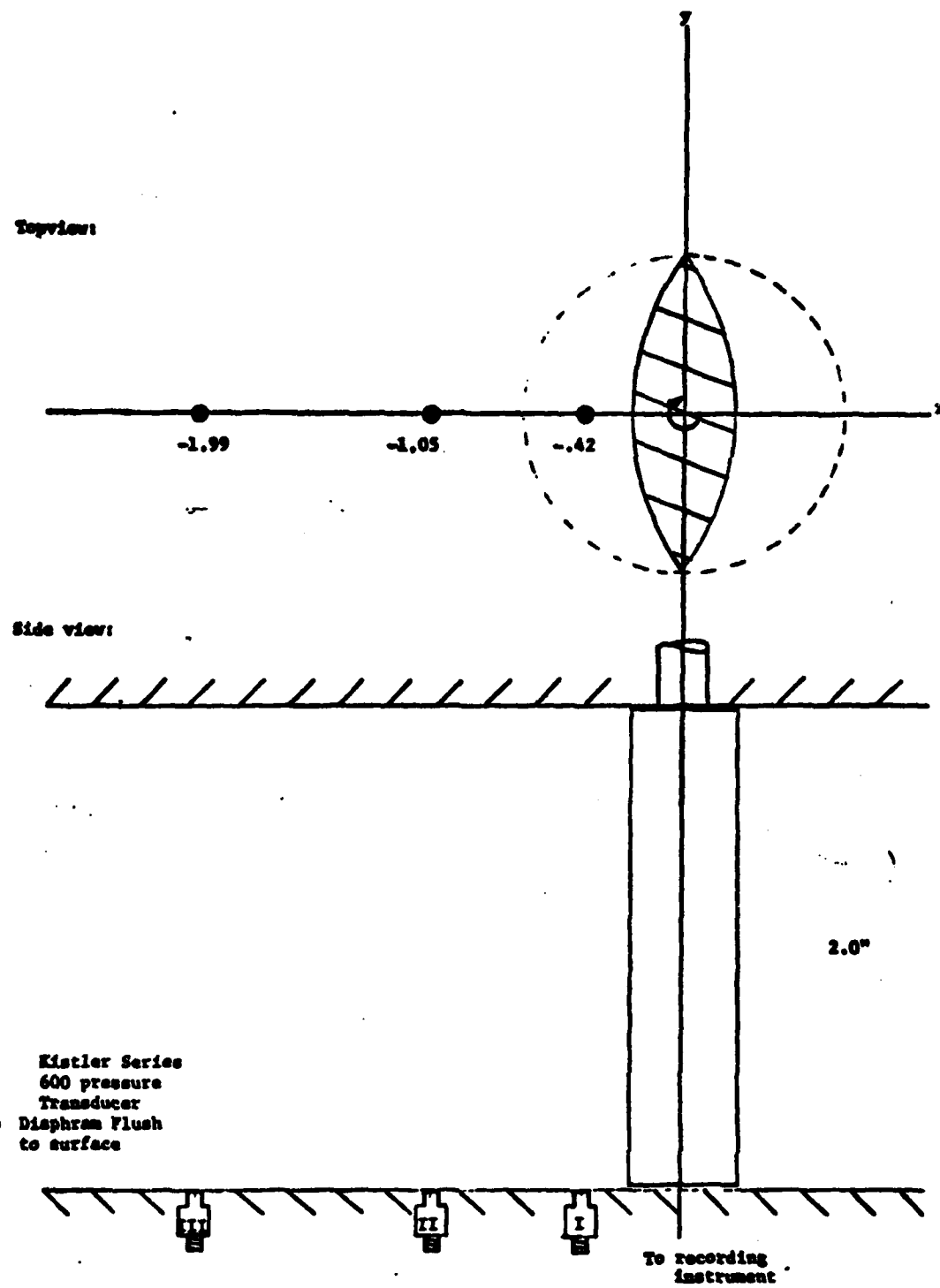


Figure 21 Rotating Ellipse Experimental Setup

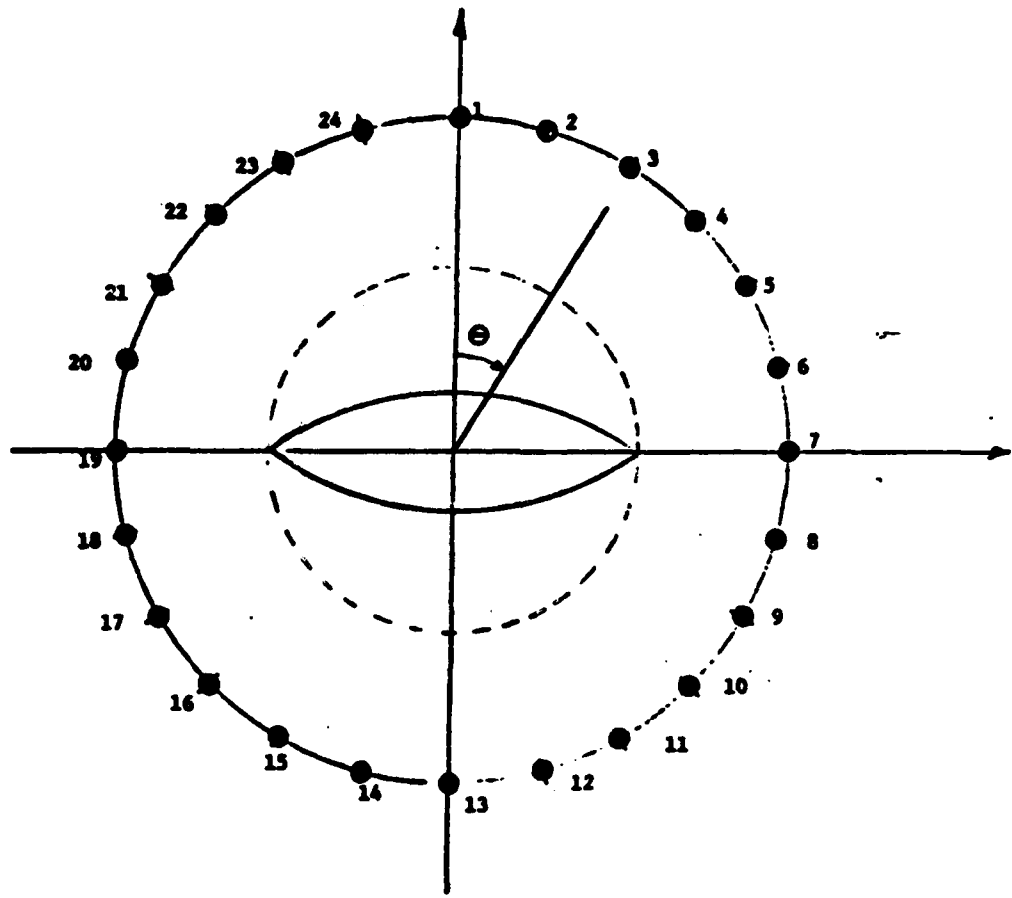


Figure 22 Relative Pressure Transducer Locations

TABLE 2 Summary of Confocal Ellipse Calculations

Transducer Location	Cartesian Coordinates		Elliptical Coordinates	
	X (inches)	Y (inches)	ξ	η (degrees)
1,1	0.0	0.632	0.923	90.0
1,2	0.164	0.610	0.911	79.02
1,3	0.316	0.547	0.875	67.87
1,4	0.447	0.447	0.811	56.17
1,5	0.547	0.316	0.711	43.38
1,6	0.610	0.164	0.557	28.0
1,7	0.632	0.0	0.348	0.0
2,1	0.0	1.07	1.348	90.0
2,2	0.277	1.034	1.342	76.85
2,3	0.535	0.927	1.321	63.42
2,4	0.757	0.757	1.288	49.35
2,5	0.927	0.535	1.246	34.27
2,6	1.034	0.277	1.207	17.77
2,7	1.07	0.0	1.19	0.0
3,1	0.0	2.0	1.926	90.0
3,2	0.518	1.932	1.923	75.59
3,3	1.0	1.732	1.915	61.06
3,4	1.414	1.414	1.904	46.27
3,5	1.732	1.0	1.893	31.14
3,6	1.932	0.518	1.885	15.68
3,7	2.0	0.0	1.881	0.0

TABLE 3 Calculated Potential and Stress Functions

Transducer Location	$\Phi @ 50K$	$\Phi @ 80K$	$\Psi @ 50K$	$\Psi @ 80K$
1,1	0.0	0.0	-1.019	-1.631
1,2	.3905	.6248	-.9683	-.1549
1,3	.7830	1.253	-.8036	-.1286
1,4	1.1793	1.887	-.4848	-.7756
1,5	1.554	2.487	.0678	.1405
1,6	1.756	2.810	1.1845	1.8952
1,7	0.0	0.0	3.218	5.1495
1,8	-1.756	-2.810	1.1845	1.8952
1,9	-1.554	-2.487	.0678	.1405
1,10	-1.1793	-1.887	-.4848	-.7756
1,11	-0.7830	-1.253	-.8036	-.1286
1,12	-0.3905	-0.6248	-.9683	-.1549
1,13	0.0	0.0	-1.019	-1.631
2,1	0.0	0.0	-.4351	-.6961
2,2	.1956	.3129	-.3950	-.6321
2,3	.3679	.5887	-.2756	-.4410
2,4	.4854	.7767	-.0742	-.1188
2,5	.4970	.7953	.1956	.3129
2,6	.3357	.5371	.4699	.7519
2,7	0.0	0.0	.3977	.9564
2,8	-.3357	-.5371	.4699	.7519
2,9	-.4970	-.7953	.1956	.3129
2,10	-.4854	-.7767	-.0742	-.1188
2,11	-.3679	-.5887	-.2756	-.4410
2,12	-.1956	-.3129	-.3950	-.6321
2,13	0.0	0.0	-.4351	-.6961
3,1	0.0	0.0	-.1368	-.2190
3,2	.0665	.1063	-.1207	-.1933
3,3	.1188	.1900	-.0742	-.1188
3,4	.1433	.2293	-.0063	-.0103
3,5	.1297	.2076	.0684	.1095
3,6	.0775	.1240	.1272	.2036
3,7	0.0	0.0	.1498	.2396
3,8	-.0775	-.1240	.1272	.2036
3,9	-.1297	-.2076	.0684	.1095
3,10	-.1433	-.2293	-.0063	-.0103
3,11	-.1188	-.1900	-.0742	-.1188
3,12	-.0665	-.1063	-.1207	-.1933
3,13	0.0	0.0	-.1368	-.2190

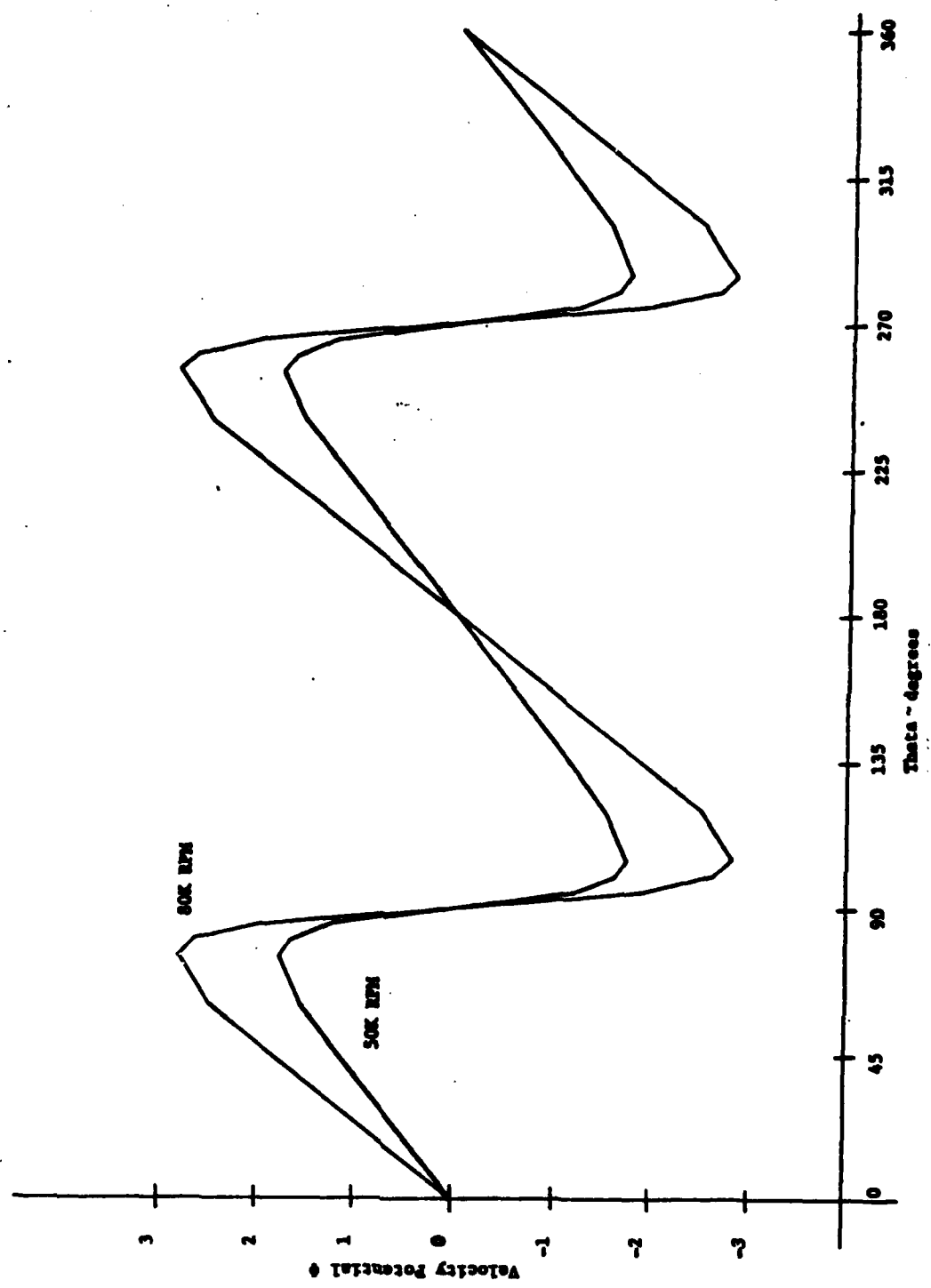


Figure 22 Velocity Potential for Transducer Location 1.

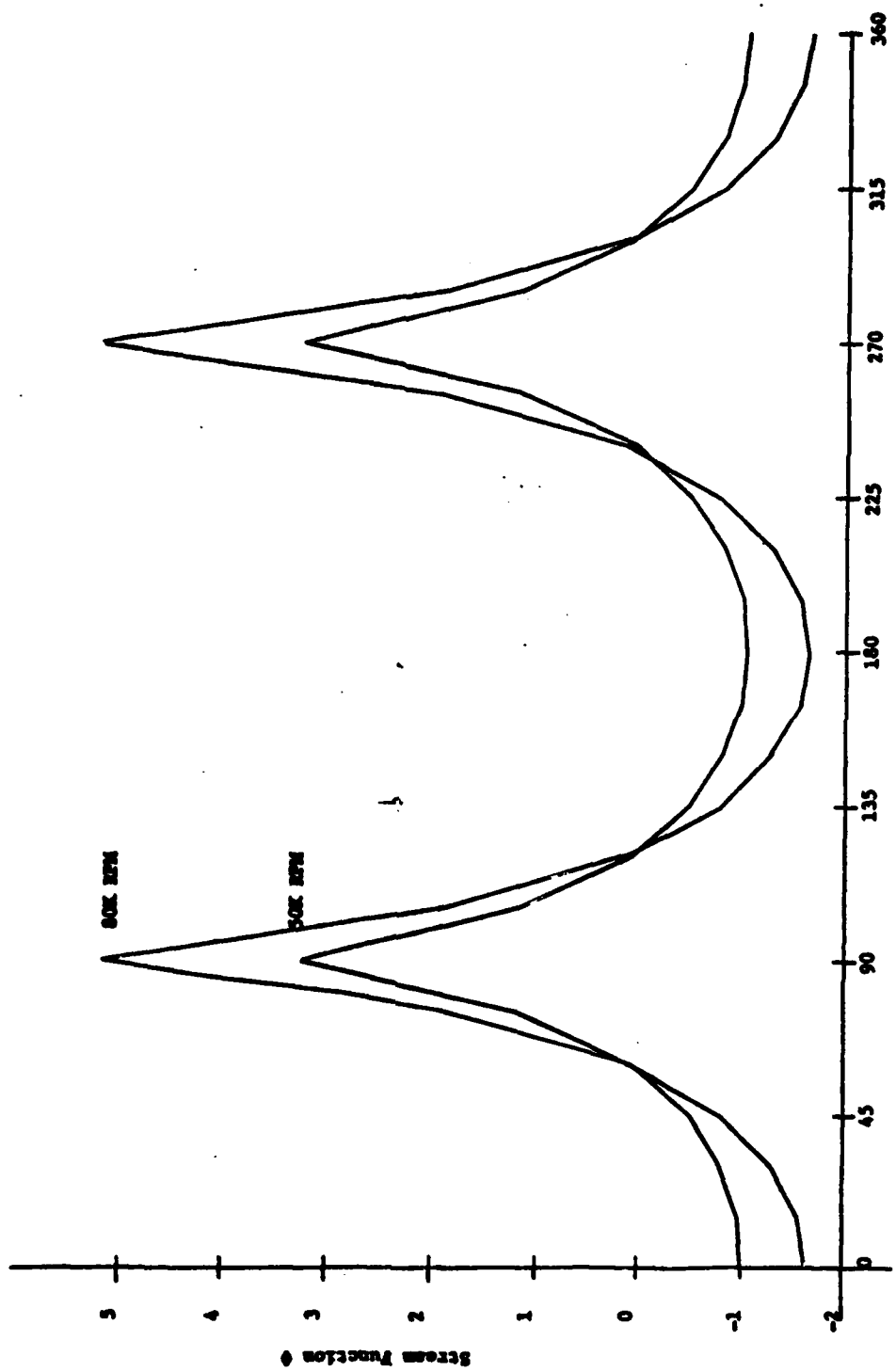


Figure 24 Stream Function for Transducer Location 1

TABLE 4 Calculated Velocities, foot/sec

Transducer Location	V @ 50K	V @ 80K
1,1	28.19	45.12
1,2	29.37	46.96
1,3	33.29	55.28
1,4	41.87	57.00
1,5	50.68	57.11
1,6	113.58	181.74
1,7	365.68	585.17
1,8	113.58	181.74
1,9	50.68	97.11
1,10	41.87	57.0
1,11	33.29	55.28
1,12	29.37	46.96
1,13	28.19	45.12
2,1	8.53	13.65
2,2	8.75	13.99
2,3	9.47	15.15
2,4	10.75	17.21
2,5	12.73	20.37
2,6	14.98	23.96
2,7	16.15	25.85
2,8	14.98	23.96
2,9	12.73	20.37
2,10	10.75	17.21
2,11	9.47	15.15
2,12	8.75	13.99
2,13	8.53	13.65
3,1	1.57	2.52
3,2	1.59	2.55
3,3	1.64	2.63
3,4	1.72	2.75
3,5	1.80	2.88
3,6	1.86	2.97
3,7	1.88	3.01
3,8	1.86	2.97
3,9	1.80	2.88
3,10	1.72	2.75
3,11	1.64	2.63
3,12	1.59	2.55
3,13	1.57	2.52

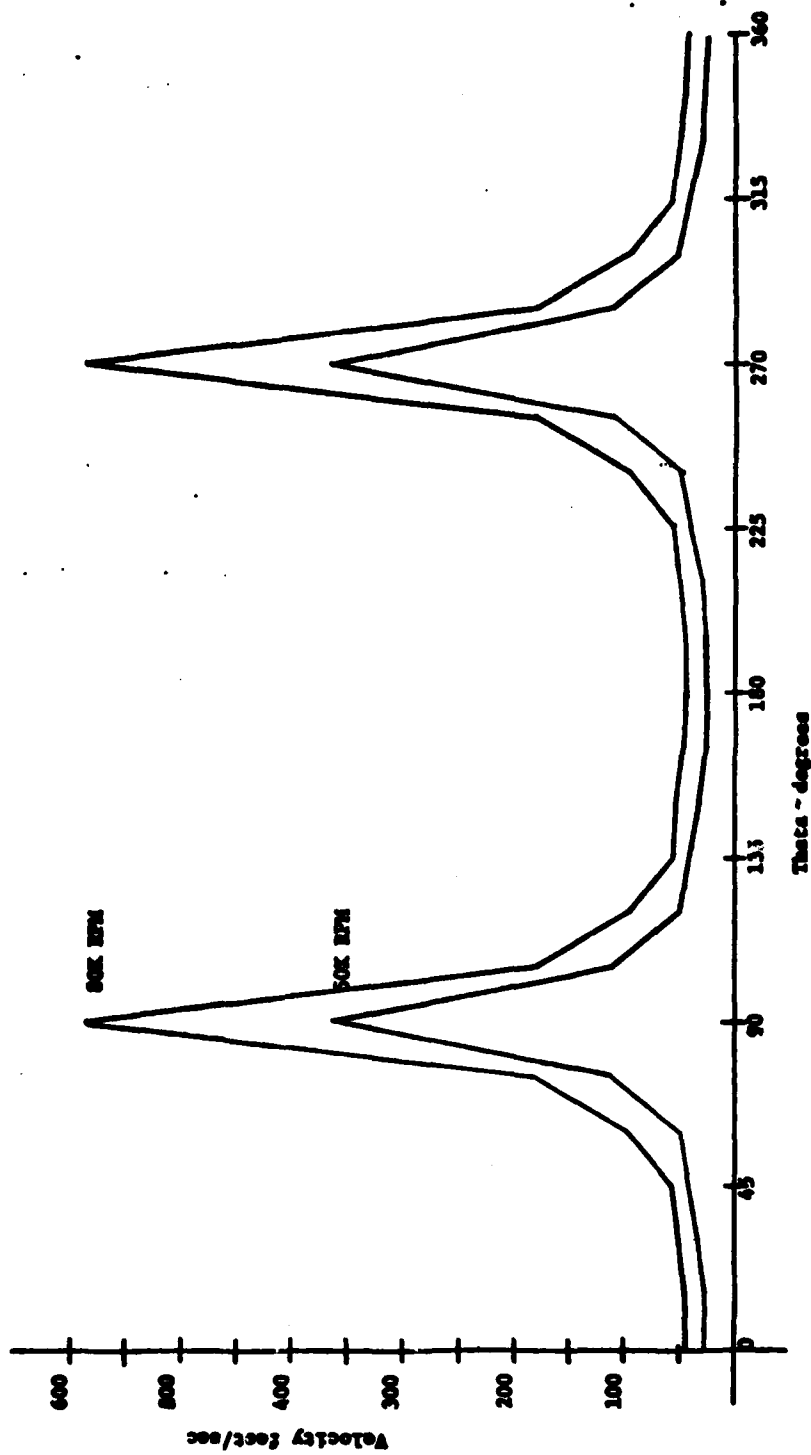


Figure 25 Velocity Calculation at Transducer Location 1

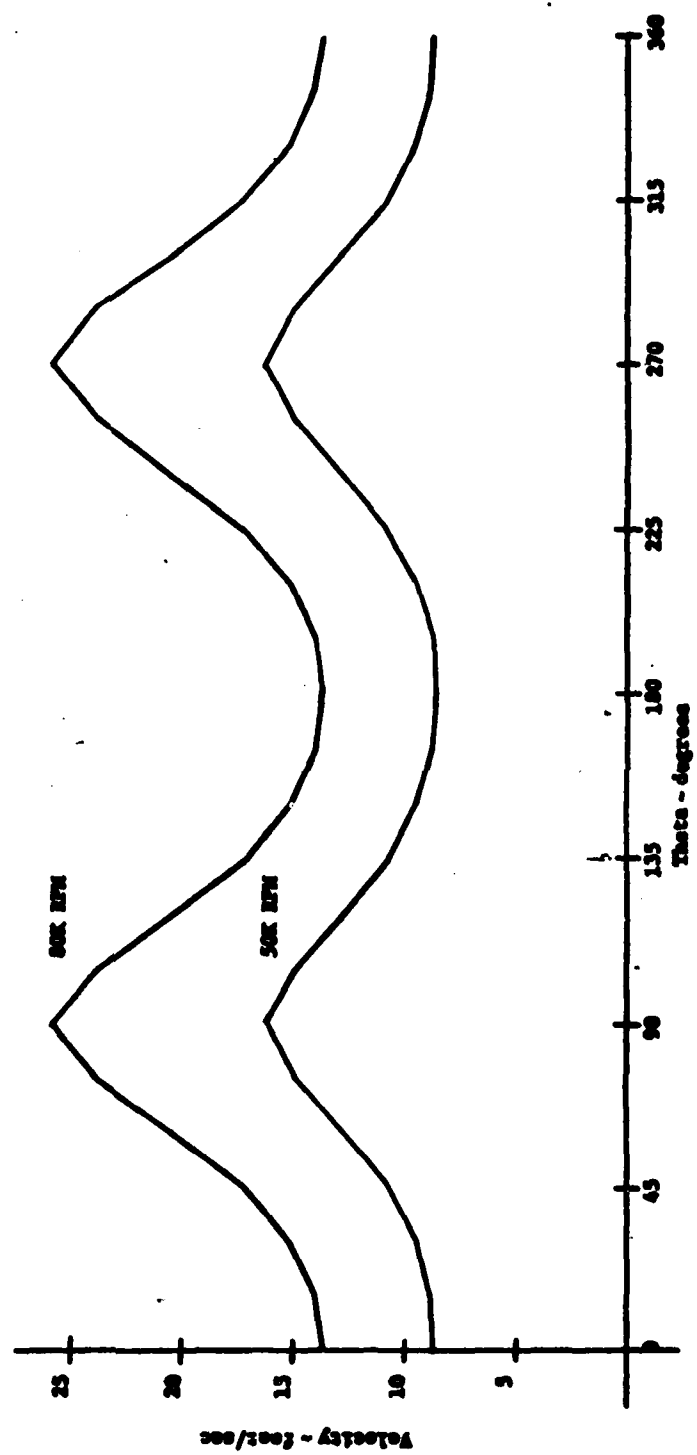


Figure 26 Velocity Calculation at Transducer Location 2

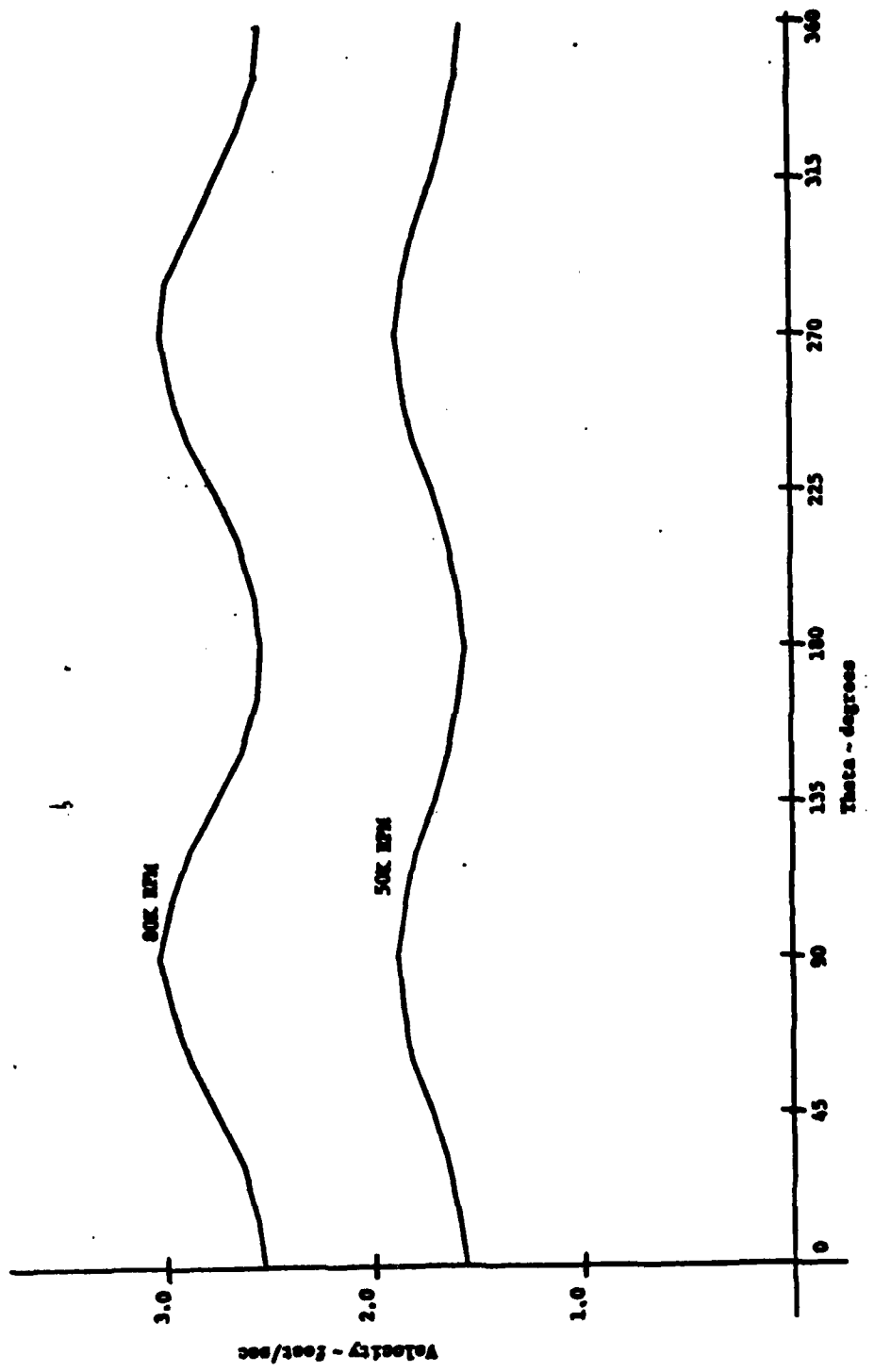


Figure 27 Velocity Calculation at Transducer Location 3

TABLE 5 DYNAMIC PRESSURE DIFFERENCE CALCULATIONS

Transducer Location	$(\Omega - \Omega_1)/\Omega_P$ @ 50k	$(\Omega_1 - \Omega_2)/\Omega_P$ @ 50k
1,1	0	0
1,2	33.3	171.3
1,3	313.5	802.9
1,4	938.4	1213.2
1,5	1773.8	7394.5
1,6	12105.7	30993.6
1,7	132927.2	340368.1
2,1	0	0
2,2	3.8	9.4
2,3	16.9	43.2
2,4	42.8	109.9
2,5	89.3	228.6
2,6	151.6	387.8
2,7	188.1	481.9
3,1	0	0
3,2	.07	0.2
3,3	.23	0.6
3,4	.50	1.2
3,5	.78	1.9
3,6	1.0	2.5
3,7	1.07	2.7

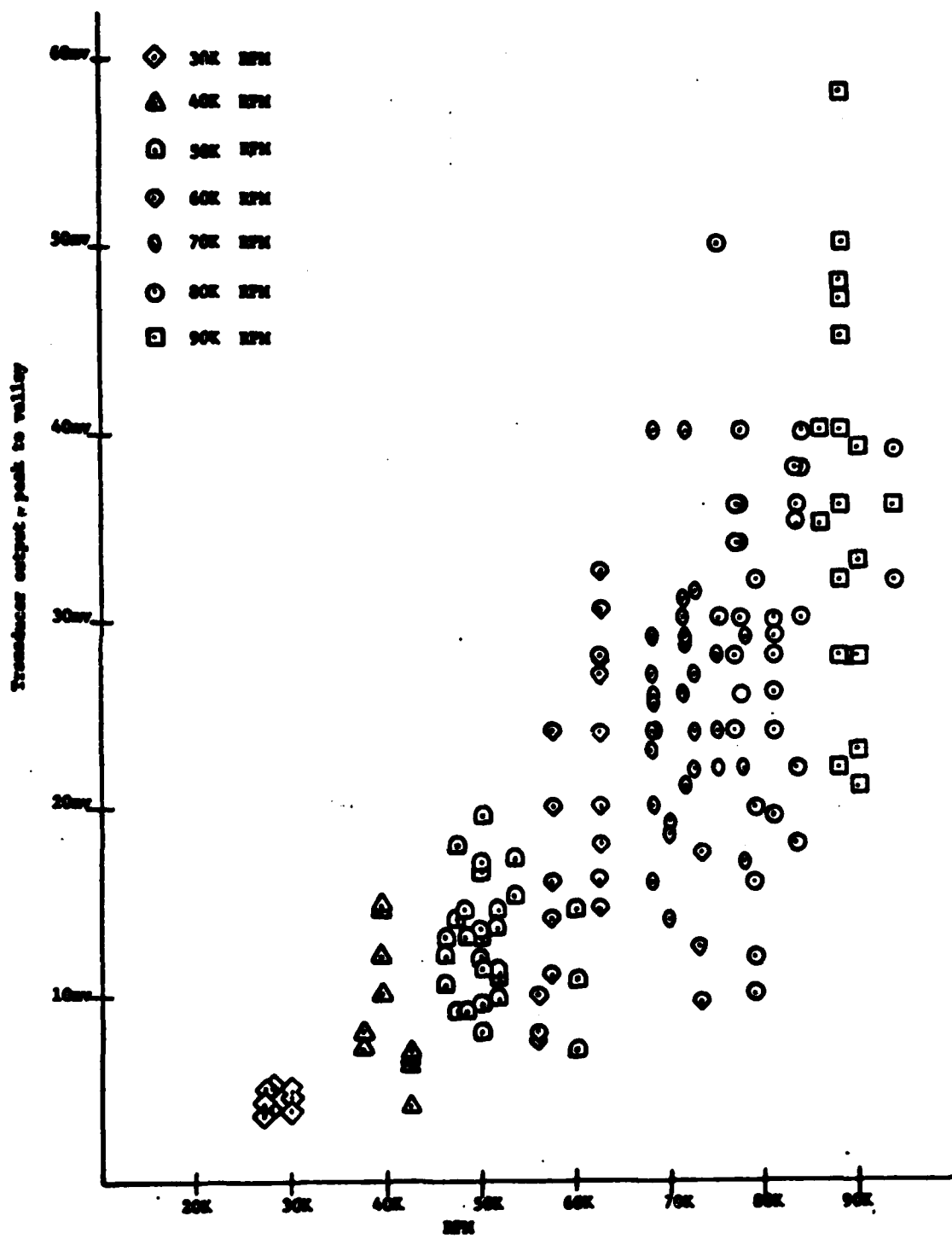


Figure 28 Measured Pressure field-Transducer Location 1

BEST AVAILABLE COPY

TABLE 6 SUMMARY OF MEASURED DATA

ETH	SPRING AVERAGE	APRIL MAXIMUM
30E	.165	.20
40E	.330	.34
50E	.473	.73
60E	.627	1.21
70E	.938	1.48
80E	1.10	1.83
90E	1.323	2.14

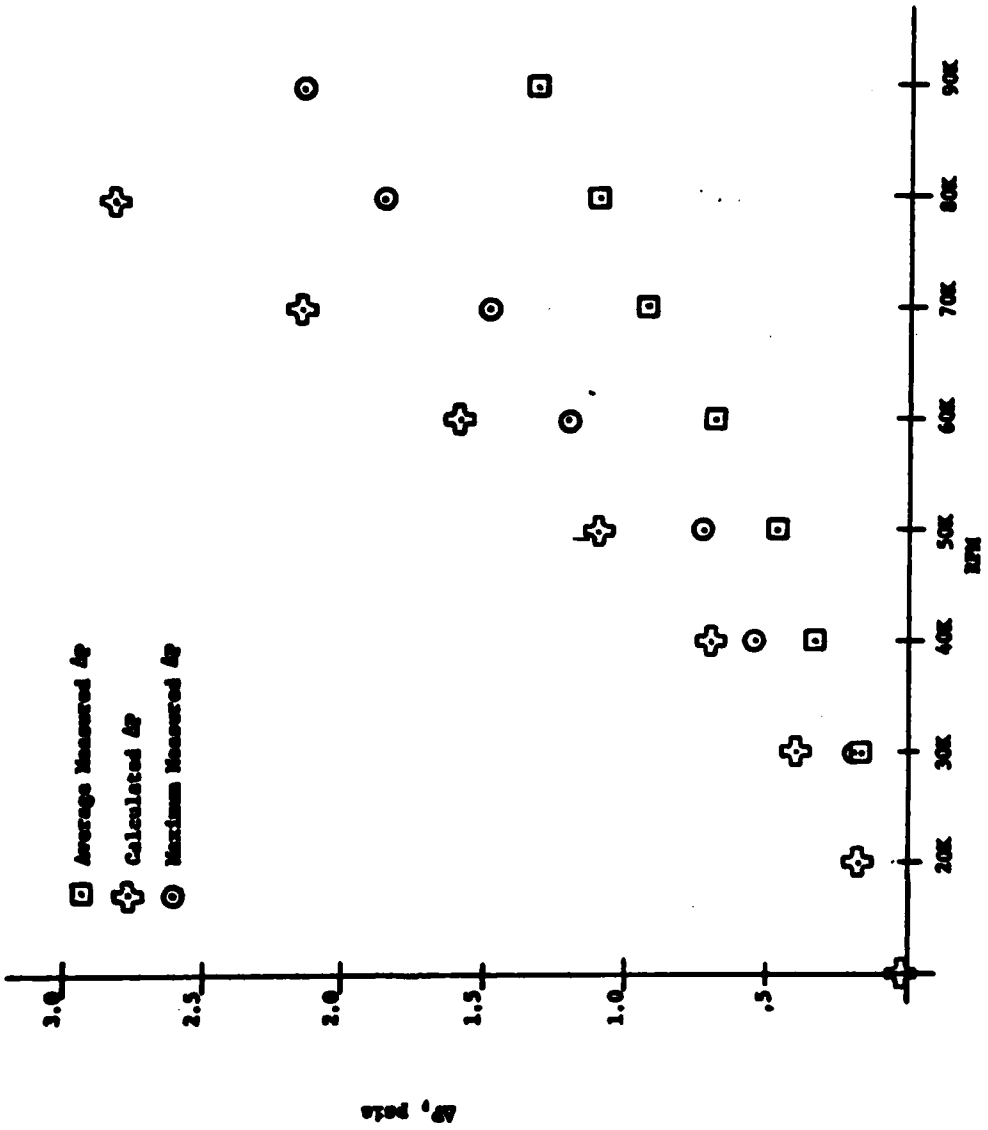


Figure 29 Comparison of Calculated and Measured Pressures

STATUS REPORT DISTRIBUTION LIST

Massachusetts Institute of Technology
Contract N00014-76-C-0253

Transonic Turbines

<u>Recipient</u>	<u>No. of Copies</u>
Chief of Naval Research Department of the Navy Washington, D.C. 20360 Attn: Mr. J.R. Patton, Jr., Code 473	(2)
Commander Naval Air Systems Command Department of the Navy Washington, D.C. 20360 Attn: Mr. R.R. Brown, Code 53673 Mr. I. Silver, Code 330	(1) (1)
Commander Naval Ship Systems Command Department of the Navy Washington, D.C. 20360 Attn: Mr. R.R. Peterson, Code 03413 Mr. C. Miller, Code 6146	(1) (1)
Director U.S. Naval Research Laboratory 4555 Overlook Avenue, S.W. Washington, D.C. 20390 Attn: Technical Information Division	(1)
Commander Naval Ordnance Systems Command Department of the Navy Washington, D.C. 20360 Attn: Mr. B. Drimmer, Code 033	(1)
NASA Lewis Research Center 21000 Brookpark Road Cleveland, Ohio 44135 Attn: Mr. E.M. Syanca	(1)

RecipientNo. of Copies

Defense Documentation Center
Cameron Station
Alexandria, Virginia 22314 (12)

Commander
Naval Air Systems Command
Department of the Navy
Washington, D.C. 20360
Attn: Mr. I. Silver, Code 330 (1)
Mr. R.R. Brown, Code 53673 (1)
Dr. H. Rosenwasser, Code 310C (1)
Technical Library Division, Code 604 (1)

Commander
Naval Ship Systems Command
Department of the Navy
Washington, D.C. 20360
Attn: Mr. R.R. Peterson, Code 03413 (1)
Mr. C. Miller, Code 6146 (1)
Technical Library (1)

The Boeing Company
Headquarters Office
P.O. Box 3707
Seattle, Washington 98124
Attn: Gas Turbine Division (1)

General Electric Company
Aircraft Gas Turbine Division
Cincinnati, Ohio 45215
Attn: Manager of Engineering (1)

Commanding Officer
U.S. Army Research Office
Box CM, Duke Station
Durham, North Carolina 27706
Attn: ORDOR-PC (1)

Director
National Aeronautics & Space Administration
Headquarters
Washington, D.C. 20546
Attn: Division Research Information (1)

<u>Recipient</u>	<u>No. of Copies</u>
Director National Bureau of Standards Gaithersburg, Maryland 20760	(1)
Office of the Assistant Secretary of Defense (R&D) Room 3E1065 - The Pentagon Washington, D.C. 20301 Attn: Technical Library	(1)
Aerojet-General Corporation P.O. Box 296 Azusa, California 91702 Attn: Librarian	(1)
AirResearch Manufacturing Company 9851 Sepulveda Boulevard Los Angeles, California 90045 Attn: Chief Engineer	(1)
General Motors Corporation Allison Division Indianapolis, Indiana 46206 Attn: Director of Engineering	(1)
General Electric Company Engineering Department Turbine Division Schenectady, New York 12305	(1)
General Electric Company Aircraft Turbine Department West Lynn, Massachusetts 01905	(1)
AVCO Corporation Lycoming Spencer Division 652 Oliver Street Williamsport, Pa. 17701	(1)
National Aeronautics & Space Administration Lewis Research Center 21000 Brookpark Road Cleveland, Ohio 44135	(2)
United Aircraft Corporation Pratt & Whitney Aircraft Division East Hartford, Conn. 06118 Attn: Chief Engineer	(1)

<u>Recipient</u>	<u>No. of Copies</u>
Solar Aircraft Company San Diego, California 92101 Attn: Chief Engineer	(1)
United Aircraft Corporation Research Laboratory East Hartford, Conn. 06118 Attn: Director of Research	(1)
Commander U.S. Naval Ordnance Laboratory White Oak Silver Spring, Maryland 20910 Attn: Library	(1)
Commander Naval Weapons Center China Lake, California 93555 Attn: Technical Library	(1)
Commander Wright Air Development Center Wright-Patterson Air Force Base, Ohio 45433 Attn: WCLPN-1, WCACD, WCLPS-1	(3)
Director U.S. Naval Research Laboratory 4555 Overlook Avenue, S.W. Washington, D.C. 20390 Attn: Technical Information Division	(6)
Director Office of Naval Research Branch Office 1030 East Green Street Pasadena, California 91101	(1)
Officer in Charge Naval Ship Engineering Center Philadelphia Division Philadelphia, Pa. 19112 Attn: Code 6700 Technical Library	(1) (1)
Superintendent U.S. Naval Postgraduate School Monterey, California 93940 Attn: Prof. R.P. Shreeve Library, Code 0212	(1) (1)

<u>Recipient</u>	<u>No. of Copies</u>
United Aircraft Corporation Pratt & Whitney Aircraft Division P.O. Box 2691 West Palm Beach, Florida 33402	(1)
Varo, Incorporated 402 East Cutierrez Street Santa Barbara, California 93101 Attn: D.J. Widiner	(1)
Director Ordnance Research Laboratory Pennsylvania State University University Park, Pa. 16802	(1)
Commander Naval Ordnance Systems Command Department of the Navy Washington, D.C. 20360 Attn: Mr. B. Drimmer, Code 033	(1)
Naval Ship Research & Development Center Annapolis Division Annapolis, Maryland 21402 Attn: Library, Code A214	(1)
Naval Undersea Warfare Center 3202 East Foothill Boulevard Pasadena, California 91107 Attn: Technical Library	(1)
U.S. Naval Oceanographic Office Suitland, Maryland 20390 Attn: Library, Code 1640	(1)
Bureau of Naval Personnel Department of the Navy Washington, D.C. 20370 Attn: Technical Library	(1)
Navy Underwater Sound Laboratory Fort Trumbull New London, Conn. 06320 Attn: Technical Library	(1)
U.S. Naval Weapons Laboratory Dahlgren, Virginia 22448 Attn: Technical Library	(1)

<u>Recipient</u>	<u>No. of Copies</u>
Director, Project SQUID Jet Propulsion Center School of Mechanical Engineering Purdue University Lafayette, Indiana 47907 Attn: Dr. Robert Goulard Dr. Bruce Reese	(1)
Army Missile Command Research & Development Director Redstone Arsenal, Alabama 35809 Attn: Propulsion Laboratory	(1)
Director Applied Physics Laboratory 8621 Georgia Avenue Silver Spring, Maryland 20910 Attn: Library	(1)
Commander U.S. Air Force Systems Command Andrews Air Force Base Silver Hill, Maryland 20331	(1)
Commander Air Force Aero Propulsion Laboratory Wright-Patterson Air Force Base Dayton, Ohio 45433	(1)
Commander Air Force Rocket Propulsion Laboratory Edwards Air Force Base, California 93523	(1)
Naval Missile Center Point Mugu, California 93041 Attn: Technical Library, Code 5632.2	(1)
Headquarters Naval Material Command Special Projects Office Washington, D.C. 20360 Attn: Technical Library	(1)
Director of Defense Research and Engineering Technical Library Room 30128 - The Pentagon Washington, D.C. 20301 Attn: Propulsion Technology	(1)
Chief of Research and Development Headquarters, Department of the Army Washington, D.C. 20310 Attn: Dr. S.J. Magram Physical & Engr. Division	(1)

<u>Recipient</u>	<u>No. of Copies</u>
Director, ONR Branch Office 495 Summer Street Boston, MA 02210 Attn: Dr. A.D. Wood	(1)
Defense Documentation Center Building 5, Cameron Station Alexandria, Va. 22314	

Internal Distribution

Professor Jean P. Louis	(5)
Andre Berenfeld	(1)
Nathan Adams	(1)
ONRRR MIT, Room E19-628	(1)
Professor Jack L. Kerrebrock	(1)